FERMILAB-THESIS-2006-96

UNIVERSITÀ DEGLI STUDI DI PADOVA

Sede Amministrativa: Università degli Studi di Padova

Dipartimento di Fisica G. Galilei

DOTTORATO DI RICERCA IN FISICA

CICLO XVIII

New measurements from fully reconstructed hadronic final states of the B_s^0 meson at CDF II experiment

Coordinatore: Prof. Attilio Stella

Relatore: Prof. Giovanni Busetto

Co-Relatore: Dott. Donatella Lucchesi

Dottorando: Dott. Saverio Da Ronco

DATA CONSEGNA TESI
2 Gennaio 2006

Abstract

This Thesis reports the reconstruction and lifetime measurement of B^+, B^0_d and B^0_s mesons, performed using fully reconstructed hadronic decays collected by a dedicated trigger at CDF II experiment. This dedicated trigger selects significantly displaced tracks from primary vertex of $p\bar{p}$ collisions generated at Tevatron collider, obtaining, in this way, huge data samples enriched of long-lived particles, and is therefore suitable for reconstruction of B meson in hadronic decay modes. Due to the trigger track impact parameter selections, the proper decay time distributions of the B mesons no longer follow a simply exponential decay law. This complicates the lifetime measurement and requires a correct understanding and treatment of all the involved effects to keep systematic uncertainties under control. This thesis presents a method to extract the lifetime of B mesons in "*ct*-biased" samples, based on a Monte Carlo approach, to correct for the effects of the trigger and analysis selections. We present the results of this method when applied on fully reconstructed decays of B collected by CDF II in the data taking runs up to August 2004, corresponding to an integrated luminosity of about 360 pb^{-1}. The lifetimes are extracted using the decay modes $B^+ \to \bar{D}^0\pi^+$,$B^0_d \to D^-\pi^+$, $B^0_d \to D^-\pi^+\pi^-\pi^+$, $B^0_s \to D^-_s\pi^+$ and $B^0_s \to D^-_s\pi^+\pi^-\pi^+$ (and *c.c.*) and performing combined mass-lifetime unbinned maximum likelihood fits. We measure

$$\begin{aligned}
\tau(B^0_d) &= 1.510 \pm 0.022\,(stat.) \pm 0.011\,(syst.)\ ps,\\
\tau(B^0_s) &= 1.599 \pm 0.096\,(stat.) \pm 0.036\,(syst.)\ ps,\\
\tau(B^\pm) &= 1.661 \pm 0.028\,(stat.) \pm\ 0.015(syst.)\ ps.
\end{aligned}$$

And for the lifetime ratios:

$$\begin{aligned}
\frac{\tau(B^\pm)}{\tau(B^0_d)} &= 1.100\ \pm\ 0.024\ (stat.)\ \pm\ 0.009\ (syst.)\\
\frac{\tau(B^0_s)}{\tau(B^0_d)} &= 1.059\ \pm\ 0.066\ (stat.)\ \pm\ 0.023\ (syst.)
\end{aligned}$$

All measurements are in agreement with the current PDG world averages [41].

Riassunto

In questa tesi sono trattate la ricostruzione e la misura della vita media dei mesoni B^+, B_d^0 e B_s^0 completamente ricostruiti in decadimenti adronici, effettuate con l'uso di eventi raccolti da un trigger dedicato all'esperimento CDF II. Il trigger utilizzato seleziona eventi con tracce non compatibili col provenire dal vertice primario delle interazioni prodotte dalle collisioni $p\bar{p}$ generate al sincrotrone Tevatron, collezionando campioni di dati con elevata presenza di particelle di vita media attorno al picosecondo. Questo tipo di selezione, basata sul parametro d'impatto delle tracce ricostruite, modifica sensibilmente la distribuzione del tempo proprio di decadimento delle particelle ricostruite. Questa tesi presenta lo studio di un metodo, basato su simulazioni, per correggere e controllare l'effetto prodotto da una selezione di questo tipo sulla misura della vita media dei mesoni B. I Risultati dell'applicazione di questo metodo sono qui riportati assieme ad una trattazione completa degli effetti sistematici di questo tipo di misura. I risultati presentati si basano sui dati raccolti dall'esperimento CDF II tra il Gennaio 2002 e l'Agosto 2004, corrispondenti ad una luminosità integrata di circa 306 pb^{-1}. Ricostruendo quindi i canali di decadimento $B^+ \to \bar{D}^0\pi^+$,$B_d^0 \to D^-\pi^+$, $B_d^0 \to D^-\pi^+\pi^-\pi^+$, $B_s^0 \to D_s^-\pi^+$ e $B_s^0 \to D_s^-\pi^+\pi^-\pi^+$ (e *c.c.*), una determinazione della vita media dei mesoni B è stata effettuata con metodi di unbinned maximum likelihood, misurando:

$$\begin{aligned}
\tau(B_d^0) &= 1.510 \pm 0.022\,(stat.) \pm 0.011\,(syst.)\ ps, \\
\tau(B_s^0) &= 1.599 \pm 0.096\,(stat.) \pm 0.036\,(syst.)\ ps, \\
\tau(B^\pm) &= 1.661 \pm 0.028\,(stat.) \pm 0.015(syst.)\ ps.
\end{aligned}$$

e per il rapporto delle vite medie:

$$\begin{aligned}
\frac{\tau(B^\pm)}{\tau(B_d^0)} &= 1.100 \ \pm\ 0.024\ (stat.)\ \pm\ 0.009\ (syst.) \\
\frac{\tau(B_s^0)}{\tau(B_d^0)} &= 1.059 \ \pm\ 0.066\ (stat.)\ \pm\ 0.023\ (syst.)
\end{aligned}$$

Tutte le misure sono compatibili entro gli errori sperimentali con le medie mondiali riporate nel PDG [41].

. . . Dum loquimur, fugerit invidia aetas:
Carpe diem, quam minimum credula postero.[1]

[1] Quinto Orazio Flacco (Odi), *723 A.U.C.*.

Contents

Chapter 1

Theoretical Overview

In the past decades, big efforts have been done to highlight the gauge sector *of the Standard Model, that proved its reliability even in higher resolution experiments ran at LEP. However, the knowledge of the physics of the* quark sector *is still at a coarser level. This side of the model can be tested studying the B mesons characteristics. B mesons decays studies, allow physicists to access the hidden elements of the* Cabibbo-Kobayashi-Maskawa (CKM) *matrix that characterizes the flavor changing weak interactions. While B factories experiments have performed precise measurements of B_d and B_u meson properties, CDF and DØ experiments at the Tevatron collider, can also produce B_s, B_c mesons and b-baryons, and study those characteristics to further constraint the CKM matrix elements. The study of the B lifetime adds new important elements to Standard Model puzzle, in particular for the B_s^0/B_d^0 and Λ_b/B_d^0 lifetimes ratios. The QCD effects make theory predictions difficult, and a precise determination can give important contributions in understanding these effects in comparison with non perturbative calculation techniques developed so far. In this Chapter we describe the CKM matrix importance within the Standard Model, and overview the framework for B mesons lifetimes and mixing phenomena. Finally, in the last sections, an experimental review will be given .*

1.1 The Standard Model and the CKM

The dynamics of the Standard Model is almost completely determined by the gauge symmetry $SU(3)_{col.} \times SU(2)_L \times SU(2)_Y$ and by the Higgs potential. In fact the spontaneous symmetry breaking of gauge symmetry operated by the Higgs scalar field, breaks the $SU(2)_L \times SU(2)_Y$ symmetry into the residual electromagnetic symmetry $U(1)_{el.}$ generating, in this way, the masses of the weak vector bosons. Therefore, the masses of the quarks and the leptons rely to the coupling constants between the scalar Higgs and the fermions it selves. So, in this picture, only the electromagnetic and strong interactions are the relic symmetries, turning in the fact that the coupling bosons for those interactions are massless.

In the quark sector, the masses are eigenstates for the electromagnetic and strong interactions but not for the weak interactions. Hence, the experimental evidence that the weak interaction can changes the flavor of a given quark via a $W^{\pm}$ exchange, *i.e.* via a charged current. The flavor changing is permitted only between different quark genera-

tions[1] and are characterized by the so called CKM (Cabibbo-Kobayashi-Maskawa) matrix elements.

The experimental evidence supports the existence of three generations of lepton and quark doublets. Within the Standard Model, the fermionic fields interact among themselves through the exchange of the gauge bosons: $W^{\pm}$, Z^0, photons and gluons. These interactions are the result of a local invariance of the Lagrangian under gauge symmetry of the group $SU(3)_{col.} \times SU(2)_L \times SU(2)_Y$. In the case of the $SU(2)_L$ symmetry, the interactions are described by coupling terms of the form:

$$\mathcal{L}_{int} = -\frac{g}{\sqrt{2}}(J^{\mu}W^{+}_{\mu} + J^{\mu\dagger}W^{-}_{\mu}) \tag{1.1}$$

where g is the coupling constant of the $SU(2)_L$ group and can be related to the most common Fermi coupling G_F trough the relation $\frac{G_F}{\sqrt{2}} = \frac{g^2}{8M_W^2}$, while the current J^{μ} is defined by

$$J^{\mu} = \frac{1}{\sqrt{2}}\sum_{i=1}^{3}\bar{u}^i_L\gamma_{\mu}d^i_L, \tag{1.2}$$

with the subscript L standing for the chiral projection of the field $d^i_L = \frac{(1-\gamma_5)}{2}d^i$ and the index i runs over the 3 quark generations. This theoretical framework is not able to produce the fermion masses without the introduction of a scalar doublet, the Higgs boson ϕ.
Its introduction generates new terms in the Lagrangian that allow coupling between mass eigenstates. Hence the mass matrix of the 3 generations quark can have off diagonal terms. A general redefinition of the quark fields can be done in order to diagonalize the mass matrix. Such as redefinition have to be a unitary transformation:

$$u^i_L = U^{ij}_u u'^j_L \qquad d^i_L = U^{ij}_d d'^j_L. \tag{1.3}$$

If we apply the field redefinition in Eq. 1.3 into the interaction Lagrangian in Eq. 1.1, we obtain that Eq. 1.2 moves to

$$J^{\mu} = \frac{1}{\sqrt{2}}\sum_{i,j=1}^{3}\bar{u}'^i_L\gamma_{\mu}V_{ij}d'^i_L, \qquad V = U^{\dagger}_u U_d. \tag{1.4}$$

The matrix V is the Cabibbo-Kobayashi-Maskawa (CKM) matrix that determines the strength of the interactions between quarks of different flavor and $W^{\pm}$ bosons. Because the unitarity constraint, the matrix is present only with the charged vector bosons and no flavor changing neutral currents are allowed at tree level. By construction, a $N \times N$ unitary CKM matrix has N^2 real parameters, however $(2 \cdot N - 1)$ parameters can be absorbed by the freedom in the quark field phase selection [6], via a redefinition of the complex phase of the quark fields. Therefore, the number of independent CKM parameters (that has $N = 3$) is 4, and can chosen to be 3 angles and one phase. The last one, arising from

[1] At tree level.

the fact that the quark generations are three, is the only source of CP violation in the Standard Model[2].
The CKM Matrix is often written in the form

$$V_{CKM} = \begin{pmatrix} V_{ud} & V_{us} & V_{ub} \\ V_{cd} & V_{cs} & V_{cb} \\ V_{td} & V_{ts} & V_{tb} \end{pmatrix}, \tag{1.5}$$

to emphasize the different physic transitions. The elements are indexed with the quarks flavors that participate in the actual vertex. Hence, each interaction vertex that includes a flavor violation is proportional to the correspondent CKM matrix element. The unitarity of the matrix V implies relations between the V_{CKM} elements such as

$$|V_{ud}|^2 + |V_{us}|^2 + |V_{ub}|^2 = 1, \tag{1.6}$$

$$V_{ud}V_{ub}^* + V_{cd}V_{cb}^* + V_{td}V_{tb}^* = 0. \tag{1.7}$$

These relations hold for any choice of rows or columns. Eq. 1.7 defines a triangle in the complex plane (see Fig 1.1), the *unitary triangle* with angles

$$\alpha = \arg\left[-\frac{V_{td}V_{tb}^*}{V_{ud}V_{ub}^*}\right], \qquad \beta = \arg\left[-\frac{V_{cd}V_{cb}^*}{V_{td}V_{tb}^*}\right], \qquad \gamma = \arg\left[-\frac{V_{ud}V_{ub}^*}{V_{cd}V_{cb}^*}\right]. \tag{1.8}$$

An alternative and convenient parametrization of the CKM matrix is the so called *Wolfenstein parametrization* [2]. In this representation the matrix shows a hierarchy that has the diagonal terms close to unity and the other terms smaller and smaller as they move away from the diagonal. More over, the parametrization shows the matrix dependence by the 4 independent parameters, that are chosen to be λ, A, ρ and η, defined as:

$$\lambda \equiv |V_{us}|, \qquad A \equiv \frac{V_{cb}}{\lambda^2}, \qquad \left|\frac{V_{ub}}{V_{cb}}\right|^2 \equiv \lambda^2(\rho^2 + \eta^2). \tag{1.9}$$

Experimentally, we have that $\lambda \simeq 0.22$, $A \simeq 0.8$, and $\sqrt{\rho^2 + \eta^2} \simeq 0.4$; therefore, expanding V_{CKM} in power series of λ we can write

$$V_{CKM} = \begin{pmatrix} 1 - \frac{1}{2}\lambda^2 & \lambda & A\lambda^3(\rho - \imath\eta) \\ -\lambda & 1 - \frac{1}{2}\lambda^2 & A\lambda^2 \\ A\lambda^3(1 - \rho - \imath\eta) & -A\lambda^2 & 1 \end{pmatrix} + O(\lambda^4). \tag{1.10}$$

where $O(\lambda^4)$ stands for terms of order λ^4 or higher. Indeed the unitarity of the CKM matrix implies that there are six orthogonality conditions between any pair of columns or any pair of rows. These triangles have the same area but different sides. For example, the triangle from the first and second column has two long sides of order λ and one very short of order λ^5, while the sides of the triangle depicted from Eq. 1.7 are all of the same order $A\lambda^3$. The uniformity between the sides explains why usually physicist refer to this

[2]In fact, there is another possible source of CP violation arising from the strong sector θ_{QCD}, but no physical evidence has been shown so far.

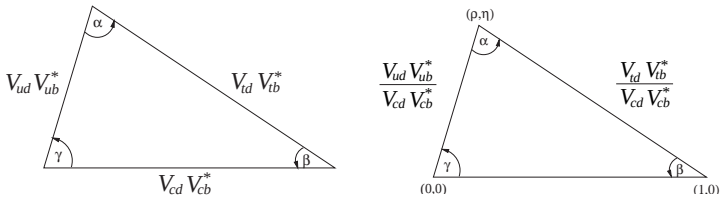

Figure 1.1: *The unitarity triangle. The left one is the expression of the Eq. 1.7. On the right the same triangle with all the sides rescaled by the well know quantity* $V_{cd}V_{cb}^{\star}$.

last triangle. It is worth to notice that usually the Eq. 1.7 is rescaled by a factor $A\lambda^3$ and divided by the experimentally precisely measured term $V_{cd}V_{CB}^*$, defining the quantity

$$\bar{\rho} + \imath\bar{\eta} \equiv -\frac{V_{ud}V_{ub}^*}{V_{cd}V_{cb}^*}. \tag{1.11}$$

The rescaled triangle has a vertex in the origin, one on the real axis and one on $(\bar{\rho}, \bar{\eta})$ in the complex plane. The angles of this triangle can be expressed in terms of these new variable:

$$\alpha = \tan^{-1}\left(\frac{\bar{\eta}}{\bar{\eta}^2 + \bar{\rho}(\bar{\rho}-1)}\right), \quad \beta = \tan^{-1}\left(\frac{\bar{\eta}}{1-\bar{\rho}}\right), \quad \gamma = \tan^{-1}\left(\frac{\bar{\eta}}{\bar{\rho}}\right). \tag{1.12}$$

In this triangle, $\bar{\eta}$, $\bar{\rho}$ and $1-\bar{\rho}$ are comparable making easier an estimation of the their values.

1.1.1 Determination of the CKM Elements

In principle all the particle decay phenomena with flavor violation can provide information to determine the CKM matrix elements. However due to theoretical uncertainties, only few measurements provide results suitable to constrain the Unitary Triangle. The magnitudes of the CKM elements are measured largely, but not exclusively, from semileptonic processes.
A high precision value of $\mid V_{ud} \mid^2$ is obtained comparing the rates for the super-allowed $0^+ \rightarrow 0^+ \quad \beta$ decays, like $^{14}O \rightarrow^{14} N^*$, to the muon decay rate. From these transitions the world average value is $\mid V_{ud} \mid = 0.974 \pm 0.001$ [58].
The semileptonic decays of strange particles like K^0 and K^+ can be used to study $s \leftrightarrow u$ transitions. In particular, $K^0 \rightarrow \pi^- e^+ \nu_e$ gives the best measure of the $\mid V_{us} \mid$. The world average value is found to be $\mid V_{us} \mid = 0.2265 \pm 0.0023$ [58].
The matrix element $\mid V_{cb} \mid$ can be determined studying B meson decays. The b quark decays predominantly into the c quark. The current world average is $\mid V_{cb} \mid = 0.0414 \pm 0.0010(stat.) \pm 0.0018(syst.)$ [58]
Even if B mesons decay predominately in charmed particles, there are some decays involving semileptonic transitions $b \rightarrow u\ell^+\nu_\ell$. Because of the large mass difference between the b and u quarks, the lepton momentum is higher than that in the analogous transition

$b \to c\ell^+\nu_\ell$. Through a measurement of the lepton spectrum is possible to measure the ratio $\frac{|V_{ub}|}{|V_{cb}|} = 0.090 \pm 0.025$ from which $\mid V_{ub} \mid$ can be inferred from the known $\mid V_{cb} \mid$ value [58].
Because the unitarity, only four elements are sufficient to determine the entire matrix. In particular following the Wolfenstein parametrization we have

$$\begin{aligned} \lambda &= |V_{us}|, \\ \left|\frac{V_{ub}}{V_{cb}}\right| &= \lambda\sqrt{\rho^2+\eta^2}, \\ |V_{cb}| &= A\lambda^2, \\ |V_{td}^* V_{tb}|^2 &= A^2\lambda^6[(1-\rho)^2+\eta^2]. \end{aligned}$$

It is thus necessary to obtain information also from the CKM elements involving the top quark. B meson mixing measurements can provide such information because within the Standard Model the mixing frequency can be expressed

$$\Delta m_q = M_{12} = -\frac{G_F^2 m_W^2 \eta_B m_{B_q} B_{Bq} f_{B_q}^2}{12\pi^2} S_0(m_t^2/m_W^2)(V_{tq}^* V_{tb})^2. \tag{1.13}$$

where G_F, m_W, m_t are respectively the Fermi coupling constant and the masses of the $W^\pm$ boson and the *top* quark, S_0 is the Inami-Lim function [7], η_B is a parameter that takes account for QCD corrections and m_{B_q}, f_{B_q}, and B_{B_q} are the mass, the decay constant and the bag parameter of the meson B_q^0 respectively. Measurement of Δm in the B_s^0 and B_d^0 systems can provide information on the CKM elements that are difficult to achieve in other ways.
However, lattice QCD calculations introduce an error of roughly 20% on quantities such as f_{B_q} and B_{B_q}. A measurement of both Δm_s and Δm_d values in the same experiement allows a precise measurement of $\mid V_{td} \mid / \mid V_{ts} \mid$ since most of the hadronic uncertainities cancel out:

$$\frac{\Delta m_s}{\Delta m_d} = \frac{m_{B_S}}{m_{B_d}} \xi^2 \left|\frac{V_{ts}}{V_{td}}\right|^2 \tag{1.14}$$

where $\xi = (f_{B_s}\sqrt{B_{B_s}})/(f_{B_d}\sqrt{B_{B_d}})$ is of the order of one and can be estimated by QCD calculation with an uncertainty at the 2% level [58][59]. Fig. 1.2 shows the current determination of the Unitarity Triangle parameters. Five measurements give the strongest constraints [60]: $\sin(2\beta)$, $\mid V_{ub}/V_{cb} \mid$, ϵ_K, Δm_d, and $\Delta m_d/\Delta m_s$.
The world average value for $\sin(2\beta)$ is 0.69 ± 0.03 [9] and it is dominated by the Belle and BaBar experiments measurements of CP violation in $B^0 \to J/\psi K_S^0$ decays [8]. Additionally B-factories will reduce also the uncertainties on the ratio $\mid V_{ub}/V_{cb} \mid$. Both $\sin(2\beta)$ and $\mid V_{ub}/V_{cb} \mid$ have little theoretical uncertainties. On the contrary even though ϵ_K , that is the amount of CP violation in the kaon system, can be measured quite precisely, translation to a limit on ρ and η is spoiled by theoretical uncertainties at 15% level [8].
Therefore the third most precise constraint to the Unitarity Triangle will come from $\Delta m_d/\Delta m_s$. However this demands a precise measurement of the B_s^0 oscillation frequency, which is a difficult task, because , as it will be shown in the following, the high B_s^0 mass and the predicted high value of the Δm_s.

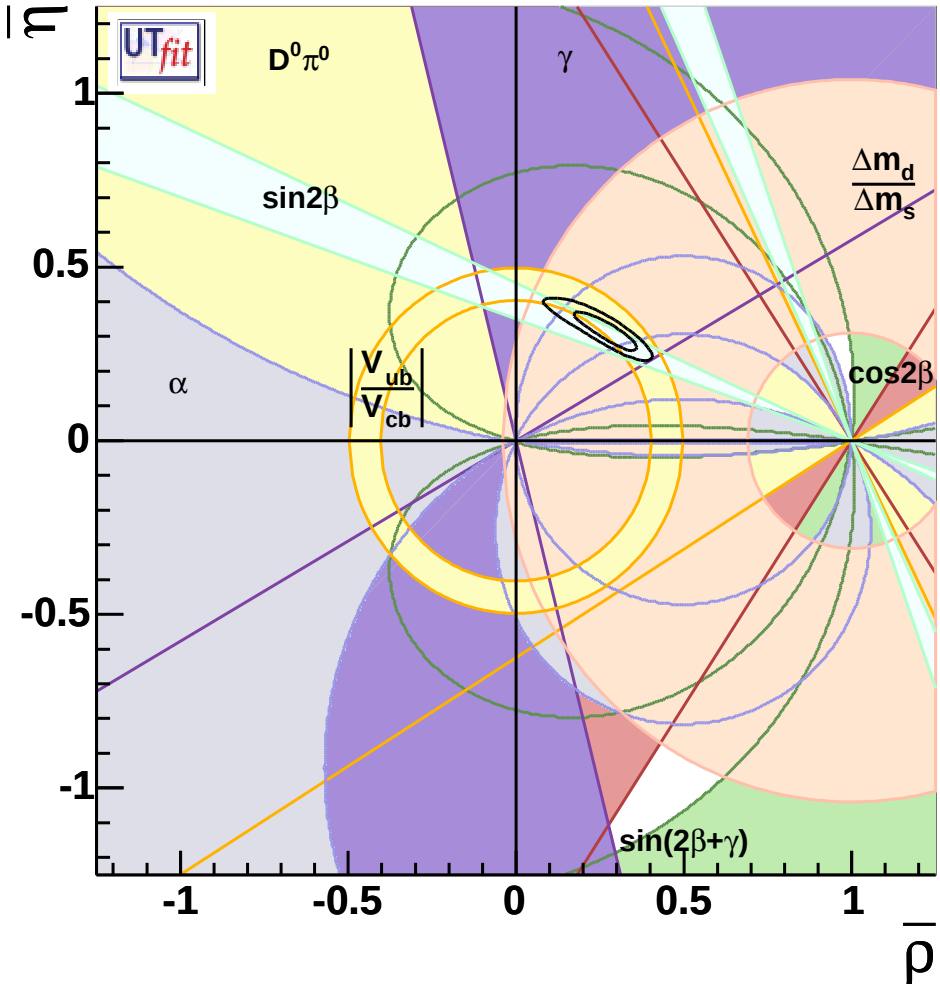

Figure 1.2: *Black circles delimits the regions of 68% and 98% probability for the fit results of unitarity Triangle parameters (ρ, η), overlaid in experimental constraints.*

1.2 The B Mesons Lifetime

Studying the B meson lifetime is of a great importance in the high energy physics. B meson lifetime measurement can provide experimental tests of the QCD phenomena describing the quark confinement in the meson states, and it can also provide independent evaluation of CKM parameters. Finally B meson lifetime analyses are the basic step for any study aimed to measure the mixing phenomena.

In the Standard Model the b quark decays to a c or u quark and a virtual W boson, with couplings given by the corresponding CKM Matrix elements. The W boson can decay into ($\bar{u}$, d) or ($\bar{c}$, s) pairs of quarks or a (l, $\bar{\nu}_\ell$) lepton pair, as shown in Fig. 1.3. The amplitude element for the case of the leptonic W decay can be written as the product of

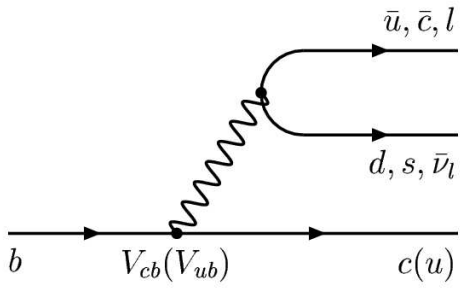

Figure 1.3: *b quark decay in the Standard Model.*

quark and leptonic currents:

$$M_{l\bar{\nu}_\ell} \simeq -\frac{G_F}{\sqrt{2}} V_{bq} \cdot \bar{q}\gamma^\mu(1-\gamma_5)b \cdot \bar{\ell}\gamma_\mu(1-\gamma_5)\nu_\ell, \tag{1.15}$$

in which $G_F = \frac{g^2}{2\sqrt{2}m_W^2}$ is the Fermi coupling constant, and q is either a c or u quark. The validity of the Eq. 1.15 reflects the assumption that the momentum of the b quark satisfy the relation $p < m_b << m_W$. Whenever the assumption holds the true propagator $(-\frac{1}{p^2-m_W^2})$ can be replaced by G_F. Thus the leptonic decay width can be calculated squaring the absolute value of $M_{l\bar{\nu}_\ell}$ and integrating over the phase space, obtaining:

$$\Gamma_{l\bar{\nu}_\ell}(b \to q) = \frac{G_F^2 m_b^5}{192\pi^3} |V_{qb}|^2 F(\epsilon_q), \tag{1.16}$$

where $\epsilon_q = m_q/m_b$ and $F(\epsilon_q)$ is the phase space factor calculated [61] to

$$F(\epsilon_q) = 1 - 8\epsilon_q^2 + \epsilon_q^6 - \epsilon_q^8 - 24\epsilon_q^4 \cdot \ln \epsilon_q. \tag{1.17}$$

The results are not so different for W hadronic decay:

$$\Gamma_{q_1\bar{q}_2}(b \to q) = \frac{G_F^2 m_b^5}{192\pi^3} 3 |V_{q_1q_2}|^2 |V_{qb}|^2 F(\epsilon_q), \tag{1.18}$$

in which $V_{q_1q_2}$ is either V_{ud} or V_{cs}, depending on which way the W decays, and a factor of 3 accounts for the possible color-anticolor combinations can occur. Clearly, the strong interaction corrections are not included. Thus the total width of the b quark, Γ_b, is related to the partial width of a specific decay mode, $\Gamma_{chan.}$, via the branching fraction for this channel, $Br_{chan.}$:

$$\frac{Br_{chan.}}{\Gamma_{chan.}} = \frac{1}{\Gamma_b} = \tau_b. \tag{1.19}$$

Therefore, one could extract the magnitude of certain CKM Matrix elements measuring the branching ratio of a given decay mode, supposed that τ_b is measured, inverting one of the equations 1.16-1.18.

However, b quarks are not available in Nature alone, but they can be studied as constituents of B hadrons. Thus, a big effort is needed to relate B hadrons quantities to the underlying quark theory. QCD effects, in particular, play an important role in this framework, making quantitative predictions harder to do, because we need the help of the non perturbative calculation techniques.

1.2.1 The Spectator Model

A naive, but useful, model, concerning the heavy hadron lifetime prediction, is the Spectator Model. Here the involved heavy quark (c or b) is bound within the hadron H_Q by a lighter *spectator* quark(s). As long as the Spectator Model holds, the decay of H_Q is dominated by the weak decay of the heavy hadron Q, and because that, the lifetime of all hadrons containing Q should be equal to that of the free Q. Experimentally, the situation is a little bit different, and the b hadron lifetimes seem to follow a hierarchy:

$$\tau_{B_c} < \tau_{baryons} < \tau_{B_s} \simeq \tau_{B_d} < \tau_{B_u}. \tag{1.20}$$

The Spectator Model can explain the observed hierarchy with essentially three mechanisms known as Pauli Interference, Weak Annihilation and Weak Exchange.
The Pauli Interference can be thought as follow: consider the diagrams in Figure 1.4(a)-(d); for B_u decay, the external W emission (Fig. 1.4(a)) and the internal color-suppressed W emission (Fig. 1.4(b)), result in the same final state, thus there is an interference between the two diagrams. The interference turns out to be destructive, explaining why the B_u lifetime is longer than that of B_d, for which the interference is absent because the internal and external W emission turns into different final states (see Fig.s 1.4(c)-(d)).
The Weak Annihilation works in the opposite direction with respect to the Pauli Interference, shortening the charged B mesons lifetimes (B_c and B_u). In fact, an additional mechanism for their decay is provided by the diagram 1.4(e); where the two quarks annihilate to form a virtual W boson. In the case of B_u the vertices are weighted by $|V_{ud}|$ CKM elements, so the effect is small. The same diagram cannot contribute to neutral meson because the Standard Model does not allow Flavor Changing Neutral Currents mechanisms, so the B_d and B_s lifetimes are not affected by Weak Annihilation.
Finally the Weak Exchange mechanism, shown in Figure 1.4(f), provides contribution to the B baryons and neutral B lifetimes. This contribution is helicity suppressed in the mesons decay, i.e. the spins of the resulting quarks, $\bar{c}$ and d in the case of the diagram in Fig. 1.4(f), must add up to zero, meaning that they must have the same helicity. This configuration is disfavored in the weak interactions. For the baryons, such suppression is absent because there is no spin requirement on the two quarks, so this mechanism is believed to explain why the B baryon lifetime is slightly shorter than those of the neutral B mesons.

1.2.2 Heavy Quark Expansion Review

In this section we review the Heavy Quark Expansion theory (HQE). HQE is a theoretical framework that allows one to calculate total decay widths of heavy-flavored hadrons including phenomena like those presented in the previous subsection.
The heavy quark Q in a hadron H_Q is surrounded by a cloud of quarks, anti-quarks and gluons, with which Q itself and its decay products interact strongly. Until recently it had been a nearly impossible task to calculate how this "interaction cloud" can affect the Q lifetime. HQE provides a framework in which the calculations can be carried out based on first principles of QCD.
Starting from the optical theorem, the transition rate to the inclusive final state f can be

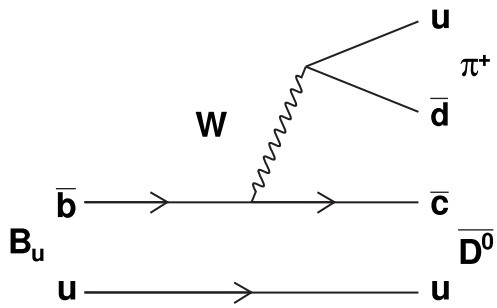

(a)

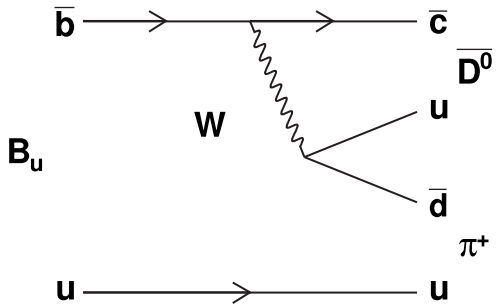

(b)

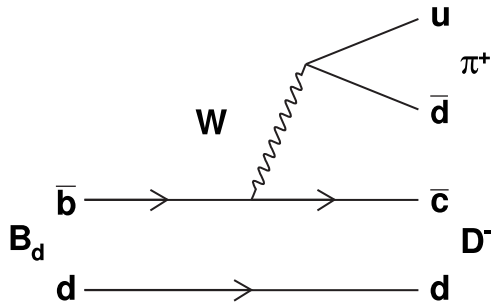

(c)

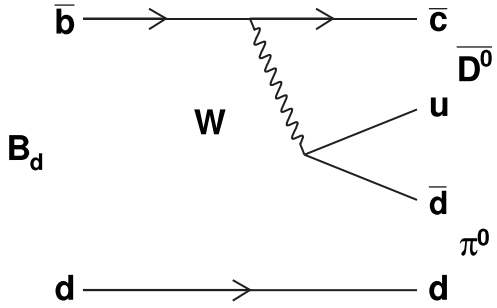

(d)

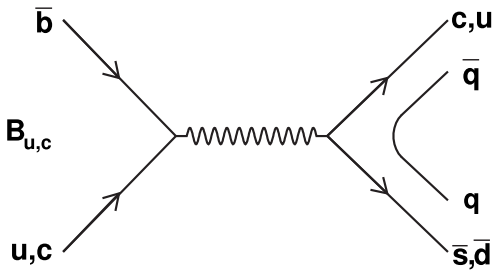

(e)

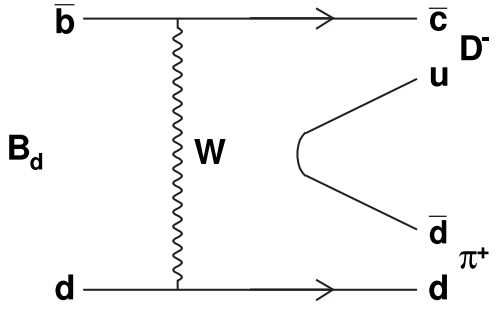

(f)

Figure 1.4: *Lowest order diagrams showing the mechanisms responsible for the B hadrons lifetime hierarchy. (b) and (d) show the different role of the Pauli Interference for B_u and B_d mesons. (e) explains the Weak Annihilation occurring for charged B mesons, while (f) is the lowest order diagram responsible for the Weak Exchange.*

written in terms of the imaginary part of the forward scattering operator:

$$\hat{T}(Q \to f \to Q) = \imath\Im \int T\mathcal{L}_W(x)\mathcal{L}_W^\dagger(0)d^4x, \tag{1.21}$$

where T stands for time-ordered product and $\mathcal{L}_W$ is the effective weak Lagrangian. Under certain conditions, the non-local operator product in Eq. 1.21 can be decomposed into an infinite sum of local operators O_i of increasing dimension i. The rate (width) of $H_Q \to f$ transition is then obtained by calculating the expectation value of $\hat{T}$ for the state H_Q:

$$\langle H_Q \mid \hat{T}(Q \to f \to Q) \mid H_Q\rangle \propto \Gamma(H_Q \to f) = \mid CKM \mid^2 \sum_i \tilde{c}_i^{(f)} \langle H_Q \mid O_i \mid H_Q\rangle, \tag{1.22}$$

where $\mid CKM \mid^2$ is the relevant combination of the CKM Matrix elements. The coefficients $\tilde{c}_i^{(f)}$ in Eq. 1.22 are known as Wilson coefficients, after K. Wilson proposed the Operator Product Expansion in 1969 [5]. They contain higher and higher powers of $\frac{1}{m_Q}$, which multiply correspondingly higher powers of Λ_{QCD} contained in the expectation values of operators O_i. The $\tilde{c}_i^{(f)}$'s can be computed in perturbation theory. Hence, the HQE predicts $\Gamma(H_Q \to f)$ in the form of an expansion in both Λ_{QCD}/m_Q and $\alpha_a(m_Q)$. The precision of the current experiments makes it mandatory to go to the next-to-leading order in QCD, *i.e.* to include corrections of the order of $\alpha_s(m_Q)$ to the $\tilde{c}_i^{(f)}$'s, when HQE predictions are made.

All non perturbative physics is shifted into the expectation values $\langle H_Q \mid O_i \mid H_Q\rangle$ of operators O_i. They can be calculated using lattice QCD or QCD sum rules. Alternatively, they could be related to other observables via HQE, as shown in detail in Reference [3]. Therefore, one may reasonably expect that powers of $\frac{\Gamma_{QCD}}{m_Q}$ provide enough suppression so that the first few terms of the sum in Eq. 1.22 matter.

For the case of semileptonic and hadronic decays Eq. 1.22 can be expanded as

$$\begin{aligned}\Gamma(H_Q \to f) &= \frac{G_F^2 m_Q^5}{192\pi^3} \mid CKM \mid^2 \Big[\tilde{c}_3^{(f)}\langle H_Q \mid \bar{Q}Q \mid H_Q\rangle \\ &+ \tilde{c}_5^{(f)} \frac{\langle H_Q \mid \bar{Q}\imath\sigma GQ \mid H_Q\rangle}{m_Q^2} \\ &+ \sum_i \tilde{c}_{6,i}^{(f)} \frac{\langle H_Q \mid (\bar{Q}\Gamma_i q)(\bar{q}\Gamma_i Q \mid H_Q\rangle}{m_Q^3} + \mathcal{O}(\frac{\Lambda_{QCD}^4}{m_Q^4})\Big],\end{aligned} \tag{1.23}$$

where we have chosen to write Wilson coefficients dependence on m_Q and the familiar $\frac{G_F^2 m_Q^5}{192\pi^3} \mid CKM \mid^2$ factor explicitly. Using the equations of motion one finds that

$$\bar{Q}Q = \bar{Q}\gamma_0 Q - \frac{\bar{Q}[(\imath D)^2 - \frac{\imath}{2}\sigma G]Q}{2m_Q^2} + \ldots \tag{1.24}$$

From Eq. 1.24, taking into account that $\bar{Q}\gamma_0 Q$ is a conserved current, one immediately concludes that

$$\langle H_Q \mid \bar{Q}Q \mid H_Q\rangle = 1 + \mathcal{O}(\frac{\Lambda_{QCD}^2}{m_Q^2}). \tag{1.25}$$

Lifetime ratio	HQE Prediction	Experiment
$\frac{\tau(B^+)}{\tau(B^0)}$	1.06 ± 0.02	1.076 ± 0.008
$\frac{\tau(B_s)}{\tau(B^0)}$	1.00 ± 0.01	0.968 ± 0.029
$\frac{\tau(\Lambda_b)}{\tau(B^0)}$	0.86 ± 0.05	0.792 ± 0.032

Table 1.1: *HQE predictions [13] for the B sector. Experimental results are also reported in the last column [8].*

The First term in Eq. 1.23 implies that the heavier the quark Q, the smaller is the variation in lifetime among different hadrons H_Q. In the limit $m_Q \to \infty$ we get the spectator model prediction. The operator in the second term, referred as the chromomagnetic operator, takes into account the spin interactions. Since the first and second terms do not contain light quark fields, that only enters at the $\frac{\Gamma^3_{QCD}}{m^3_Q}$ level, all B mesons lifetimes have the same magnitude up to $\frac{\Gamma^3_{QCD}}{m^3_Q}$ corrections. The second term generates differences between mesons and baryons lifetimes for a given heavy flavor. The third term is responsible for lifetime difference among mesons and includes effects like Pauli Interference, Weak Annihilation and Weak Interference.

Table 1.1, compiled from References [13] [8], shows the current HQE predictions for the B sector together with the experimental results. In certain cases the experimental precision is more accurate than the theoretical ones.

1.3 The B Meson Mixing

The Standard Model predicts the existence of the mixing phenomenon to take place within the systems of Kaon, charmed and bottom neutral mesons . The Kaon oscillation phenomenon was the first to be observed in the 60's, followed by the more recent mixing in the B^0_d, while B^0_s and D^0 oscillations have not been observed so far.
Within the b sector, the mixing is predicted to take place in two systems of neutral mesons B^0_d and B^0_s. The theoretical model is formally identical for both systems, therefore in what follow we will use B in place of B_s or B_d mesons.
In the Standard Model, the mixing arise through the presence of box diagrams like the ones shown in Fig. 1.5. Flavor violation allows the temporal evolution of the initial state $|B^0\rangle(|\bar{B}^0\rangle)$ into the state $|\bar{B}^0\rangle(|B^0\rangle)$. The time evolution of the initial state is described the Schrödinger equation:

$$\imath\frac{\partial}{\partial t}\begin{pmatrix} a(t) \\ b(t) \end{pmatrix} = \left(M - \imath\frac{\Gamma}{2}\right)\begin{pmatrix} a(t) \\ b(t) \end{pmatrix}, \tag{1.26}$$

where M and Γ are 2×2 independent hermitian matrices, the mass and decay matrix respectively, describing the dispersive and adsorbing components of the mixing. From CPT invariance of the Hamiltonian, we have that the diagonal elements of the two matrices must be equal ($M_{11} = M_{22} \equiv M$ e $\Gamma_{11} = \Gamma_{22} \equiv \Gamma$), while the presence of flavor changing

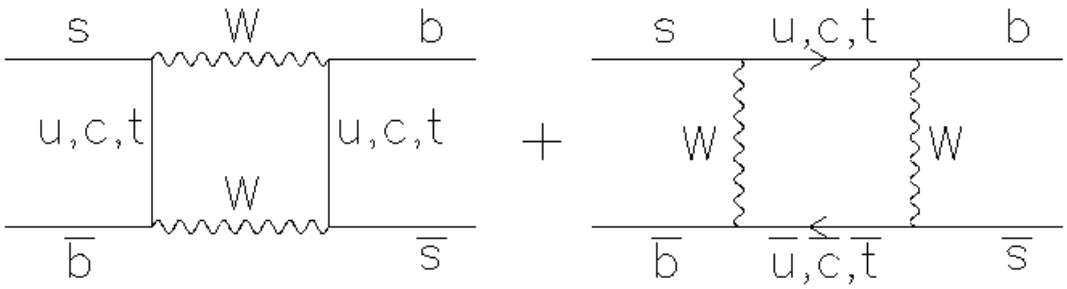

Figure 1.5: *Lower level box Diagrams showing the B_s^0 mixing.*

transitions with $\Delta B = 2$ constraint off diagonal elements to be different from zero. This fact implies that the mass eigenstates are different from the flavor eigenstates $|B^0\rangle$ and $|\bar{B}^0\rangle$. The mass eigenstates are defined as the eigenvectors of the matrix $M - \imath\Gamma/2$ and are expressed in terms of the flavor eigenstates:

$$\begin{aligned} Light\,eigenstate: &\qquad |B_L\rangle = p|B^0\rangle + q|\bar{B}^0\rangle, \\ Heavy\,eigenstate: &\qquad |B_H\rangle = p|B^0\rangle - q|\bar{B}^0\rangle, \end{aligned} \tag{1.27}$$

and the corresponding eigenvalues

$$\lambda_\pm = (M - \frac{\imath}{2}\Gamma) \pm \frac{q}{p}(M_{12} - \frac{\imath}{2}\Gamma_{12}), \tag{1.28}$$

where

$$\left(\frac{q}{p}\right)^2 = \frac{M_{12}^* - \frac{\imath}{2}\Gamma_{12}^*}{M_{12} - \frac{\imath}{2}\Gamma_{12}}. \tag{1.29}$$

Therefore, the temporal evolution of the mass eigenstates is determined by the eigenvalues of the matrix $M - \imath\Gamma/2$

$$|B_{H,L}(t)\rangle = e^{-(\imath M_{H,L} + \Gamma_{H,L}/2)t}|B_{H,L}\rangle. \tag{1.30}$$

so that, given an initial state $|B^0\rangle$ or $|\bar{B}^0\rangle$, using Eqs. 1.30 1.27 we obtain:

$$\begin{aligned} |B^0(t)\rangle &= g_+(t)|B^0\rangle + \frac{q}{p}g_-(t)|\bar{B}^0\rangle, \\ |\bar{B}^0(t)\rangle &= \frac{p}{q}g_-(t)|B^0\rangle + g_+(t)|\bar{B}^0\rangle, \end{aligned} \tag{1.31}$$

$$\tag{1.32}$$

where

$$g_\pm(t) = e^{-\imath Mt}e^{-\Gamma t/2}\left[\cosh\frac{\Delta\Gamma t}{4}\cos\frac{\Delta m t}{2} \pm \imath\sinh\frac{\Delta\Gamma t}{4}\sin\frac{\Delta m t}{2}\right], \tag{1.33}$$

with

$$\Delta m = |M_H - M_L|, \quad \Delta\Gamma = |\Gamma_H - \Gamma_L|. \tag{1.34}$$

Therefore the flavor eigenstate oscillates with a time dependent probability proportional to:

$$|g_{\pm}(t)|^2 = \frac{e^{-\Gamma t/2}}{2}\left[\cosh\frac{\Delta\Gamma t}{2} \pm \cos(\Delta m t)\right]. \tag{1.35}$$

From an experimental point of view, the mixing probabilities are well defined only when we consider decays to final states with well defined flavor, that is, final states f in which a particle can decay but its antiparticle can not. Because of mixing, a B meson can decay into a final state f but also into the final state $\bar{f}$. Therefore the mixing phenomenon can be observed looking at the b flavor when the meson is generated and when it decays. This can be done also without taking into account the time dependence and considering the probability that a B meson mixed at the decay time. Hence, a *time integrated mixing probability* can be defined as:

$$\begin{aligned}\chi_f^{B^0\to\bar{B}^0} &= \frac{\int_0^\infty |\langle\bar{f}|H|B^0(t)\rangle|^2 \mathrm{d}t}{\int_0^\infty |\langle\bar{f}|H|B^0(t)\rangle|^2 \mathrm{d}t + \int_0^\infty |\langle f|H|B^0(t)\rangle|^2 \mathrm{d}t} = \\ &= \frac{|\xi_f|^2(x^2+y^2)}{|\xi_f|^2(x^2+y^2)+2+x^2+y^2},\end{aligned} \tag{1.36}$$

where

$$\xi_f = \frac{q}{p}\frac{\bar{A}_{\bar{f}}}{A_f}, \qquad x = \frac{\Delta m}{\Gamma}, \qquad y = \frac{\Delta\Gamma}{2\Gamma}. \tag{1.37}$$

The mixing probability $\chi_f^{\bar{B}^0\to B^0}$ in the case of $\bar{B}^0$ production can be obtained from Eq. 1.36 substituting ξ_f with $1/\xi_f$. If we neglect the CP violation in the mixing process, we have $|\xi_f|^2 = 1$ and the two probabilities are the same. In this scenario we have

$$\begin{aligned}\Delta m = 2|M_{12}|, \qquad \Delta\Gamma = 2|\Gamma_{12}|, \\ \chi_f = \chi_f^{B^0\to\bar{B}^0} = \chi_f^{\bar{B}^0\to B^0} = \frac{x^2+y^2}{2(x^2+1)}.\end{aligned} \tag{1.38}$$

In the Standard Model the transitions $B^0 \to \bar{B}^0$ and $\bar{B}^0 \to B^0$ are described, at lower order, by the weak interaction mediated by a charged boson W and a quark of type *up* (see Fig. 1.5). As a consequence M_{12} is proportional to the ratio m_q^2/m_W^2, thus the only significant contribution is the one coming from a virtual top exchange, and a similar dependence is expected for the Γ_{12}. More over, the phases of M_{12} and Γ_{12} satisfy the relation

$$\phi_{M_{12}} - \phi_{\Gamma_{12}} = \pi + \mathcal{O}\left(\frac{m_c^2}{m_b^2}\right), \tag{1.39}$$

and this implies that the mass eigenstates must have mass difference and width of opposite sign.

1.3.1 Mixing Phenomenology

Keeping in mind the Eq. 1.35 we can express the 4 mixing probabilities as

$$\begin{aligned}
\mathcal{P}(B \to B) &= \frac{e^{-\Gamma t/2}}{2}\left[\cosh\frac{\Delta\Gamma t}{2} + \cos(\Delta m t)\right] \\
\mathcal{P}(B \to \bar{B}) &= \frac{e^{-\Gamma t/2}}{2}\left[\cosh\frac{\Delta\Gamma t}{2} - \cos(\Delta m t)\right]\left|\frac{p}{q}\right|^2 \\
\mathcal{P}(\bar{B} \to B) &= \frac{e^{-\Gamma t/2}}{2}\left[\cosh\frac{\Delta\Gamma t}{2} - \cos(\Delta m t)\right]\left|\frac{q}{p}\right|^2 \\
\mathcal{P}(\bar{B} \to \bar{B}) &= \frac{e^{-\Gamma t/2}}{2}\left[\cosh\frac{\Delta\Gamma t}{2} + \cos(\Delta m t)\right]
\end{aligned} \tag{1.40}$$

therefore, we can conclude that the mixing probabilities depend on the following observables: the mass difference Δm and the decay width difference $\Delta\Gamma$ between the two mass eigenstates, the parameter $\mid q/p \mid^2$ which signals CP violation in the mixing if $\mid q/p \mid^2 \neq 1$. Depending on the B meson system, the importance of the mixing parameters can change deeply, anyway for both B_d and B_s systems the parameter $\mid q/p \mid^2$ is compatible with the unit, so no CP violation is supposed to take place in the B mixing phenomenon. In what follow we will analyze the contribution of Δm and $\Delta\Gamma$ to the two different B meson mixing systems.

B_d^0 mixing

So far, the experimental effort on B mixing phenomena was able to perform high precision measurement of $B_d^0 - \bar{B}_d^0$ oscillations, with different methods as Fig. 1.6 shows. For this system is possible to perform mixing analysis both with time-dependent and time-integrated techniques. However direct time-dependent studies provide better results, therefore combining all the results, and assuming $\frac{\Delta\Gamma_d}{\Gamma_d}$ to be negligible, we got the following estimations [8]:

$$\Delta m_d = 0.509 \pm 0.004\, ps^{-1}, \tag{1.41}$$

or equivalently:

$$x_d = 0.788 \pm 0.008 \qquad \chi_d = 0.189 \pm 0.004\,. \tag{1.42}$$

Direct time-dependent studies were also used to constraint the $\frac{\Delta\Gamma_d}{\Gamma_d}$ value. Combining the two better results from `BaBar` [10] and `DELPHI` [11] and taking $1/\Gamma_d = \tau(B_d^0) = 1.528 \pm 0.009\, ps$ we got

$$\frac{\Delta\Gamma_d}{\Gamma_d} = -0.009 \pm 0.037. \tag{1.43}$$

B_s^0 mixing

For the B_s^0 meson,the situation is a little bit different. The time-integrated measurements of $\bar{\chi}$ [8], when compared to our knowledge of χ_d and the b-hadron fractions, indicate that B_s^0 mixing is large, with a value of χ_s close to its maximal possible value of 1/2. However, the time dependence mixing has not been observed yet, mainly because the period of these oscillations turns out to be so small that it can't be resolved with the proper time

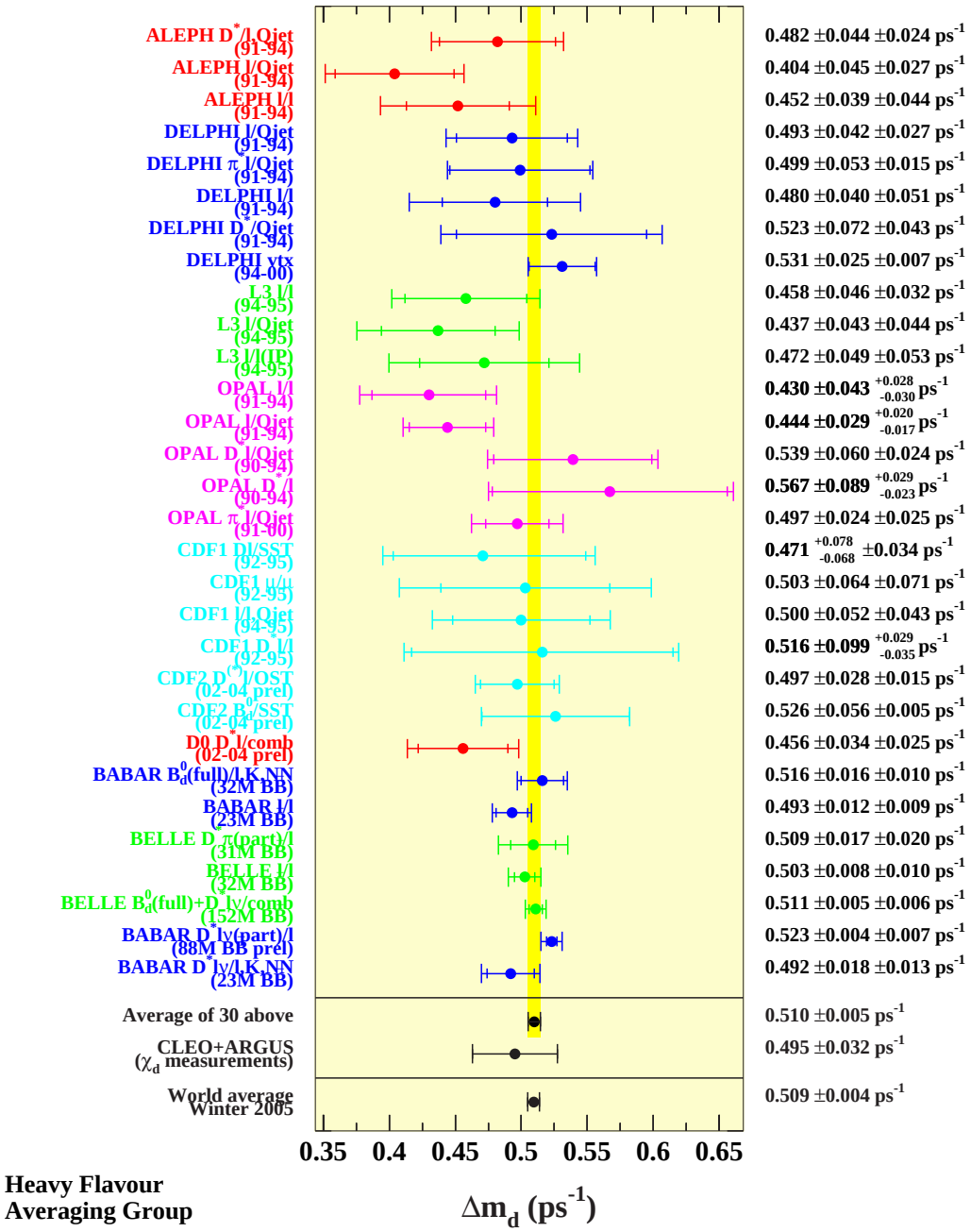

Figure 1.6: $B_d^0 - \bar{B}_d^0$ *mixing experimental results [8].*

resolutions achieved so far.
The statistical significance $\mathcal{S}$ of a B_s^0 oscillation signal can be approximated as [14]

$$\mathcal{S} \sim \sqrt{\frac{N}{2}} f_{sig}(1-2w)e^{-\frac{(\Delta m_s \sigma_t)^2}{2}} \tag{1.44}$$

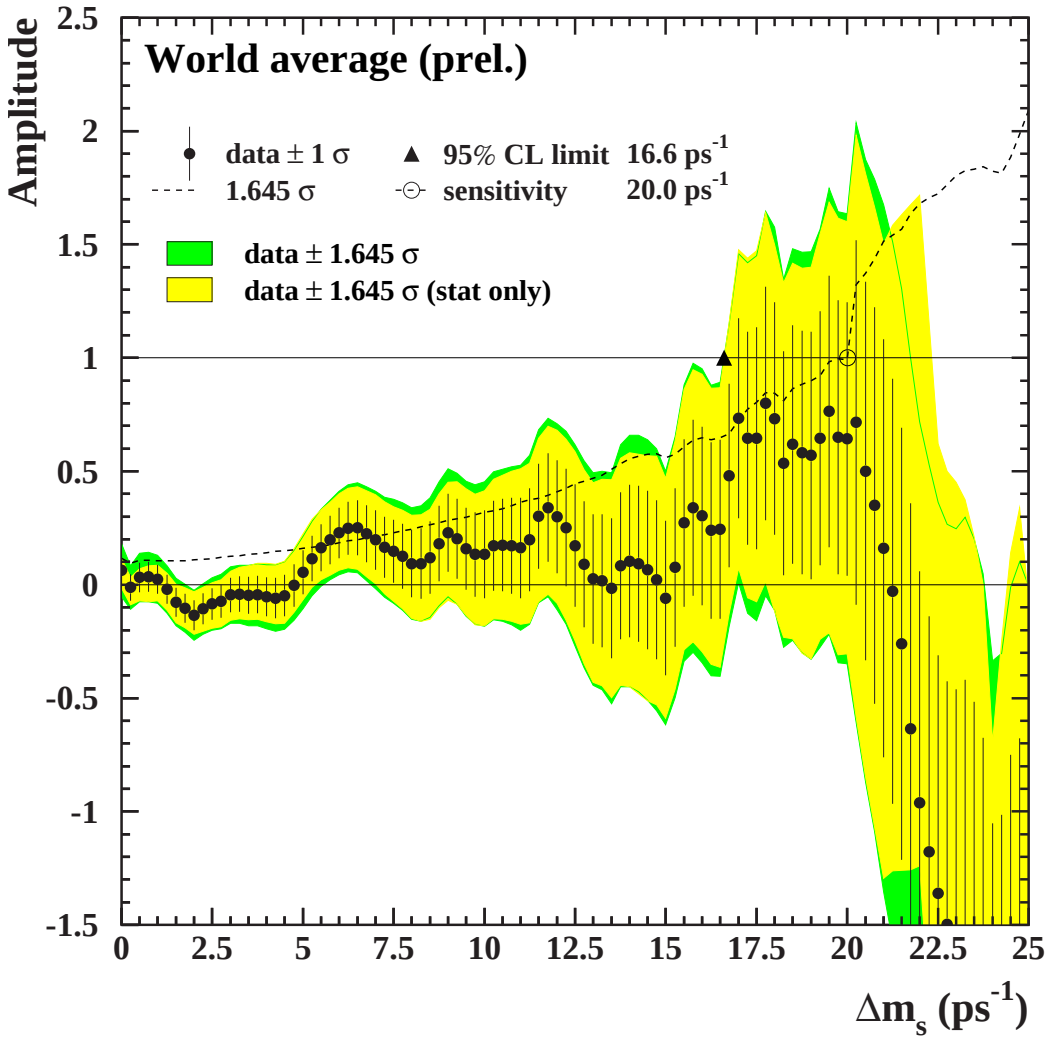

Figure 1.7: $B_s^0 - \bar{B}_s^0$ *mixing experimental results.*

where N is the number of selected and tagged B_s^0 candidates, f_{sig} is the fraction of B_s^0 signal in the selected and tagged sample, w is the total mistag probability[3] and σ_t is the resolution on proper time. As can be seen, the quantity $\mathcal{S}$ decreases very quickly as Δm_s increases: the dependence is controlled by σ_t, which is therefore the most critical parameter for Δm_s analyses.
So far, the widely used method for the Δm_s measurements, is the so called *Amplitude Scan* method. If $N(t)_{mix}$ represents the number of B_s^0 that at the time t have mixed, and $N(t)_{nomix}$ represent the number of B_s^0 that at the time t have not mixed, we got, using

[3]The mistag probability, defined in the next section, can be thought as the probability to mistake the flavor of a quark at generation level.

Eq. 1.40:

$$\frac{N(t)_{nomix} - N(t)_{mix}}{N(t)_{nomix} + N(t)_{mix}} = \mathcal{A}\cos(\Delta m_s \cdot t), \tag{1.45}$$

where the amplitude $\mathcal{A}$ should be equal to 1. The *Amplitude Scan* method consists of measuring the amplitude oscillation $\mathcal{A}$ with different hypotheses of Δm_s value, using maximum likelihood fits on the data sample. The idea is that at the *true value* of Δm_s we must have $\mathcal{A} = 1$, while we get $\mathcal{A} = 0$ at a test value of Δm_s far below the true value. To a good approximation, the statistical uncertainty on $\mathcal{A}$ is Gaussian and equal to $1/\mathcal{S}$ [14].
So far, different experiments tried to measure the Δm_s value [8]. All of them were able to put only a lower limit. The limit estimations can be combined to get the result shown also in Fig. 1.7 :

$$\Delta m_s > 16.6\, ps^{-1} \quad at \quad 95\%\, CL. \tag{1.46}$$

No deviation form $\mathcal{A} = 0$ is seen, that would indicate the observation of a signal [8].
It should be noticed that most Δm_s analyses assume non decay-width difference in the B_s^0 system. Due to the presence of the cosh terms in Eq. 1.40, a non zero value of $\Delta\Gamma_s$ would reduce the oscillation amplitude with a small time-dependent factor that would be very difficult to distinguish from time resolution effects.

1.4 Experimental Review

In previous sections the theoretical motivations for the mixing and lifetime measurements of heavy flavor mesons have been exposed together with the framework used to perform such as calculations. Here, we propose a glance on the experimental framework used to perform such as measurements.
In the past decades the experiments at collider, played a dominant role in the study of the heavy particle features. Among them, B_d^0 and $B^{\pm}$ mesons have been extensively studied at the *B-factories* **Belle**, **BaBar** and **Cleo**, and the best precise measurements have been performed at these experiments. Nevertheless, also the four **LEP** collaborations, **CDF** and **DØ** at Tevatron, and **SLD** at SLC facility gave important contributions and the possibility to study the B_s^0 and the barion Λ_b, that cannot be produced at the *B-factories*.
Both lifetime and time-dependent mixing analyses need proper time information of the reconstructed B meson; this quantity can be extrapolated from spatial informations of the decay vertices. Because the heavy mass, the b quark lifetime is of the order of picosecond, therefore a B meson can fly on average for $500\mu m$ in the laboratory frame before it decays. Hence a secondary vertex displaced from the interaction point is used as a signature of a b decay.
The decay proper time ct, can be measured from the decay length L, defined as the distance between the primary vertex and the reconstructed decay vertex. For relativistic particles we have

$$L = \beta\gamma ct \tag{1.47}$$

where $\beta\gamma = p/m$. Therefore the resolution on the proper time depends on the spatial resolution and on the momentum resolution in the Lorentz boost factor

$$\left(\frac{\sigma_t}{t}\right)^2 = \left(\frac{\sigma_L}{L}\right)^2 + \left(\frac{\sigma_{\beta\gamma}}{\beta\gamma c}\right)^2 . \tag{1.48}$$

High spatial resolutions can be achieved with sophisticated tracking systems like those based on silicon microstrip technology, while momentum resolution depends on the decay mode reconstructed. In the semileptonic modes, for example, that are usually statistically large, the escape of the neutrino turns in a lower energy resolution. On the contrary, reconstructing exclusive modes such as $B_d^0 \to J/\psi K_s^0 \to \ell^-\ell^+\pi^+\pi^-$, or $B_d^0 \to D^{(\star)-}\pi^+$ gives excellent resolution, but you have to pay the price of small statistic due to low branching ratio of these modes ($\sim 10^{-4}$).

1.4.1 Lifetime Measurements

As said before, in most cases lifetime of b hadron is estimated from a flight distance and $\beta\gamma$ factor, which is used in Eq. 1.48 to convert the geometrical distance into the proper decay time. Different methods have been developed to accessing lifetime information, in the next, the commonly used methods will be exposed, and a brief description of the results obtained will be given also.

Inclusive B Hadron Lifetime

These measurements are aimed at extracting the lifetime determination from a mixture of b-hadron decays, without distinguishing the decaying species. Often the knowledge of the mixture composition is limited, which makes these measurements experiment-specific. Also, these measurements have to rely on Monte Carlo to estimate the $\beta\gamma$ factor, because the hadrons are not fully reconstructed. Anyway these usually are the largest statistics b-hadron measurements accessible to a given experiment and are used as an important performance benchmark. To measure the average b-hadron lifetime, the LEP experiments select identified electrons and muons with large momentum, p, and transverse momentum, p_T, with respect to the associated jet axis. This technique typically results in a b-quark purity around 80-90%. Signed impact parameter distributions of the leptons, as defined in Fig. 1.8, are then measured. Fits are made to these distributions using functions of detector resolution convolved with an expected *physics function* of impact parameter as determined from Monte Carlo simulations.

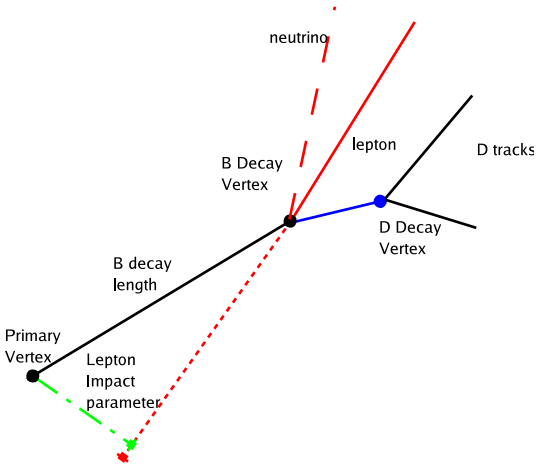

Figure 1.8: *Lepton Impact Parameter from a B meson decaying into D + lepton mode.*

Allowing for the different contributions from charm, cascade ($b \to c \to l$), and primary b quark decays, a value of τ_B is extracted. These measurements give an *average* b-hadron lifetime weighted over the sum of $f(b \to Xhadron) \cdot Br(X \to l) \cdot \epsilon(tag)$. If there is any bias in selection for one type of b hadron over another, the measurement is corrected to the admixture of b hadrons at production. This bias is estimated to be $+0.011 \pm 0.005$ for the lepton measurements. DELPHI's measurement considers hadronic events, not identifying leptons, and is slightly biased against b baryons.

Charge Correlation

A high p_T lepton is usually easy to identify, and it often used as strong signature of a semileptonic b hadron decay. More over, the branching ratio of the b-hadron decays involving leptons (muons and electrons) is around 21%, therefore B meson identification can be performed looking at lepton charge of a partially reconstrected decay mode. Considering the figures 1.4 (a) and (c), it's clear that the neutral B meson will always decay semileptonically into a charged $D^{(\star)}$ meson, whereas a charged B will decay only into a neutral $D^{(\star)}$ meson. That is, $B^0_d \to D^{(\star)+}\ell^-\nu$ decay leads to $D^{(\star)+} - \ell^-$ correlations signaling B^0_d production, while $B^- \to D^0\ell^-\nu$ decay leads to $D^0 - \ell^-$ correlations signaling B^+ production. Unfortunately, the presence of higher spin states of D mesons or non-resonant $D(n\pi)$ states (Usually denoted $D^{\star\star}$) ruins the almost perfect separation obtained in the correlation above. For example, the decay $B^- \to D^{0\star\star}\ell^-\nu$ ($D^{0\star\star} \to D^{\star+}\pi^-$) will also lead to $D^{(\star)+} - \ell^-$ correlations, but now from the charged B. This dilution factor, due to $D^{\star\star}$, has to be estimated with the aid of external measurements and assumptions.
ALEPH, DELPHI,OPAL, and CDF have all measured the exclusive lifetimes of B^0_d and B^+ mesons using partial reconstruction, resulting in samples sizes of several hundred signal events for each experiment. In these analyses, D mesons are first reconstructed using kinematic cuts. For $D^{\star+}$, a small $D^\star - D^0$ mass difference is required, whereas for D^+ and D^0, an *anti-cut* is made on this mass difference. In the next step, high momentum electrons or muons are identified to enhance events containing b quarks through their semileptonic decay. Correct-sign $D^{(\star)} - lepton$ correlations are then formed.
The B decay vertices are reconstructed as the interaction point of the lepton track and the D meson trajectory. So proper decay time distributions can be constructed but Monte Carlo simulations are usually needed to correct the $\beta\gamma$ factor for the lack of neutrino energy. Therefore the charge correlation is used to separate the $B^\pm$ and B^0_d samples where to extract the lifetime via fitting technique on proper time distributions. This method provides high statistic samples and better discrimination of the sample composition. Nevertheless the proper time resolution is usually poor because the neutrino energy lack; all the LEP experiments, for example, reached a B proper time resolution around 300 μm, which is comparable with the b lifetime.

Secondary vertex Charge

Another high inclusive method was used for the first time at the DELPHI experiment [12]. DELPHI used a method that attempts to separate all the charged particles of a jet into two unique vertices: one primary vertex compatible with the beam spot and a secondary

vertex from the B decay. Demanding that the invariant mass of the tracks making up the secondary vertex be grater than 2.2 GeV/c^2 results in an estimated 99% b quark purity. In this method, the event selection is done using kinematical and statistical selections aimed to identify clean secondary vertices. Then all the tracks and energy deposit referring to the secondary vertex are associeted to a B candidate. Therefore the proper time distriubution is done using the decay length between the two vertices and the $\beta\gamma$ factor estimated using Neural Network Techniques [12]. The charge of the secondary vertex is then often found and the efficiency of the charge determination is estimated from the number of doubly-charged vertices and cross-checked in Monte Carlo studies.
Neutral and charged vertices can be therefore separated. While mostly of the charged vertices are from B^+ mesons, the neutral ones arise from B_d^0, B_s^0 and Λ_b. To extract the $\tau(B^+)$ and $\tau(B_d^0)$, charge mis-measurements were unfolded thanks to simulations. For $\tau(B_d^0)$, the influence of B_s^0 and Λ_b decays had to be deduced from measurements and estimates of production rates and branching ratios, contributing to an increased systematic error.
This high inclusive method provides huge samples of data, reducing, in this way, the statistical errors to the percent level. Nevertheless the biggest source of uncertainties comes from the estimation of sample composition that need heavy use of simulations and the externals estimations of branching fractions, giving a systematic error to be comparable with the statistical one.

Ratio of B_d^0 and B^+ Lifetimes

The B_d^0 and B^+ lifetimes, estimated in a inclusive way, are in general anti-correlated in the measurements by each experiment. Because of these correlations, the average lifetime ratio will not necessarily equal the ratio of the averages of the two lifetimes. Each experiment therefore also simultaneously fits the ratio of the two lifetimes with the added advantage that many systematic errors cancel.

Exclusive Decay Reconstruction

In order to avoid the problem of the sample composition determination, lifetime measurement has been performed in exclusive decay mode fully reconstructed. `CDF` has performed the first high statistic measurement of B meson lifetime using fully reconstructed decays. B^+ and B_d^0 have been reconstructed in the decay modes $J/\psi K(J/\psi \to \mu\mu)$, where the K stands for $K^+, K^{(\star)}(892)^+$ or K_S^0,$K^{(\star)}(892)^0$. The decay length are measured reconstructing the secondary vertex in the silicon tracker. Unbinned likelihood fits are performed as shown in Fig. 1.9 where the most recent results are reported.
The lifetimes of similarly reconstructed B^+ and B_d^0 events from the hadronic decay of the Z^0 have also been measured by `ALEPH`. The dominant systematic errors in these analyses are due to alignment and resolution uncertainties plus a trigger bias in the `CDF` analysis, in fact, the use of fully reconstructed decay modes allows to reduce the uncertainty in the particle boost and reach proper time resolution about 50 μm. Anyway this technique suffers from the lack of statistic available and usually systematic uncertainties are well below the statistical ones.

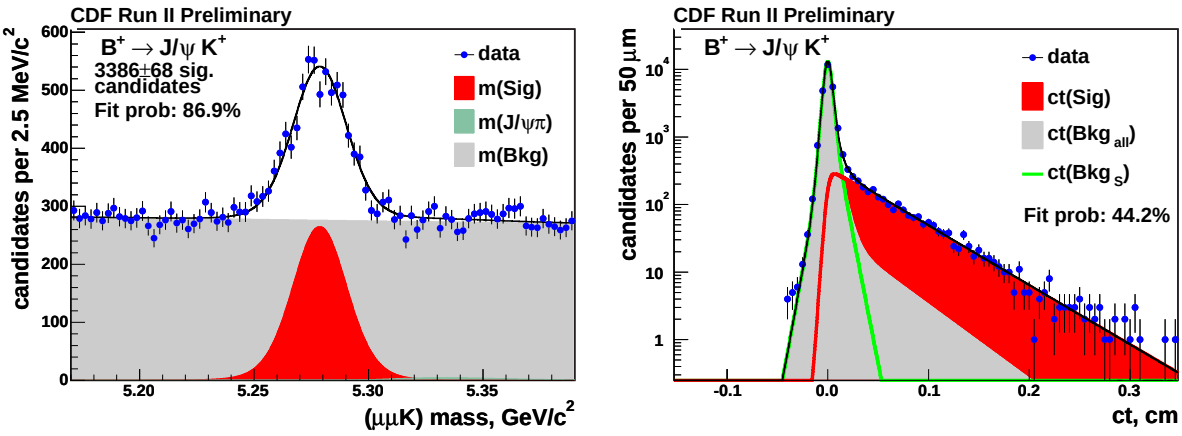

(a) (b)

Figure 1.9: *(a) Invariant mass peak of B^+ candidates reconstructed in the exclusive decay mode $B^+ \to J/\psi K^+$ at CDF II. (b) Fit to the ct distribution.*

B_s^0 Lifetime

Because the high mass value of B_s^0 meson, it cannot be produced at every facility, more over the fragmentation probability that a b quark becomes a B_s^0 meson is ∼10% with respect to the 40% to produce a B_d^0 or a $B^{\pm}$, further reducing the sample size collected. The methods used to measure the B_s^0 lifetime come from the ones used for the B_d^0: referring back to the figure 1.4 (c) , the semileptonic decay of B_s^0 results in the decay $B_s^0 \to D_s^- \ell^+ \nu$. Therefore, similar to the case of B_d^0 and B^+, $D_s^- - \ell^+$ correlations signal the presence of B_s^0.

`ALEPH, DELPHI, OPAL` and `CDF` have all used decay lengths obtained from a combination of high momentum lepton and a reconstructed D_s meson. Usually D_s is reconstructed through the hadronic channels $D_s \to \phi\pi$ and $D_s \to \bar{K}^{\star 0} K^-$, starting by the reconstruction of $\phi \to K^+K^-$ and $\bar{K}^{\star 0} \to K^+\pi^-$. After the D_s reconstruction, a high momentum lepton with the correct charge correlation is required in a similar fashion as in the B_d^0 and B^+ cases. A decay length is formed as the direction-constrained distance between the primary vertex and the point of intersection of the lepton and the reconstructed direction vector of D_s. The B_s^0 boost estimation, the fitting functions used for the signal and the backgrounds, and the level of the background are obtained as in the B_d^0 and B^+ cases.
Fully hadronic reconstructed B_s^0, such as $B_s^0 \to D_s^- \pi^+$ or $B_s^0 \to J/\psi\phi$ were also used, but usually the low statistic collected results in poor resolutions. The dominant systematic in these kind of measurements is due to the understanding of D_s^- from $c\bar{c}$ and the B_s^0 multiplicity. For the semileptonic decay modes, the dominant systematics are due to the modeling of the physics and combinatorial backgrounds, and the knowledge of the boost, decay length, and proper time resolutions.
Thanks to this set of measurements, today the lifetimes of the B_d^0 and B^+ are known at the percent level, while for B_s^0 lifetime the uncertainty is higher (Fig. 1.14).

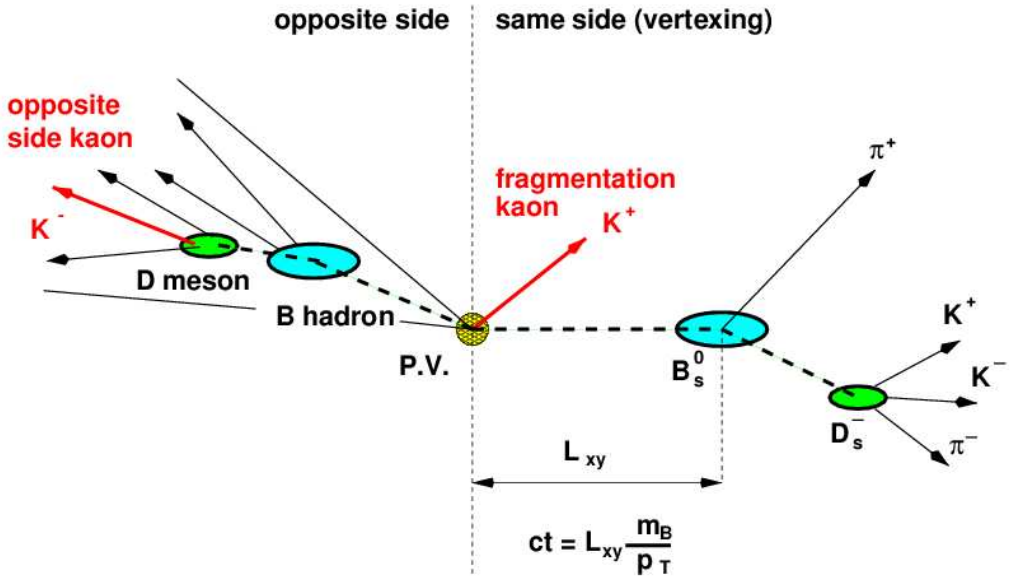

Figure 1.10: *Diagram showing a generic B_s^0 meson decaying hadronically. Different tagging techniques are also represented.*

1.4.2 Techniques for the Δm Measurement

As seen in the previous Sections, direct measurement of the frequency oscillation can be done for all the B systems, and in particular for the B_s^0, this seems to be the only approach available. To perform this kind of measurement we have to know the flavor state of B meson at production and decay level together with an estimation of the proper decay time for that meson. Proper decay time is estimated as for the lifetime analyses using geometrical decay length and boost informations of the desired particle, therefore, as shown in Eq. 1.48, proper time resolution depends on both vertex and momentum resolutions. When the decay proper time is measured, it also necessary to identify the B meson flavor at the creation and decay times. The procedure to do that is usually called *tagging*. The flavor identification in the final state can be obtained studying decay modes with defined flavor. In semileptonic modes this is done looking at the charge of the lepton, while in the hadronic modes this is possible looking at the charge of the charmed meson or at the associated pion(s) and/or kaon(s).
The identification at production level is more challenging, because less dependent on the reconstructed channel, so different techniques have been developed. Essentially two strategies are used for the tagging, the first one, called *same-side tagging*, try to determine the flavor through the charge of the particles produced during the hadronization, the other one, called *opposite-side tagging*, identifies the flavor of the associated B meson in $b - \bar{b}$ events (see Fig. 1.10). The main opposite side tagging methods are the *soft lepton* and *Jet Charge*. The former, use the hypothesis that the opposite b quark decays semileptonically; in this case its flavor can be identified looking for the charge of a displaced lepton. The

Jet Charge method instead, uses geometrical or topological information from the hadronic decays of the opposite b quark to identify its flavor.

As one can guess, the tagging procedure is not perfect, so that one have to take into account the quality of that identification. Usually this is done introducing the quantity called dilution D, defined as

$$D = \frac{N_{tag} - N_{mistag}}{N_{tag} + N_{mistag}} \tag{1.49}$$

where N_{tag} is the number of correctly tagged events and N_{mistag} is the number of wrongly tagged events, also called mistagged events. The dilution is used to define the tagging probability by

$$P_{mistag} = \frac{1-D}{2} \quad P_{tag} = \frac{1+D}{2}. \tag{1.50}$$

In addition, the tagging efficiency is defined as $\epsilon = \frac{N_{tag}}{N_{tot}}$ with N_{tot} the total number of events. The figure of merit in the measurements of Δm is the effective efficiency ϵD^2. Table 1.4.2 shows a comparison between the different tagging procedures at CDF II experiment [73][74][75][76]. So the observed asymmetry is then given by

$$\mathcal{A}(t) = \frac{N^{RS}(t) - N^{WS}(t)}{N^{RS}(t) + N^{WS}(t)} = D \cdot \cos(\Delta m \cdot t) \tag{1.51}$$

where $N^{RS}(t)$ is the number of events in which the decay flavor of the B meson matches the tagged production flavor and $N^{WS}(t)$ is the number of events in which the decay flavor of the B meson is opposite to the tagged production flavor.

Therefore for the B mixing the time independent asymmetry will follow a cosine distribution with an amplitude equal to the dilution. The significance of this signal is given, starting from Eq. 1.44, by

$$\mathcal{S} = \sqrt{\frac{S\epsilon D^2}{2}} \cdot \sqrt{\frac{S}{S+B}} \cdot e^{-\frac{\sigma_{ct}\Delta m}{2}} \tag{1.52}$$

where the first factor defines the effective statistics useful for the measurement, the second factor shows the deterioration of the significance due to background contribution and the third one shows the deterioration due to the measurement uncertainties on the B decay proper time.

Tagging technique	$\epsilon D^2(\%)$	
	CDF II	BaBar
Soft Lepton	1.03 ± 0.05	7.6 ± 0.4
Jet Charge	0.72 ± 0.03	—
Same Side Kaon	2.4 ± 0.6	14.1 ± 0.6

Table 1.2: ϵD^2 *estimations for different tagging procedures at the* CDF II *and* BaBar *experiments.*

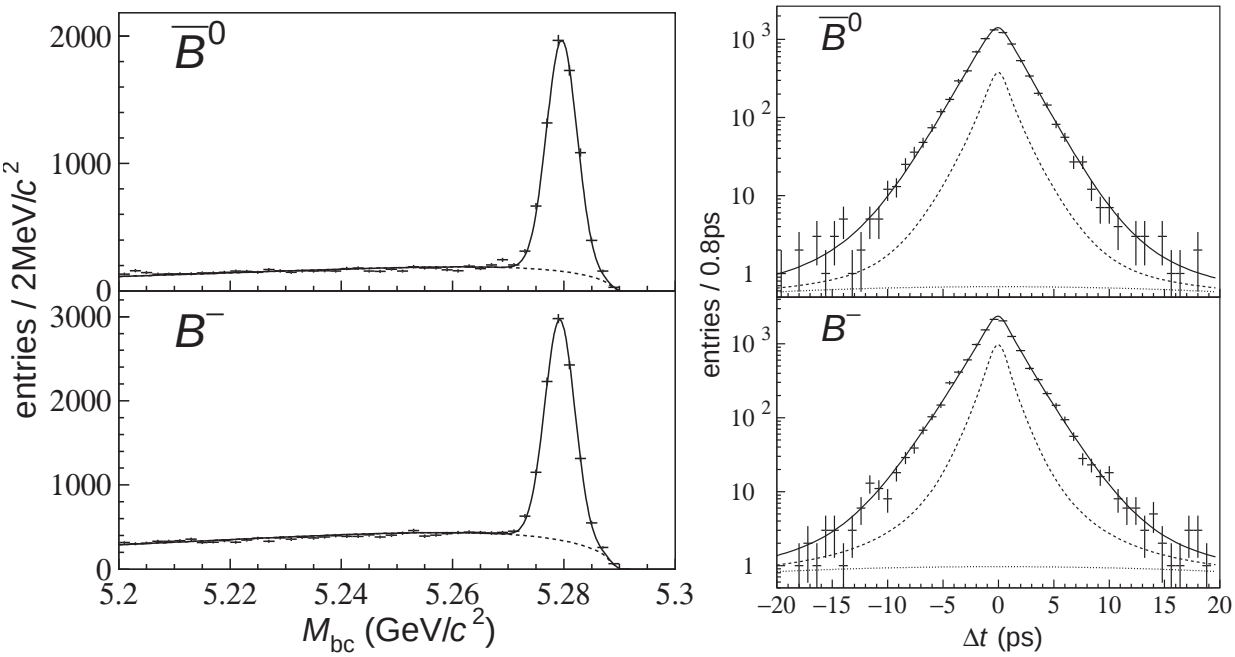

(a) (b)

Figure 1.11: `Belle` *Lifetime measurements for* B_d^0 *and* B^+*. (a) Invariant Mass distributions, (b)* Δt *distributions.*

1.4.3 The *B-factories*

To perform a precision measurements of B particle properties, dedicated experiments have been realized. In this colliding experiment, electron-positron collisions are generated at energies equal to the mass of $b\bar{b}$ states, in order to enhance the $b\bar{b}$ cross section. These experiments are usually called *B-factories*. While `Cleo` uses symmetric beam energies, `BaBar` and `Belle` adopted an asymmetric configuration making possible lifetime measurements. The different accelerator configuration used in the asymmetric B-factories allows to use dedicated techniques to study the B mesons properties, because the asymmetric beams energy, e^+e^- collisions generate boosted $\Upsilon(4S)$ mesons decaying subsequently into a $B_d^0\bar{B}_d^0$ or B^+B^- couples. Since the B mesons are nearly at rest in the $\Upsilon(4s)$ center of mass, B lifetimes can be determined from the separation in z between the two B decay vertices as shown schematically in Fig. 1.12. B mesons are reconstructed using fully reconstructed decay mode. In each event, one B is fully reconstructed while the decay point of the second B is obtained from the vertex posi-

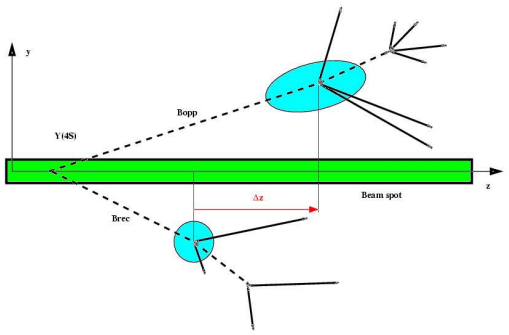

Figure 1.12: Δz *method as used in the B-factories*

tion and momentum vector of the reconstructed D meson and the associated track(s). The charge correlation at the vertices identify the presence of a neutral or charged B. The proper time difference between the reconstructed meson and the associated B decays $\Delta t = t_{rec.} - t_{ass.}$ is calculated as $\Delta t = (z_{rec.} - z_{ass.})/[c(\beta\gamma)_\Upsilon]$, where the $z_{rec.}$ and the $z_{ass.}$ are the z coordinates of the fully reconstructed and associated B decay vertices, respectively. This technique takes advantage of the good momentum resolution of the $\Upsilon(4s)$, but suffers of the poor resolution on z that is, for example, about 180 μm at `BaBar`, when the average $\Delta t \approx \langle\beta\gamma\rangle c\tau_B$ is 260 μm.
The lifetime is then extracted via an unbinned likelihood fit in the Δt distribution as shown in Fig. 1.11. The High statistic available and the purity of the events allow high precision measurements. Unfortunately the collision energy is not able to produce the more interesting B_s^0 mesons, because that, mixing phenomena have been studied for the B_d^0 only. As shown in Table 1.4.2, the cleanest environment of the B-factories allows for better ϵD^2 with respect to the hadron colliders, thus, `Belle` and `BaBar` were able to produce the best measurements of Δm_d (Fig.: 1.6), reconstructing 1 period of the $\mathcal{A}(t)$ asymmetry (Fig.: 1.13).

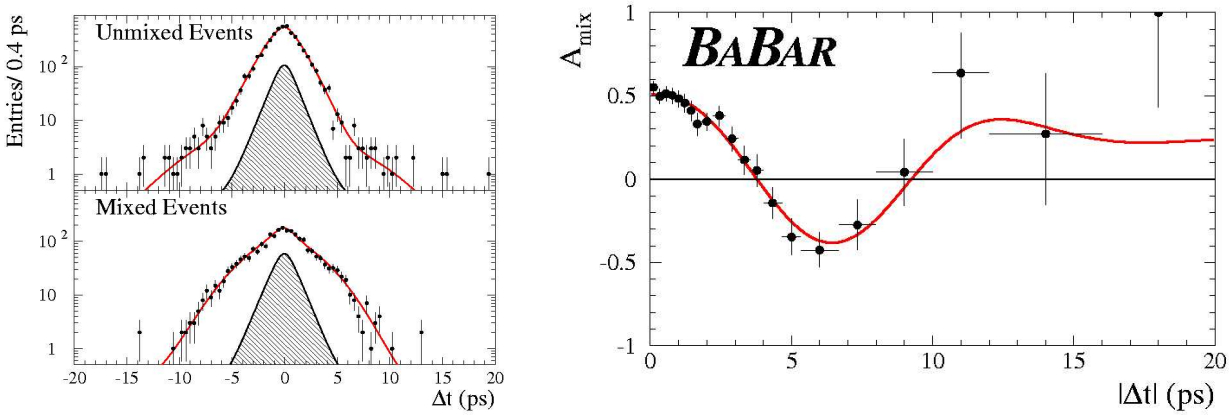

(a) (b)

Figure 1.13: B_d^0 *mixing results from* `BaBar` *experiment. Distributions of* Δt *for (a) unmixed and (b) mixed events. (c) The time-dependent asymmetry* $\mathcal{A}(|\Delta t|)$ *defined in Eq. 1.51.*

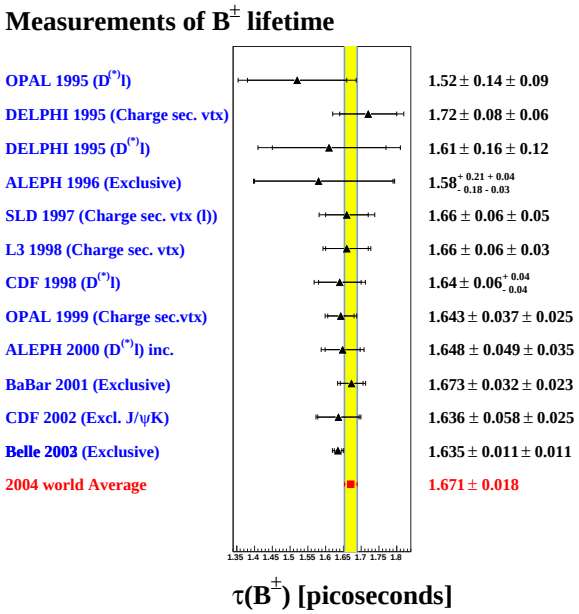

(a)

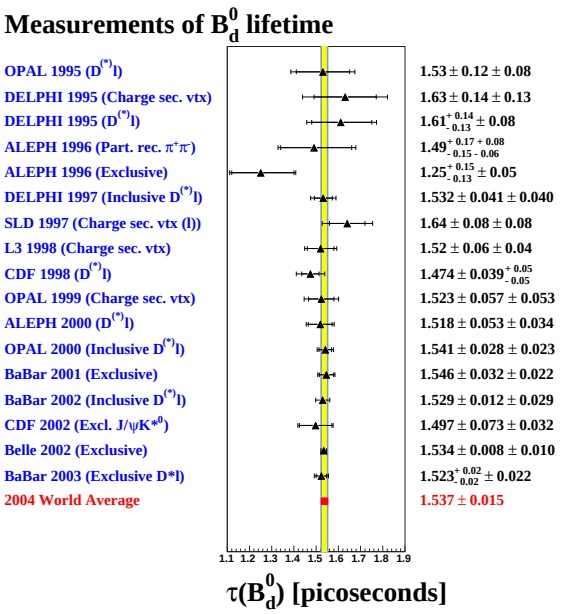

(b)

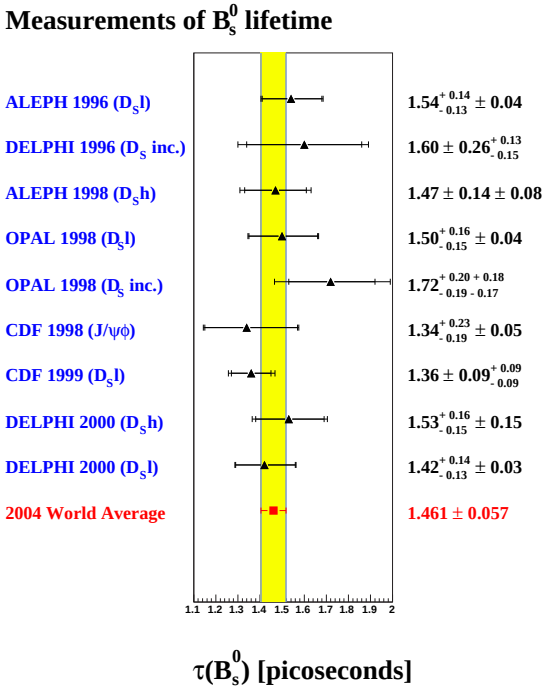

(c)

Figure 1.14: *Lifetime World Averages: (a) the $B^{\pm}$ meson; (b) the B^0_dmeson; (c) the B^0_s meson. The most significant results are also reported. In parenthesis the method used to extract the lifetime.*

Chapter 2

The Experimental Apparatus

The Tevatron accelerator provides, after the latest upgrades, proton-antiproton head-on collisions to energies at center of mass close to 2 TeV. Thus we have a very interesting environment where heavy quarks are generated with a high cross-section and generally with high boost. The improved CDF II detector was installed at Tevatron ring to collect the informations about the interactions taking place during these collisions. This Chapter describes the experimental apparatus, the Tevatron accelerator and CDF II detector, that produced and collected the data used in this analysis, respectively.

2.1 The Tevatron Collider

The Fermilab Laboratories are a large complex near Chicago where a sophisticated apparatus was build to accelerate and collide protons and antiprotons to exploit high-energy physics analyses. Figure 2.1 shows a simplified sketch of the accelerator system, which involves several stages such as: preparing protons and antiprotons, accelerating them, injecting them into the Tevatron, controlling the beam sizes and finally colliding them in selected regions where the detectors are installed.

2.1.1 The Proton Source

The process leading to $p\bar{p}$ collisions begins in a Cockroft-Walton chamber, where electrical discharges into hydrogen gas, enveloped within an electrostatic field, produce negative ions, immediately accelerated by a positive voltage applied to a so-called extractor plate. The resulting negative ions are then driven via a magnetic field to the linear accelerator, the Linac. The magnetic transportation system provides also a filtering tool to remove non -H^- ions.
The Linac [16] picks up the H^- ions at energy of 750 KeV, and accelerates them to inject into the Booster. The Linac is divided in two subsystems: a first drift-tube that accelerates the H^- to 116 MeV, and a second side-couple cavity accelerated structure used to bring up the negative ions to the energy of 400 MeV. The Booster [15], is a fast cycling synchrotron about 150 meters in diameter. It provides both acceleration of the ions to the energy to 8 GeV and the conversion of the incoming negative H^- to the final protons (H^+). The Booster loading scheme overlays the injected beam with

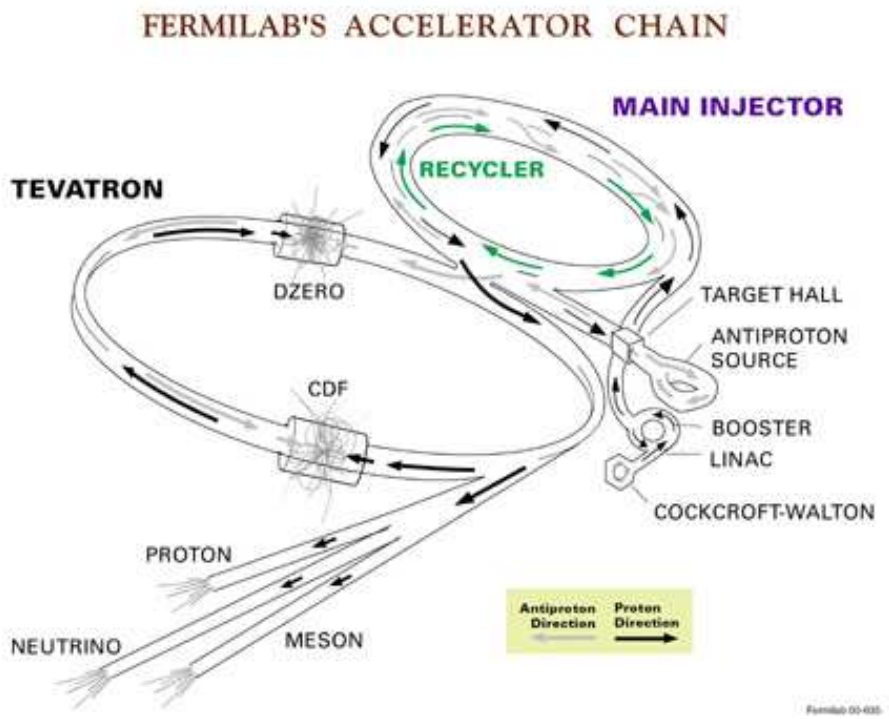

Figure 2.1: *The FERMILAB's accelerator chain.*

the one already circulating in the machine. In fact, the H^- source and the overlaid beam injection were developed to increase beam intensity from the Booster: the idea exploits the fact that it's a proton beam that circulates in the Booster, while the Linac provides the incoming beam of negative H^- ions. Superimposing H^+ and H^- beams does not violate the *Liouville 's Theorem*[1]. When this is accomplished, the mixed beams are forced through a carbon foil, which strips off the electrons turning the negative hydrogens into protons. In order to minimize the beam blow-up due to stripping, the beams are forced to pass through the carbon foil only during loading.
When the bare protons are collected in the Booster, they are accelerated to the energy of 8 GeV by the conventional method of varying the phase of RF fields in the accelerator cavities [15] and subsequently injected into the Main Injector. The final "batch" will contain a maximum of 5×10^{12} protons divided among 84 bunches spaced by 18.9 ns of 6×10^{10} protons each.

2.1.2 The Main Injector

During the Run I era the protons and antiprotons were injected into the Tevatron by the Main Ring, an old[2] 400 GeV proton synchrotron. Originally the Main Ring was not designed as a Tevatron injector, it was later adapted to this purpose, and that clearly limited its performances. To improve the antiproton production capability, the Run II

[1]The density in phase space remains constant along a dynamic trajectory (in presence of conservative forces), in particular two dynamic trajectories cannot merge.

[2]The Main Ring was build in the early 1970's.

Upgrade includes the new Main Injector (MI). This is a new rapid cycling accelerator designed to accomplish several topics such as: accepting 8 GeV protons or antiprotons coming from the Booster or antiproton Accumulator or the Recycler, accelerating the protons to 120 GeV and delivering them to the antiproton target or a fixed target area or the neutrino Beamline (NuMI), accelerating protons and antiprotons up to 150 GeV for the Tevatron Injection, and finally accepting the 150 GeV antiprotons from the Tevatron ring and decelerating them to 8 GeV to transfer to the Recycler.
The MI is seven times the circumference of the Booster. So it can hold 6 Booster batches with 84 bunches in each of them. In the Collider Mode, the six batches are accelerated to the *flat top* (150 GeV), the maximum energy to which a machine can keep the particles for an extended time. At *flat top* the bunches are coalesced into a single bunch of 27×10^{10} protons that is subsequently injected into the Tevatron. The described procedure constitutes a single MI cycle. To fill the Tevatron with protons thirty-six of such cycles are needed. Due to the fact that the coalescing efficiency is not 100%, the MI is able to prepare at maximum 4 Tevatron bunches per cycle, requiring at minimum 9 cycles to fill the Tevatron ring.
When the Tevatron is filled with the final protons, the MI goes back to its other duties that can summarized as: antiproton production, discussed in Section 2.1.3, and intense beam delivered for the fixed target and/or neutrino experiments.

2.1.3 The Antiproton Source

As the proton production is a relatively easy task, the same is not true for the antiprotons. In fact, the antimatter is harder to come by on Earth, and we have to produce it from scratch [17]. Anyway colliding protons and antiprotons, compared to protons and protons, has greater advantages even if it's more difficult to produce them in a sufficient quantity. In fact the antiprotons can be accelerated in the same ring used for protons, because the opposite charge, reducing the cost of the magnet for a second ring. More over, the production rate for a number of interesting processes is higher in $p\bar{p}$ collisions at $\sqrt{s}$ up to 3 TeV compared with pp collisions at the same energy.
The Figure 2.2 shows the general layout of the antiproton source at the Tevatron. As mentioned in the Section 2.1.2 the antiproton production is one of the Main Injector's greater tasks. During antiproton stacking mode, the MI accelerates batch of 5×10^{12} protons at 120 GeV, and sends them to hit a nickel target. The collision with the target produces a shower of secondary particles that are focused by the use of a lithium lens [17]. Then a pulsed dipole magnet deflects the 8 GeV antiprotons toward the Debuncher [17], while the undesired particles with wrong charge-to-mass ratio are filtered out of the beam and collected by a graphite-core beam-dump. The antiprotons produced in this way present an high spread in kinetic energy that have to be reduced before to use them in a narrow beam. This process of reducing the kinetic energy spread is referred as *cooling* the beam. New batches of antiprotons are initially cooled in the Debuncher synchrotron, collected and further cooled using stochastic cooling in the 8 GeV Accumulator synchrotron [15]. The stochastic cooling [17] is a feedback based method. Some pick up sensors sample the average motion of particles in the beam and corrects the trajectory for the average using kicker electrodes, which are a pair of electrodes placed around the ring. Integrated over

a long period of time, this manifests itself as a damping force applied to the individual particles which evens out their kinetic energies.

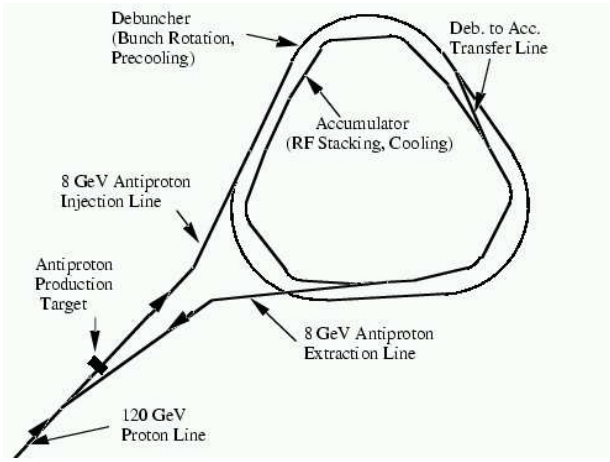

Figure 2.2: *Layout of the antiproton source.*

The cooled antiprotons are then transferred to the Accumulator. Here the antiprotons produced are collected and prepared to be injected in MI. In fact the Accumulator provides also a further cooling step in order to even out the different antiproton batches and to prepare the bunches that will be injected in the MI and subsequently, after they will be accelerated to 150 GeV, into the Tevatron ring. The overall production can take from 10 to 20 hours to built up a stack of antiprotons which is then used in the Tevatron collisions. Antiproton availability is the most limiting factor attaining high luminosities, assuming there are no technical problems with the accelerator, motivating why a lot of effort was spent to upgrade the antiproton production at Tevatron for the Run II. In this context is important to mention the Recycler ring [18]. The Recycler is designed to collect the antiprotons left at the end of a Collider *store*[3] and re-use them in a later store. The Recycler will also take up the role of the Accumulator as the final storage for 8 GeV antiprotons allowing the existing Antiproton Source to perform more efficiently and produce antiprotons with higher rate.
The Recycler was included in the Fermilab Program in 1997 as an addition to the Main Injector project. Most of the lattice elements (dipoles and quadrupoles) are made out of permanent magnets and the ring shares the tunnel with the MI keeping low constructional and operational costs, but substantial benefits are expected, as promised by the first colliding stores in 2005, that thanks to Recycler were able to reach high instantaneous luminosities.

2.1.4 The Tevatron Ring

The Tevatron is the last stage of the Fermilab accelerator chain. The Tevatron is a 2 km synchrotron able to accelerate the incoming 150 GeV beams from MI to 980 GeV,

[3] a roughly 20 hour period of time when the colliding beams are retained within the Tevatron

providing a center of mass energy of 1.96 TeV. The accelerator employs superconducting magnets throughout, requiring cryogenic cooling and consequently a large scale production and distribution of liquid helium. During The Run II the Tevatron operated at the 36×36 mode, which refers to the number of bunches in each beam.
The antiprotons are injected after the protons are already been loaded. Just before the antiproton injection a set of electrostatic separators are used to create a pair of non-intersecting helical closed orbits. When the Tevatron loading is complete, the beams are accelerated to the maximum energy and the collisions begin. In the 36×36 mode, there are 72 regions along the ring where the bunch crossing occurs. While 70 of these are parasitic, in the vicinity of CDF and $D\emptyset$ detectors, additional focusing and beam steering is performed, to maximize the chance the proton strikes an antiproton. The Focusing, driven by quadrupole magnets, reduces the beam spot size increasing the *luminosity*. The instantaneous luminosity, a quantity proportional to number of collision per unit time, is given approximatively by:

$$\mathcal{L} = \frac{N_B N_{\bar{p}} N_p f}{2\pi(\sigma_{\bar{p}}^2 + \sigma_{\bar{p}}^2)} \tag{2.1}$$

Where N_B is the number of bunches, $N_{(\bar{p}),p}$ is the number of the (anti)protons per bunch, f is the revolution frequency, and $\sigma^2_{(\bar{p})p}$ is the effective width of the (anti)proton beam. Clearly, smaller is $\sigma^2_{(\bar{p})p}$ results in a larger rate of collisions. During collisions the instantaneous luminosity decreases in time as particles are lost or beam begin to heat up. In the meanwhile new antiprotons are stored in the Accumulator. When the luminosity becomes too much low (approximately after 15-20 hours) it becomes beneficial dumping the current store and start a new cycle. Table 2.1 summarizes the accelerator parameters for the Run II and Run I configurations.

Parameter	Run I	Run II
number of bunches (N_B)	6	36
bunch length [m]	0.6	0.18
bunch spacing [ns]	3500	396
protons/bunch (N_p)	2.3×10^{11}	3.3×10^{11}
antiprotons/bunch ($N_{\bar{p}}$)	5.5×10^{10}	3.6×10^{10}
interactions/crossing	1	1.5
typical luminosity $[cm^{-2}s^{-1}]$	0.16×10^{32}	0.9×10^{32}

Table 2.1: *Accelerator parameters for Run I and Run II configurations.*

2.2 The CDF II Detector

CDF II is a general purpose detector installed around one of two interaction points along the Tevatron ring, as shown in Figure 2.1. Looking at Figure 2.3, from inside to outside you can find: a tracking system, magnet, electromagnetic (EM) calorimetry, hadronic

calorimetry and finally the muon detectors. CDF II is also equipped with dedicated sub-detectors, such as a Time-of-Flight system and a Cherenkov Luminosity Counter.
In this Chapter we shall present a general description of the different subsystems of CDF detector, with a main focus on Tracking systems heavily used in this analysis.

2.2.1 Standard Definitions in CDF II

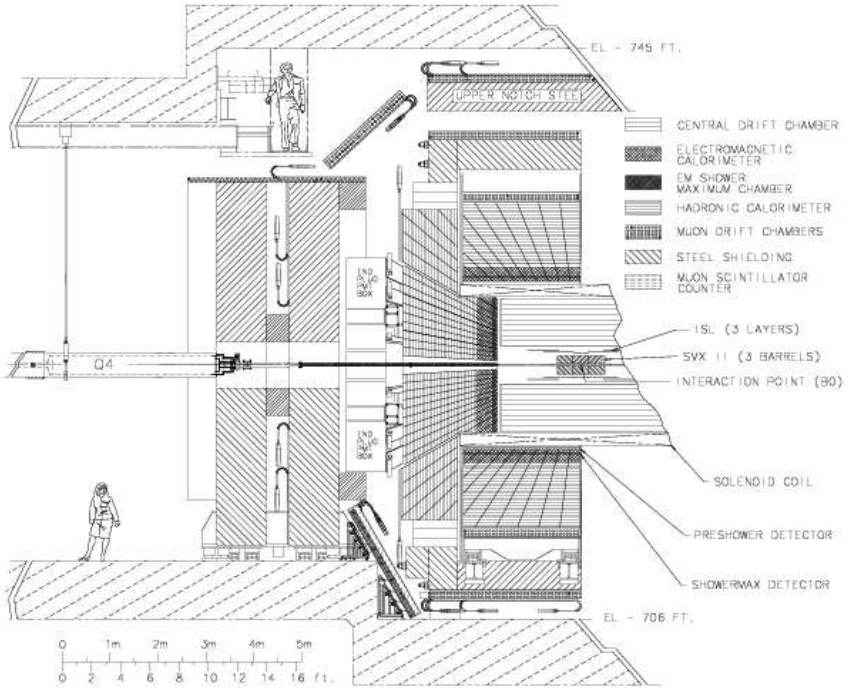

Figure 2.3: *CDF II Detector Layout.*

Before moving on sub-detectors description, it is helpful to present some common definitions used at CDF II. The Cartesian coordinate system associated with CDF II has the detector's geometric center as its origin. The x axis is in the (horizontal) plane of the accelerator ring, pointing radially outward, while the y axis points vertically up. The z axis is chosen to complete the right-handed coordinate system. Beams travel approximatively parallel to z axis with protons moving in the positive z direction. So the center of the detector roughly coincides with the center of the beam crossing region.
Anyway the detector is essentially a cylindrically and forward-backward symmetric device, making convenient to work with cylindrical (z, r, ϕ), or polar (r, θ, ϕ) coordinates. Following these conventions, one found that the azimuthal angle ϕ runs in the transverse (x-y) plane, with $\phi = 0$ being the positive direction of the x axis. The Polar angle θ is counted from the positive direction of z axis. The z axis is the same as in carting coordinates.
Another important coordinate is often used instead the polar angle θ, this is called pseudo-rapidity and it's defined as:

$$\eta = -\log \tan \frac{\theta}{2}. \tag{2.2}$$

The choice of a coordinate system such as (r, η, ϕ) is convenient because it is based on the experiment symmetries. The collisions processes are invariant under rotation under the (unpolarized) beam, making ϕ a natural choice. Then, the physics processes that take place in an hadronic colliders involve essentially the *partons* (can be valence or sea quarks or gluons) more than the protons or antiprotons. They carry only a fraction of the initial proton or antiproton momentum so, as a consequence of possible unbalance in the longitudinal components of the two momenta, the observed physics interactions often show large boosts along the z axis. Keeping in mind this statements, it can be easily shown that η is the relativistic/massless limit of the more common used quantity, the rapidity ξ, defined as:

$$\xi = -\frac{1}{2}\log\frac{E+p_z}{E-p_z}. \tag{2.3}$$

So the invariance under Lorentz boost is preserved for η, but now we have also a more clear geometrical association.
The detector components (whenever appropriate) were chosen to be uniformly segmented along η and ϕ coordinates, thus simplifying the analysis.

2.2.2 Tracking System

Charged particles cause ionization passing through matter. This phenomenon is typically localized near the trajectory of the particle within the matter in little clusters called *hits*. If detected, hits give geometrical information that can be used to reconstruct the particle's trajectory. The process of trajectories reconstruction is often called *tracking*.
The inner part of the CDF II is devoted to tracking system, because reconstructing the trajectories of charged particles near the collision point turns into the reconstruction of decay vertexes for long lived particles. To collect also the information of particle charge, the CDF II tracking volume is permeated by a uniform magnetic field directed along the z axis. So, within the tracking volume the charged particles move along helicoidal trajectories, which are described by the parameters:

- ✓ z_0 The z coordinate of the closest point to the z axis
- ✓ d_0 The Impact Parameter: the distance from the point of the closest approach to z axis
- ✓ ϕ_0 The ϕ direction of the transverse momentum of the particle (tangential to the helix) at the point of the closest approach to the z axis
- ✓ $\cot\theta$ The helix pitch, defined as the ratio of the helix step to its diameter
- ✓ C The helix curvature

The impact parameter and the curvature are signed quantities defined by :

$$C = \frac{q}{2R}, \tag{2.4}$$

$$d_0 = q(\sqrt{x_c^2 + y_c^2} - R), \tag{2.5}$$

where q is the charge of the particle, $(x_c^2 + y_c^2)$ is the center of the helix as projected onto the x-y plane and R is its radius. A graphical view of these variables together with the ϕ_0 is shown in Figure 2.4.

From helix parameters one can easily derive particle's transverse and longitudinal momenta:

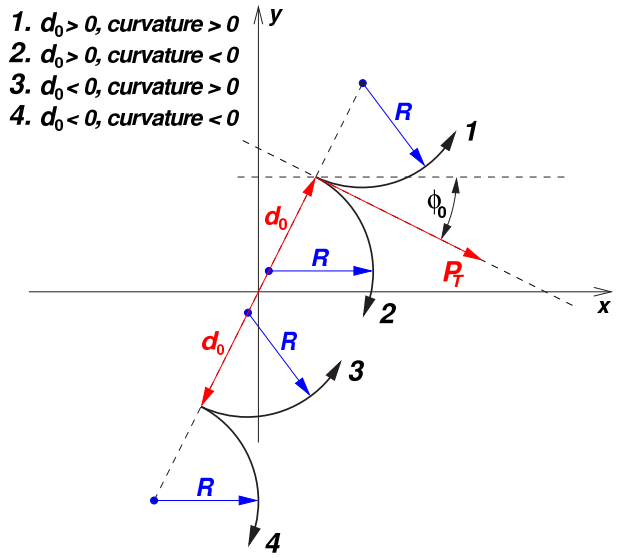

Figure 2.4: *Illustration of helix track parametrization.*

$$p_T = \frac{cB}{2|C|}, \tag{2.6}$$

$$p_z = p_T \cot\theta \tag{2.7}$$

The CDF II tracking system is essentially divided in an inner silicon strip detector, aiming to more precise vertices reconstruction, and an outer Drift Chamber that provides the necessary information for track's momentum definition. As shown in Figure 2.5, the overall tracking volume covers up to $|\eta| = 2$ region, allowing track's reconstruction in a wide volume.

Silicon Vertex Detector

As mentioned above, silicon tracking detectors are used to obtain precise measurements of the charged particle's path, and then a precise determination of the long lived particle's decay vertex.

The principle on which a silicon strip detector works is visualized on Figure 2.6. In practice it can be summarized as a reverse-biased p-n junction. In a typical silicon microstrip detector, over a lightly doped n-type silicon (n^-) substrate, roughly 300 μm thick, a series of finely spaced p-type silicon strips are inserted via implantation technique [20]. The opposite side is then equipped with a thin layer of strongly doped n-type silicon (n^+). A positive voltage is then applied to the n^+ side, depleting the bulk of free charge carriers

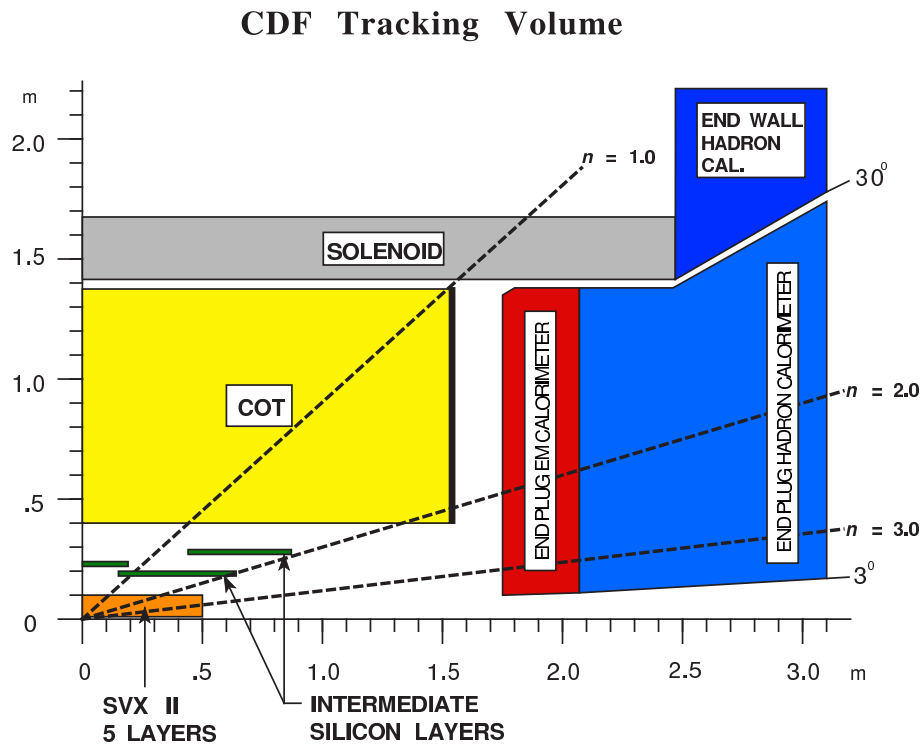

Figure 2.5: *The r-z view of The CDF II tracking system.*

(both electrons and holes) creating an electric field. When a charged particle crosses the active volume (i.e. the n^- substrate), it creates a column of electron-hole pairs from ionization along the particle path. The presence of the electric field drifts the holes to the p^+ implanted strips producing a well localized signal in r - ϕ plane.
The inter-strip spacing is typically around 60 μm, non the less the position measurement accuracy that can be achieved at CDF II is of 12 μm. This can be done using weighting technique. In fact, the signal is usually detected not by a single strip but on a small cluster of adjacent strips. So the hit position can be extracted by weighting the strip positions by the amount of charge collected by each strip.
The CDF II Silicon VerteX Detector, called SVX II [19], is composed by three different barrels 29 *cm* long each. Each barrel support five layers of double-sided silicon micro-strip detectors in the range of 2.5 to 10.7 *cm* from the beamline. The layers are numbered from

Layer	Radius [cm]		# of strips		Strip pitch [μm]		Stereo	Ladder Active, [mm]	
	stereo	r - ϕ	stereo	r - ϕ	stereo	r - ϕ	angle	width	length
0	2.55	3.00	256	256	60	141	90°	15.30	4×72.43
1	4.12	4.57	576	384	62	125.5	90°	23.75	4×72.43
2	6.52	7.02	640	640	60	60	+1.2°	38.34	4×72.43
3	8.22	8.72	512	768	60	141	90°	46.02	4×72.43
4	10.10	10.65	896	896	65	65	-1.2°	58.18	4×72.43

Table 2.2: *SVX summary.*

0 (innermost) to 4 (outermost). The Layers 0,1 and 3 combine an r - ϕ measurement on one side with the 90° stereo (r - z) on the other, while the Layers 2 and 4 combine an r - ϕ measurement with small angle stereo at 1.2° (Table 2.2). The active silicon crystals,

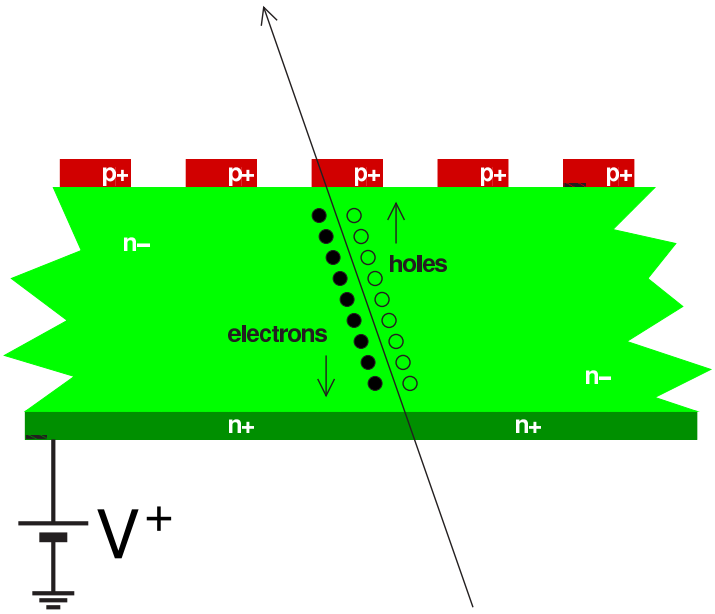

Figure 2.6: *Sketch of a generic silicon micro-strip detector.*

usually called wafers, are supported by weight substrates (Rohacell foam) in assemblies called ladders. The layout of these wafers is shown in Figure 2.7. There are four wafers connected by wire-bonds in each ladder. Twelve ladders of appropriate width compose a layer. Sixty ladders are mounted between two beryllium bulkheads making an SVX II barrel.
Each ladder is read out at both ends. The number of channels in the system (405,504) and the nature of the signals require that the electronics be physically mounted on the system. In fact the amount of cables that one should route out will be impossible to manage, more over a pre-amplification is needed to avoid noise increasing. The negative side of this, is that more passive material is brought inside the detector, increasing the effect of Coulomb scattering. Finally the built in electronics dissipates significant amount of heat over 1 kW, so to provide adequate cooling SVX II was designed to incorporate cooling channels into the bulkheads.
A measure of the SVX performances is the impact parameter resolution. Presently it is at about 40 μm, which includes 25-30 μm contribution from the beam width. Another benchmark is the z_0 resolution[4], which is at very respectable 70 μm.

Intermediate Silicon Layer and Layer 00

To reach better performances in terms of resolutions and tracking coverage two special sub detectors were subsequently added to the silicon tracker: the Intermediate Silicon Layer

[4]The quoted z_0 resolution has been obtained by tracks that have ISL hits on them. SVX stand-alone resolution is somewhat worse.

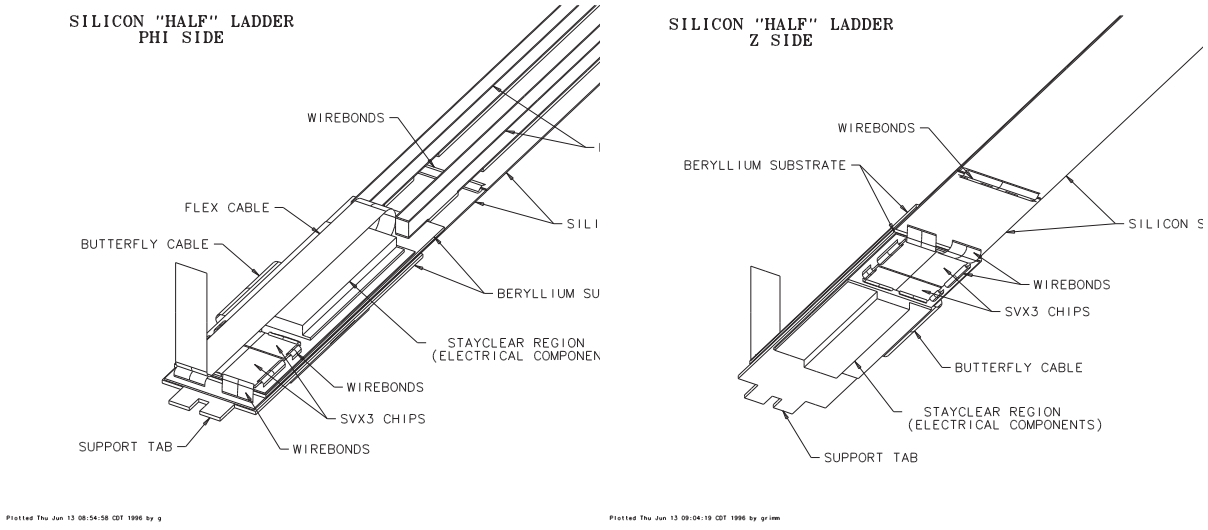

(a) top *(r - ϕ)* (b) bottom *(r - z)*

Figure 2.7: *Perspective view of the top (r - ϕ) and bottom (r - z) side of Layer 0 ladder.*

(ISL) and Layer 00 (L00) [21]. These two brand new detectors were not included in the *baseline project* for the CDF upgrade, turning onto some technical difficulties such space, time and money ... Due to these problems, the integration of the devices got relatively late.

ISL: In the central region a single ISL layer is placed at a radius of 22 *cm*. In the region $1.0 < |\eta| < 2.0$, two silicon layers are placed at radii of 20 and 28 *cm* (see Figure 2.5). Double sided silicon is used with 55 μm strip pitch on the axial side and 73 μm pitch on the stereo side with a 1.2° stereo angle. The read out is performed every other strip, in order to reduce the number of total read out channels, that count 268,800 units. This indeed affects the single hit resolution, which is about 16 μm on the axial side and 23 μm on the stereo side. Despite this fact ISL ladders are similar to the ones used for SVX.

L00: As can be seen in Figure 2.8, the L00 is a set of silicon strips assembled directly on the beam pipe. The design has six narrow and six wide groups of ladder in ϕ at radii 1.35 and 1.62 *cm* respectively, providing 128 read out channels for the narrower groups and 256 channels for the other groups. The silicon wafers are mounted on a carbon-fiber support which provides cooling also. L00 sensors are made of light-weight radiation-hard silicon (different from the ones used within SVX) and are single-sided with a 25(50) μm implant (readout) pitch. The ISL is intended to improve the tracking resolution in the central region, while in the $1.0 < |\eta| < 2.0$ region should provide a useful tool for a silicon stand alone tracking in conjunction with SVX layers. L00 instead, allows to overcome the effects of multiple scattering for tracks passing through high density regions of SVX

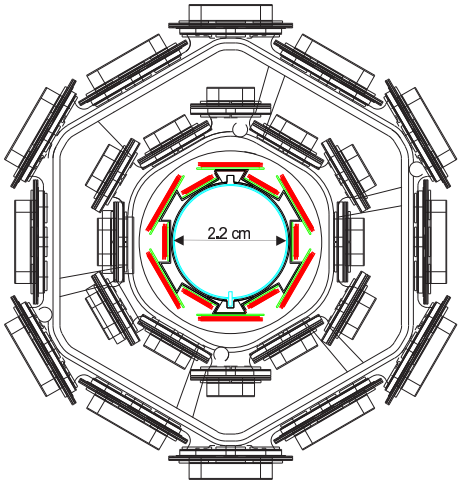

Figure 2.8: *Transverse view of Layer 00, the innermost silicon layer.*

(where the bulkheads and readout electronics are located) making possible to improve vertexing resolutions.

Central Outer Tracker

In addition to the silicon detector a drift chamber is used at larger radii to improve the momentum resolution. In the region $|z| < 155\ cm$ and between the radii of 43 and 133 cm takes place the Central Outer Tracker, COT. The COT [19], is a cylindrical multi-wire open-cell drift chamber with a mixture of 50:35:15 Ar-Ethane-CF4 gas used as active medium. The COT contains 96 sense wire layers, which are radially grouped into eight "superlayers" (See Figure 2.10). Each superlayer is divided in ϕ "supercells", and each supercell has 12 sense wires and it's designed so that the maximum drift distance is approximately the same for all supercells. Therefore, the number of supercells in a given superlayer scales approximately with the radius of the superlayer. Half of the 30,240 sense wires within the COT run along the z direction ("axial"), while the others are blow at a small angle (2°) with respect to the z direction ("stereo").
In this type of detectors a charged particle passing through the gas mixture leaves a trail of ionization electrons. These electrons are then drift toward sense wires of the cell where they are produced. The electrons drift is not only driven by an electrical field crated with this purpose, but also by the magnetic field present within the tracking volume. In such kind of fields electrons originally at rest move in the plane perpendicular to the magnetic field at an angle α with respect to the electric field lines. The value of α, the so called Lorentz angle, depends on both the magnitude of fields and the properties of the gas mixture. In the COT $\alpha \simeq 35°$.

Resolution-wise, the optimal situation is when the drift direction is perpendicular to that of the track. Usually the optimization is done for high p_T tracks, which are almost radial. Therefore all COT cells are tilted of 35° away from the radial, so that the ionization electrons drift in the ϕ direction. When the electrons get near the sense wire, the local field accelerates them causing further ionization. In brief an "avalanche" of ionized particles is produced, creating a signal (a hit) on a sense wire. Subsequently the signal

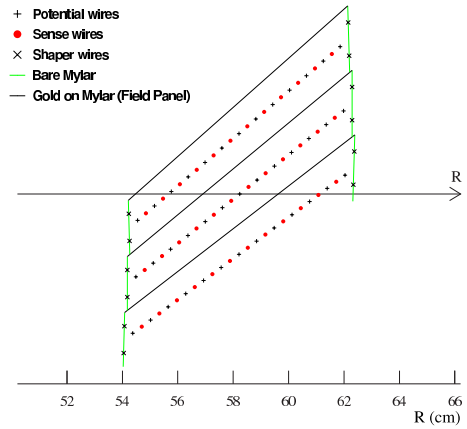

Figure 2.9: *Transverse view of three cells from the COT superlayer 2. The arrow shows the radial direction or, equivalently, a very high p_T track trajectory. The electric field is roughly perpendicular to the field panels; the drift velocity would be vertical in this picture. The angle between wire-plane of the central cell and the radial direction is 35˚.*

is amplified and shaped by the electronics attached at the end of the wire. So the r - ϕ position of the track with respect to the sense wire is inferred by the arrival time of the signal.
There are other advantages in doing the wire-plane tilt. For example, the tilt allows to overlap in the radial view, which means that high p_T tracks must pass very close to at least one wire in each superlayer. This is taken advantage by the eXtremely Fast Tracker (XFT) in the Level-1 trigger, as will be described in Section 3.2. Also the large tilt provides a lever in resolving the left/right ambiguity. Indeed, a particle passing by a wire-plane leaves several hits, which are grouped into a track segment, but since there is no way of knowing whether an individual hit is on the left of the respective wire or on the right of it, there are actually two segments, one the mirror image of the other. The angle between the two track segments ($\tan^{-1}(2 \cdot \tan\alpha) \approx 54°$) is large, which renders pattern recognition problem much easier.
A measure of COT performance is the single hit position resolution. It has been measured to be about 140 μm, which translates into the transverse momentum resolution $\frac{\delta p_T}{p_T} \sim 0.15\% \frac{p_T}{GeV/c}$.

Tracking and Vertexing

Before proceeding in this overall Detector review, it's important to introduce the basic concepts of tracks reconstruction at CDF II. Several algorithms were developed at CDF to reconstruct tracks, some use only the COT informations, other the silicon information only, others use both COT and silicon hits. The most used is the so called *Outside-In* algorithm [23]. The basic idea is to start the track reconstruction from the drift chamber and project the track into the silicon detector to find the hits that have to be used in the final determination of track's parameters.
Track reconstruction in the COT begins from finding matching track segments or just

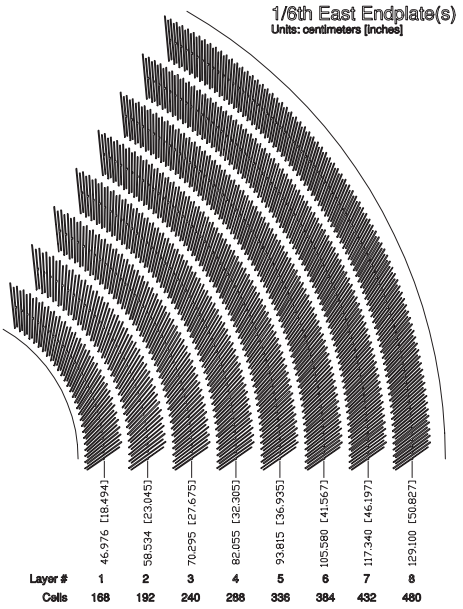

Figure 2.10: *Layout of wire planes on COT end-plate.*

individual hits in the axial superlayers [24]. When the r - ϕ projection of the track is reconstructed we get the measurement of C, d_0 and ϕ_0 helix parameters. When looked at in r - ϕ plane, hits from stereo superlayers appear to be offset from the reconstructed helix projection. The amount of the offset is proportional to the z coordinate. Proper matching of stereo superlayer segments/hits to existing r - ϕ track projection allows to extract z information of the track at 4 radial regions thereby measurement $\cot\theta$ and z_0 parameters of the helix.
It's crucial to mention that the global CDF coordinate system, introduced at the beginning of the Section 2.2.1 is anchored to the center of the COT, i.e. the COT cylinder axis is the z axis of the global CDF coordinate system, and the center of the COT is its origin. Positions of other detector components are measured[5] with respect to the COT reference frame and encoded in so-called *alignments tables*. Whenever a spatial measurement is done by a system other than the COT, it is usually done in the local reference frame and then converted into the global CDF (w.r.t. COT) reference frame, via the respective alignment table. One example of this procedure concerns the Silicon Vertex Detector, described in previous paragraph.
As said before, tracking can be performed using only the silicon informations, so that a dedicated alignment effort has to be done in order to have high precision tracks measurement. In fact, every effort is made to place the SVX barrels in a coaxial manner. Remaining (small) spatial shifts are accounted for by barrel-to-barrel alignment. For the purpose of triggering[6] it is much more important to place SVX symmetrically around the beam than that of the z axis of the detector. This results in the fact that the SVX axis

[5]Measurement are performed mechanically, by means of optical survey, or , when the ultimate precision is needed and the possibility exists, with data .

[6]Certain triggers rely on the d_0 track parameter as measured by SVX. In case the beamline does not coincide with the SVX axis d_0 (and consequently, the triggers) became ϕ-dependent!

is offset from the COT axis by about the same amount that the beamline differs from the z axis of the detector.

To complete the helical fit for the track in the best way [24], SVX and COT information have to be combined, when all SVX hits (some of which may be fakes) are found. At this point, it is absolutely important to have a very good alignment table, so that the positions of the SVX hits, originally measured only with respect to individual ladders, are translated correctly into the global (COT) reference frame. Then, using this information, SVX and COT hits can be combined to extrapolate the tracks parameters. The process starts when a track is reconstructed with the COT informations only (The so-called COT-only track). This track, because the parameters uncertainties is more like a tube of radius σ, determined by the errors on the track parameters. As additional complication σ, does not have to be the same in ϕ and z directions.
Thereby the COT-only track is extrapolated through the SVX. As extrapolation proceeds from the outermost SVX layer toward the beampipe, the track error matrix is updated to reflect the amount of scattering material transversed. At each SVX layer, hits that are within a certain radius[7] are appended to the track and track re-fit is performed. A new track candidate is generated for each of the newly appended hits, but only the best two (in terms of the fit quality and the number of hit) are retained. Each of these candidates is then extrapolated further in, where the process is repeated. At the end there may still be several candidates associated to the original COT-only track. In this case, a selection is done in the number of hits and then in terms of fit quality.

Precise determination of track parameters allows to discern which tracks came from what vertex and thereby to distinguish the *primary* vertex (PV) from the *secondary* vertex (SV), such as a B hadron or other long-lived particle decay vertex.

2.2.3 Calorimeter Apparatus

Even if not used in this analysis, the calorimeter system, together with the muon and tracking systems, is one of the main sub-detector apparatus of CDF II detector.
The CDF II calorimetry system has been designed to measure energy and direction of neutral and charged particles leaving the tracking region. In particular, it is devoted to jet reconstruction and it is also used to measure the missing energy associated to neutrinos.

Particles hitting the calorimeter can be divided in two classes, according to their main interaction with the matter: electromagnetically interacting particles, such as electron and photon, and hadronically interacting particles, such as mesons or barions produced in hadronization processes. To detect these two classes of particles, two different calorimetric parts have been developed: an inner electromagnetic and an outer hadronic section, providing coverage up to $|\eta|$ <3.64. In order to supply information on particle position, the calorimeter is also segmented in radial sections, called towers, projected toward the

[7] Often the radius defined as some multiple of σ rather than an absolute number because σ changes as hits are being added.

	Thickness	number of layers	Resolution (E in GeV)
CEM	19 X_0	20-30 Pb:3mm,Scint.:5mm	$13.5\%\sqrt{E\sin\theta}\oplus 2\%$
PEM	21 X_0	22 Pb:4.5mm,Scint.:4mm + Preshower	$16\%\sqrt{E\sin\theta}\oplus 1\%$
CHA/WHA	4.7/4.5 λ_0	32/15 Fe:25/50 mm, Scint.:10 mm	$75/\%/\sqrt{E\sin\theta}\oplus 3\%$
PHA	7 λ_0	23 Fe:51 mm, Scint.:6mm	$80\%\sqrt{E\sin\theta}\oplus 5\%$

Table 2.3: *Basic quantities characterizing CDF II calorimetry.*

geometrical center of the detector. Each tower consists of alternating layers of passive material and scintillator tiles. The signal is read out via wavelength shifters WLS embedded in the scintillator and light from WLS is then carried by light guides to photomultiplier tubes. The central sector of the calorimeter, covering the region $|\eta|$ <1.1, was recycled from Run I, while brand new calorimeters (called plug calorimeters) were built up to cover the forward and backward regions.

The Central Calorimeter

Apart from upgrades on the readout electronics, needed to follow the increased collision rate, the central calorimeter is almost the same used during Run I [19] . The Central Electro-Magnetic calorimeter (CEM) is segmented in $\Delta\eta\times\Delta\phi$=0.11×15° projective towers consisting of alternate layers of lead and scintillator, while the Central and End Wall HAdronic calorimeters (CHA and CWA respectively), whose geometry tower segmentation matches the CEM one, use iron layers as radiators. A perspective view of a central electromagnetic calorimeter module (*wedge*) is shown in Figure 2.11 (a), where both the arrangement in projected towers and the light-gatering system are visible.
The projective geometry has been used in order to take advantage of the momentum conservation in the transverse plane: before the $p\bar{p}$ collision, the projection in the transverse plane w.r.t. the beam direction of the beam energy is zero, therefore this quantity have to be the same also after the collision took place. Thus, the for each tower the *transverse energy* E_T is defined as $E_T = E\cdot\sin\theta$, where E is the energy detected by the tower and θ is the angle between the beam axis and the tower direction, in the CDF detector coordinates system. Two position detectors are embedded in each wedge of CEM:

- The Central Electromagnetic Strip chamber (CES) is a two-dimensional stripwire chamber arranged in correspondence to maximum shower development ($\sim 5.9X_0$). It measures the charge deposit of the electromagnetic showers, providing information on their pulse-height and position with a finer azimuthal segmentation than calorimeter towers. This results in an increased purity on electromagnetic object reconstruction.

- The Central Pre-Radiator (CPR) consists of two wire camber modules placed immediately in front of the calorimeter. It acts as pre-shower detector by using the

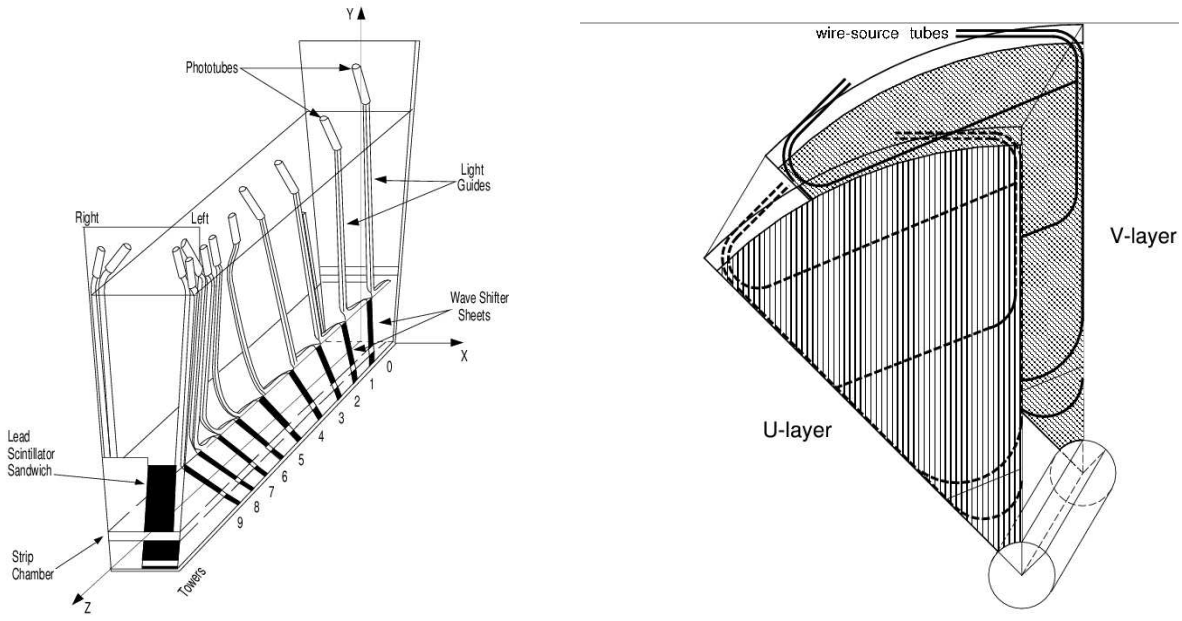

(a) (b)

Figure 2.11: *Perspective view of a CEM module (a) and of SIMD (b).*

tracker and the solenoid coil material as radiators, resulting to be a very useful tool in rejection of electron and photon background.

Calorimeter response is fast enough to match the time requirements imposed by Run II. However, wire chambers associated to CES and CPR may need to be integrated over several beam crossings; this will not be a problem since the high granularity of these devices guarantees a low detector occupancy.
Table 2.3 summarize the basic quantities of calorimeter detectors.

The Plug Calorimeter

The plug calorimeter, covers the η region from 1.1 to 3.64. The new configuration, based on the same principles as the central calorimeter, allows the detector to operate in the Run II environment and makes experimental data more homogeneous. Both electromagnetic and hadronic sectors are divided in 12 concentric η regions, with $\Delta\eta$ ranging from 0.10 to 0.64, according to increasing pseudorapidity, each of them is segmented in 48 or 24 (for $|\eta| < 2.11$ or $|\eta| > 2.11$ respectively) projective towers. The actual size of these towers was chosen so that identification of electron in b-jets would be optimized.

Projective towers consist in alternating layers of absorbing material (lead and iron for electromagnetic and hadronic sector respectively) and scintillator tiles. The first layer of the electromagnetic tile is thicker (10 mm instead of 6 mm) and made of material with

higher photon yield. They act as a pre-shower detector.
As in the central calorimeter, a Shower Maximum Detector (SMD) is also included in the plug electromagnetic calorimeter, at a radial depth of $\sim 6\ X_0$. The SMD consists of eight 45° azimuthal sectors, each covering six (or three) calorimetric towers in ϕ. Furthermore, each detector is segmented in two η regions in order to reduce detector occupancy. Within each region, 5 *mm* pitch scintillating strips are arranged on two layers (called U and V). Being parallel to either boundary of the sector, U and V strips from an angle of 45° among them (see Figure 2.11 (b)), providing a two dimensional measurement of the shower. The SMD is a useful tool to discriminate photons and electrons from pion background.

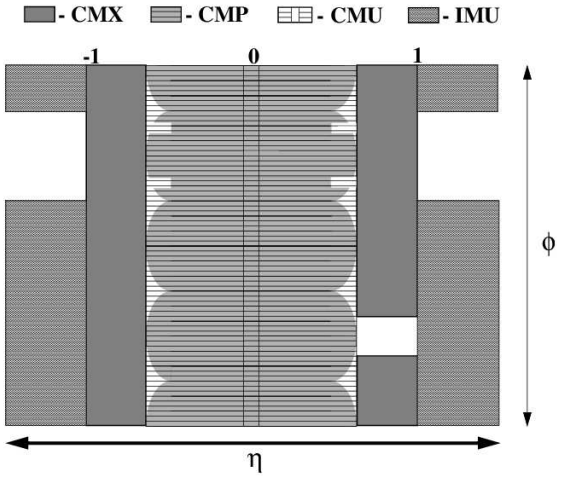

Figure 2.12: $\eta - \phi$ *coverage of the Run II muon system.*

2.2.4 Muon Detectors

Thanks to their high penetration power, muons are separated from surrounding particles by the calorimeter, that acts as a shield on electromagnetic and hadronic matter. Muon identification can therefore be performed by extrapolating the tracks outside the calorimeter and matching them to tracks segments (called *stubs*) reconstructed in an external muon detector.
Figure 2.12 shows an overview of the coverage of the muon detectors. To this purpose, muon system has been equipped with several devices:

- Central MUon detector (CMU) consists of a set of 144 modules, each containing four layers of rectangular drift cells, operating in proportional mode. It is placed immediately outside the calorimeter and supplies a global coverage up to $|\eta|$ <0.6; ϕ measurement of muon position is guaranteed by azimuthal segmentation of the detector, while z coordinate is estimated on the basis of charge division.

- Central Muon uPgrade (CMP) consists of four layers of single-wire proportional drift tubes stagged by half cell per layer and shielded by an additional 60 *cm* steel layer. It is arranged in a square box around the CMU, providing a ϕ-dependent η

coverage (see Figure 2.12) according to the cylindrical structure of the inner detector. Contrary to CMU, this device supplies only ϕ information. For Run II, CMP benefits of an increased acceptance of $\sim 17\%$.

- Central Scintillator uPgrade (CSP) is a layer of rectangular scintillator counters placed on the outer surface of CMP.

- Central Muon eXtension (CMX) consists of a stack of eight proportional drift tubes, arranged in conical sections to extend the CMU/CMP coverage in the $0.6 < |\eta| < 1$ region. Azimuthal acceptance has been improved by 45% for Run II; only a 30° ϕ-gap remains to be used by the solenoid cryogenic system.

- Central Scintillator eXtension (CSX) consists of a layer of scintillator counters on both sides of CMX. Thanks to scintillator timing, this device completes with z information the measurement of ϕ position of muons provided by CMX.

- Intermediate MUon detector (IMU) replaces the old Forward Muon Detector (FMU) to exploit the improved tracking capabilities and perform muon momentum measurement based only on the central solenoid field. In fact, during Run I the momentum of forward muons had to be measured by the FMU itself through a toroidal magnet; steel toroids are now used to supply mechanical support and shielding to new detector. IMU consists of four staggered layers of proportional drift tubes and two layers of scintillator tiles, arranged as for the CMP/CSP system to extend triggering and identification of muons up to $|\eta| \leq 1.5$ and $|\eta| \leq 2$ respectively.

Due to their slow response, muon chambers are not able to work within the Run II inter bunch interval of 400 to 132 ns. However, detector occupancy is expected to be strongly reduced with respect to Run I thanks to the accelerator upgrades[8] and to stronger shielding from beam halo. Together with the high granularity of the muon devices, it would allow to integrate the collected signals over several beam crosses.

2.2.5 Other Systems

In this section we review the remaining systems. These are not directly involved in the presented analysis, and a brief summary is given.

TOF

The Time-Of-Flight system (TOF), expands the CDF's particle identification capability in the low p_T region. TOF measures arrival time t of a particle with respect to the

[8]More than 95% of the ionization detected in the muon system during the Run I resulted to be originated by the Main Ring, that has been replaced by the Main Injector.

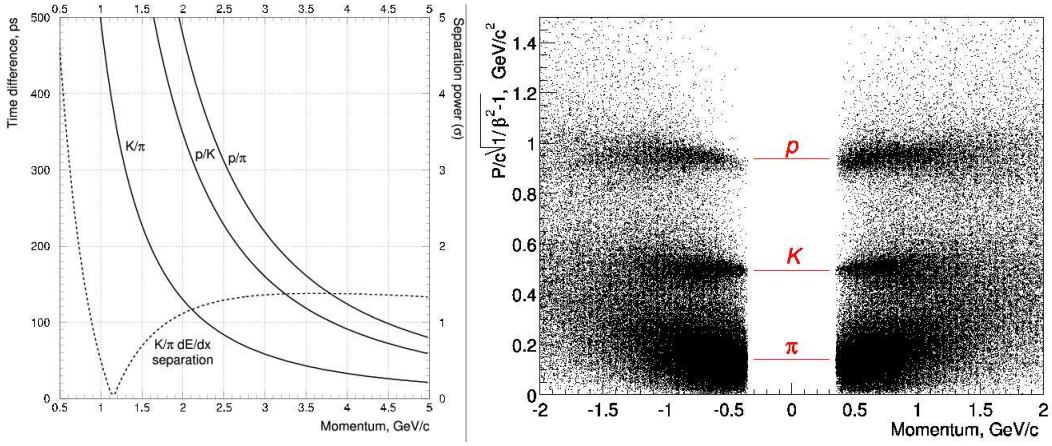

(a) K/π, p/π and K/p difference over a path of 140 cm as a function of momentum, expressed in ps and separation power(σ), assuming resolution of 100 ps. The dashed line shows the K/π separation power from dE/dx measurement by the COT.

(b) TOF reconstruction mass vs. momentum for positive and negative tracks. Cluster of data points corresponding to π, K and p are clearly visible. Data are from Tevatron store 860 (12/23/2001).

Figure 2.13: *Time-Of-Flight system performance: design (a) and data (b).*

collision time t_0. The mass m of the particle is then determined using the path length L and momentum p measured by the tracking system via relationship

$$m = \frac{p}{c}\sqrt{\frac{(ct)^2}{L^2} - 1}. \tag{2.8}$$

The TOF consists of 216 CB-408 scintillator bars installed at a radius of about 138 cm (from the z axis) in the 4.7 cm space between the outer shell of the COT and the cryostat of the superconducting solenoid (see Figure 2.5). Bars are approximatively 279 cm long and $4 \times 4\,cm^2$ in cross-section. With cylindrical geometry TOF provides 2π coverage in ϕ and roughly (-1;1) coverage in η.
Bars are read out at both ends by fine-mesh PMTs (Hamamatsu R7761), capable of providing adequate gain even if used inside 1.4T magnetic field. Usage of long attenuation length fast rises time scintillator in conjunction with these PMTs allowed to achieve specified resolution of 100 ps.
Figure 2.13 (a) shows time-of-flight difference for K/π, p/π and K/p hypotheses and the separation power assuming resolution of 100 ps. In Figure 2.13 (b) early TOF performance is illustrated.
More details on TOF construction and performances can be found in Reference [21].

CLC

The Cherenkov Luminosity Counter (CLC), measures the average number of interactions per bunch crossing μ. Then instantaneous luminosity $\mathcal{L}$ is extracted using the following formula:

$$\mu \cdot f_{bc} = \sigma_{p\bar{p}} \cdot \mathcal{L} \tag{2.9}$$

where $\sigma_{p\bar{p}}$ is relatively well known total $p\bar{p}$ cross=section at $\sqrt{s} = 1.96\,TeV$ and f_{bc} is the rate of bunch crossings in the Tevatron.

The CLC exploits the effect, known as Cherenkov radiation. Particles traversing a medium at a speed higher than the speed of the light in this medium, radiate light into a cone around particle direction; cone's opening angle depends on the ratio of the two speeds and the refraction index of the medium.
The idea is to use an assembly of long gas-filled Cherenkov counters positioned in the Plug Calorimeter 3^d gap, so that they point toward the interaction region, as schematically shown in Figure 2.14. This arrangement allows to make the detector much more sensitive to the particles coming directly from the interaction point because their flight path in the gas of the counter is the longest, and therefore the amount of the light produced the largest.

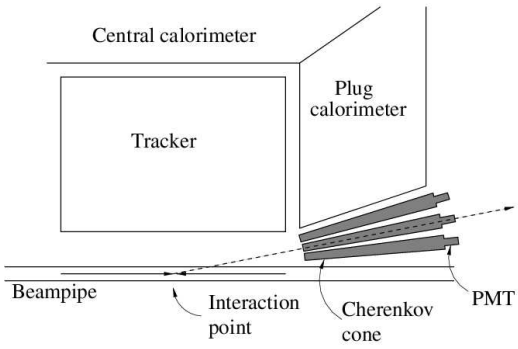

Figure 2.14: *CLC geometry.*

Excellent timing resolution ($\sim 50\,ps$) and clever design allow the CLC to discern multiple interactions within the same bunch crossing and achieve an overall accuracy of the luminosity measurement better than 5%.
Further information on the CLC design and performance is given in References [38] [39] [40].

Chapter 3

The CDF II Trigger

In the Tevatron collider, protons and antiprotons collide every 396 *ns. At the energy of* $\sqrt{s} \simeq 2\ TeV$ *and Luminosity* $\sim 6 \times 10^{31}\ cm^{-1}s^{-1}$*, this means we have roughly one interaction per bunch crossing, and equivalently one event every 396 ns. This collision rate is too high to record all the events. In fact CDF has mass storage capability of* $\sim 100\ Hz$*, while the collision rate provides an output of roughly* $2.5\ MHz$*. Therefore a selection have to be performed to reduce the event rate. More over, even with a higher recording speed, keeping all the produced events would result in 300 TB of data in one week of running, that will be too much expensive... However, most processes of interest have cross-sections in range of 10-100* μb *or smaller, i.e., at least three orders of magnitude smaller than the total* $p\bar{p}$ *cross-section. This fact allows one to perform a preliminary on-the-fly selection recording only the most interesting events: The trigger.*

3.1 Triggering

CDF II is equipped with a 3-levels trigger. At each level, only part of the all available informations are used to built some *primitives*, subsequently used to select the interesting events. At every level the primitive variables are even more complete, and the trigger selections are more accurate and more efficient. The design of the fully pipelined data acquisition system and the three-level deadtimeless trigger is pictured in Figure 3.1.
Level-1 trigger discards the vast majority of the event. Since it can take as long as 5.5 μs for the Level-1 to reach its decision, all front-end electronics are equipped with buffers 14 bunch crossing deep. If Level-1 does not reject an event it proceeds to the Level-2. The Level-2 does a more careful analysis of the information, taking longer time (few tens of microseconds) to do it. The entire detector is read out for the Level-3 decision only if Level-2 pass.

The Level-1/Level-2 trigger system is managed by the Trigger Supervisor Interface (TSI/CLK box in Figure 3.1 (b)). TSI also provides an interface between the triggers and the DAQ as well as global clock and a bunch crossing signal. In the case of Level-2 accept, the digitized output from all detector components is collected and transferred to the Event Builder. There, the event fragments obtained from different subsystems are organized into a properly ordered sequence, which is then fed to Level-3 computing farm. At the Level-3 the event undergoes fairly thorough reconstruction after which final

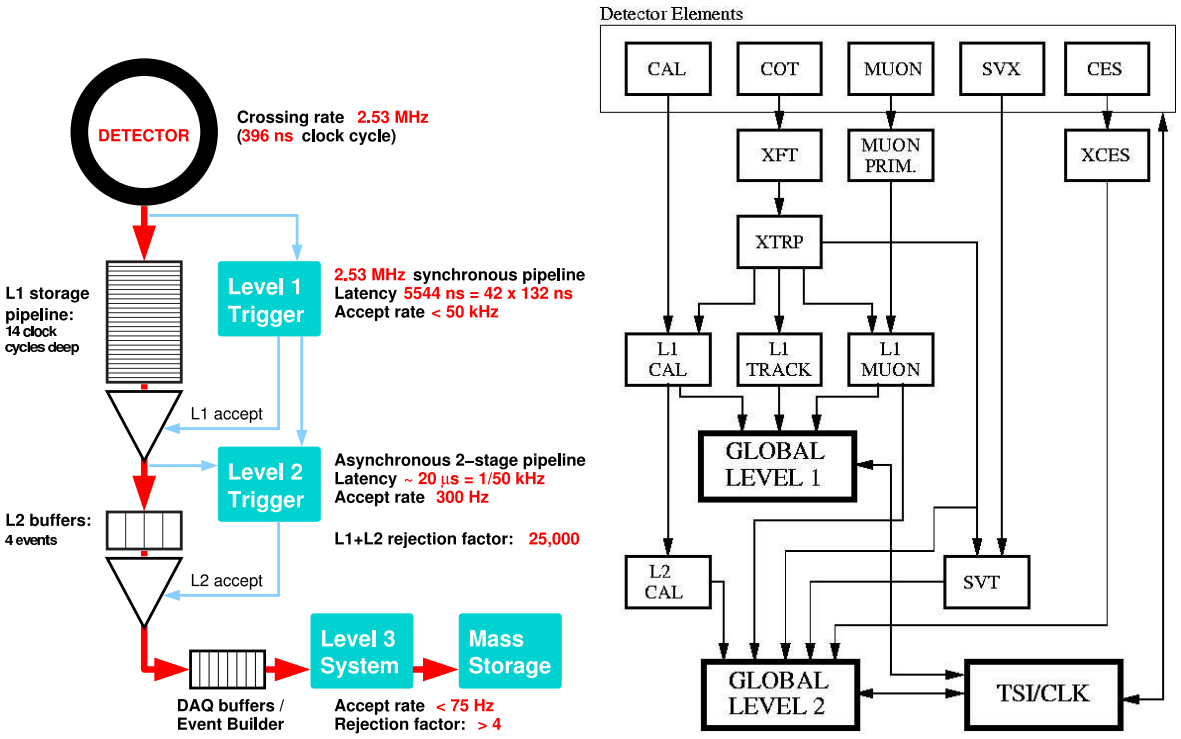

(a) CDF readout functional diagram

(b) Block diagram of the CDF trigger system

Figure 3.1: *Block diagram detailing CDF DAQ and L1/L2 trigger system.*

requirements are applied. If these are satisfied the event gets written to a mass storage device.
At every level the decision process can follow different rules, depending on the physics process to be selected.

Below, we discuss CDF II trigger and data acquisition system, relevant to our analysis. The conceptual design of the entire system is presented in Reference [25] and an elaborate description is given in Reference [19].

3.2 The Level 1 Trigger

The Level-1 is a synchronous system with an event read-in and an accept/reject decision, made every bunch crossing. The decision is based on transverse energy in the calorimeters, tracks in the COT and stubs in CMU, CMX and CMP chambers. Level-1 uses rudimentary (no detailed reconstruction) versions of the above mentioned objects, called *primitives*.
In several cases tracks primitives are combined with calorimeter or muon primitives to form e, μ and jet objects as shown by arrows in Figure 3.1 (b).
To ensure the maximum speed, Level-1 uses custom designed hardware. The total rate of Level-1 accept is about few tens of KHz, a factor of few hundred smaller than the input

rate of 2.5 MHz.
There are many algorithms (or, equivalently, individual triggers) at the Level-1 [26]. In this analysis we used a forerunner trigger which selects couple of tracks with significant non zero impact parameter and called Two Tracks hadronic Trigger. We shall discuss it in Section 3.5 in more details. The rest of this Section will be devoted to introduce two important systems for L1-triggering, XFT and XTRP, which provide information to be incorporated into decision making process for several separate Level-1 triggers, including the Two Track Trigger.

XFT and XTRP

The track reconstruction at Level-1 is performed by XFT [27], the eXtremely Fast Tracker, which identifies the track primitives (high p_T tracks[1] in r - ϕ view) using the four axial superlayers of the COT. Track identification is accomplished in two steps: segment finding and segment linking. In the finding step, all COT axial hits are classified as either "prompt" (drift time less then $44ns$) or "delayed" ($44ns$ < drift time < 132 ns). Then a set of binary masks (predefined patterns of prompt/delayed hits) is applied in order to find all segments compatible with a valid track[2] passing through a given superlayer. For a successful match a "pixel" is set. This pixel represents the ϕ position of the segment plus a slope information in the two outermost axial superlayers (needed to resolve the charge). In the second step (linking) four pixels appearing to have come from the same track are identified and a crude estimate of track parameters is done. These tracks are reported to the XTRP (the eXTRaPolator unit) unit and a copy of them is preserved to be used in the Level-2.
XTRP, is responsible for quick extrapolating of the XFT tracks to other detector subsystems such as calorimetry and muon chambers (see Figure 3.1 (b)). Matching these tracks with electron towers (EM calorimeter) or muon stubs (muon chambers) allows the construction of more complex primitives and, therefore, an additional rejection at Level-1.

The trigger selection criteria developed for the trigger dataset used in this analysis (called hadronic datasets), do not require any other detector's information but some track parameters. So the Level-1 Decision is performed, for this kind of trigger, with XFT informations only. The XFT reports to XTRP the p_T, ϕ_{SL6} (ϕ at the COT superlayer 6) and charge informations for each detected track. Different trigger paths can need muon or calorimeter informations (L1MUON and L1CAL respectively). These are extracted by dedicated boards and sent to XTRP for the final Level-1 characterization and then to the Global Level-1 Board for the ultimate decision. Finally if an event is not rejected by the Level-1 trigger decision, it is automatically passed to the Level-2 system.

[1] High p_T tracks are tracks with $p_T > 1.5\ GeV/c$.
[2] The one that originates in the vicinity of the beamline and has high enough p_T .

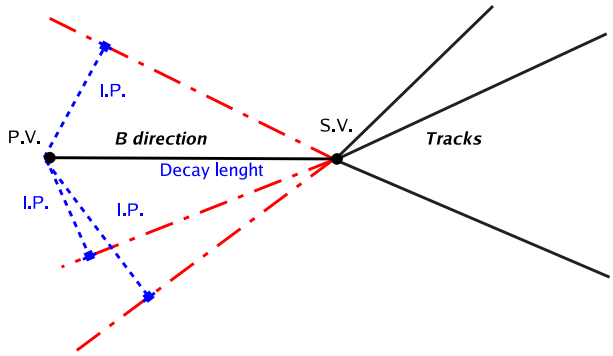

Figure 3.2: *Schematic chart showing the correlation between the tracks I.P. and the decay length of a hypothetic B meson decay.*

3.3 The Level 2 Trigger

The Level-2 is an asynchronous system which processes events accepted by the Level-1 in the time-ordered fashion. It uses Level-1 primitives as well additional data coming from the shower maximum strip chambers (CES) in the central calorimeter and the r - ϕ strips of the SVX as indicated in Figure 3.1 (b). There are three hardware subsystems building primitives at the Level-2: L2CAL, XSEC and SVT.
Briefly L2CAL hardware receives trigger towers from L1CAL and finds energy tower clusters by applying seed and shoulder thresholds. That is, starting from the tower with highest energy deposit (seed tower), nearest towers are subsequently added to the seed if their energy is higher than an fixed value (the shoulder threshold) creating, in that way, a cluster.
The XSEC system generates bitmap of strips above certain threshold in the shower maximum chambers (8 bits per 15°). Then XFT track primitives are extrapolated by the XTRP to the CES radius and fed to the XSEC where they are matched with the strip bitmap, producing electron candidates.
The SVT uses SVX r - ϕ hits to extend XFT track primitives inside the SVX volume, closer to beamline. The SVT improves the XFT ϕ_0 and p_T resolutions and adds the measurement of the impact parameter d_0 (original XFT track primitives are beamline constrained). Acting into the impact parameter have is a very useful handle in order to select hadronic decay modes of heavy mesons. As shown in Fig. 3.2, the impact parameter of decay products is strongly related to the decay length of the *mother* meson, therefore a selection based on the tracks impact parameter turns directly in to a proper time requirement.
This innovative system is the core of all the trigger systems for B physics, and will be described in further details in the next subsection.

3.3.1 SVT

The Silicon Vertex Tracker (SVT) [28][29][30][31] is the most significant addition to Level-2 trigger system from Run I. This is an innovative device that exploits the potential of

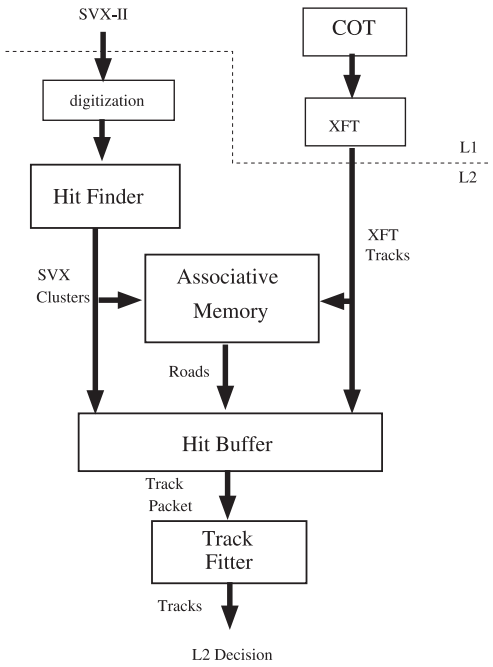

Figure 3.3: *The SVT architecture.*

a high precision silicon vertex detector to trigger on tracks significantly displaced from the $p\bar{p}$ interaction point. This can make accessible a large number of important processes involving decays of b-hadrons with a long lifetime.
SVT is a sophisticated device able to perform track reconstruction in the r - ϕ plane; its overall architecture is shown in Figure 3.3. The event flow can be summarized as follows: first, each of the 72 SVX II sectors[3] is read out by the *Hit Finder* , that performs a hit clustering on each layer contained in the sector. For each cluster found, the Hit Finder computes the centroid, representing the most probable intersection point between the trajectory of a particle and the layer that cluster belongs to. The outputs of the Hit Finder of each SVX II wedge are merged into one stream and fed both into an *Associative Memory* (AM) [33] and into a *Hit Buffer* [32], together with track primitives informations from XFT. The task of the Associative Memory is to perform the first stage of the pattern recognition [34]: cluster centroids from the Hit Finder are mapped in *superstrips*; then, all possible combinations of superstrips and XFT tracks are compared to a pre-established set of admissible combinations (*roads*), each corresponding to a set of four SVX II superstrips and an outer XFT track. Superstrip size results from a compromise between a precise pattern recognition which requires a large memory, and a coarse one, which introduces a lot of fake track candidates but small costs. The present choice is 300 μm. The result from the pattern recognition performed by the Associative Memory is finally stored into the *Hit Buffer* [32] together to the SVX clusters and XFT tracks informations. Now a road represent some kind of pipe where to perform a more detailed track reconstruction. The *Track Fitters* takes care of that, fitting the track informations from the Hit Buffer

[3]As described in the previous Chapter SVX II is composed by 3 barrels with 24 ϕ-wedges each.

by means of a linear approximated algorithm, consisting of a set of scalar products [35]. Hence, for each track, p_T, ϕ_0 and d_0 are computed.

The Hit Finder, Hit Buffer and the AM, constitute the first stage in building the primitives and are hardware based. The second stage,(the linear fit) is performed by four programmable processors (Alpha), which operate on list objects provided by the first stage. The Level-2 latency time is 20 - 30 μs, which along with the buffers for four events allows to bring the event rate from tens of KHz down to 300 - 350 Hz, the input bandwidth for Level-3.
For tracks with $p_T > 2$ GeV/c the SVT resolutions are found to be $\sigma_{d_0} = 35\mu m$, $\sigma_\phi = 1mrad$ and $\sigma_{p_T}/p_T = 0.003$ c/GeV [70]. In fact the width of the Gaussian fit for the distribution of measured track impact parameters is 47 μm. This is a combination of the intrinsic impact parameter resolution of the SVT measurement, and the transverse intensity profile of the interaction region. This profile is roughly circular and can be approximated by a Gaussian of $\sim 35\mu m$ resolution. Thus, the intrinsic SVT resolution is obtained by subtracting the beamline width from the width of the d_0 distribution by the use of the following relation:

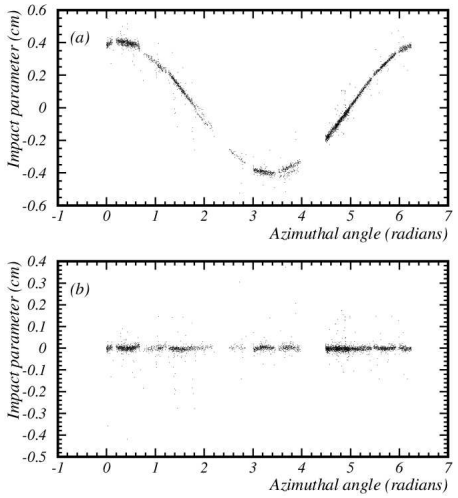

Figure 3.4: *Impact parameter (d_0) vs azimuthal angle (ϕ_0) plot using SVT variables after (top) and before (bottom) beam position correction has been done.*

$$\sigma_{SVT} = \sqrt{\sigma^2_{Measured} - \sigma^2_{Beam}} \tag{3.1}$$

At that time, all the track quantities refer to the origin of the coordinates system, *i.e.* the center of the COT. Clearly, the $p\bar{p}$ beam cannot be controlled with a infinite precision, and even if a lot of efforts have been done to keep it stable, usually it does not lie in the z axis and some kind of slope is present in both r - ϕ and $z - y$ plane projections. This problem, together with the fact that beam resolution in the z axis is around 30 cm, forced CDF to create a dedicated database where the beam properties are stored for each stable condition of data acquisition, the SVT alignment tables. The beam properties are measured in the first moments of data taking with stable beam condition.
Such as measurement is done looking at the correlation between the track impact parameter d_0 and the angular position ϕ_0. In absence on any bias there isn't any correlation between the two variables, while whenever the beam position differs from the nominal one a sinusoidal correlation appears in between d_0 and ϕ_0. This correlation is used to correct the track parameters and is used iteratively until it disappears (Fig.: 3.4). When the correcting factor are found they are written in the SVT alignment table and becomes available for the next events. Finally the SVT corrects the impact parameter and angular position of each track for the beam position in order to operate the trigger selection in

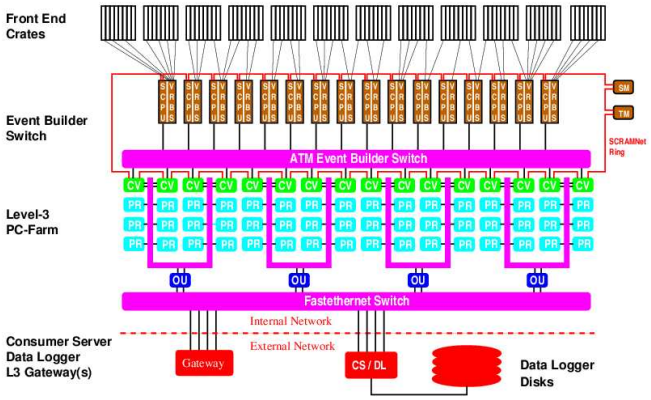

Figure 3.5: *Event Builder and L3 operating principle. All the main components are shown: ATM switch (purple), converter nodes (green), output nodes (dark blue), Consumer Sever and data logging System (red).*

an unbiased way. All the Level-2 primitives are then sent to the Global Level-2 decision board, that perform the event rejection according to the different trigger requirements of every trigger path.

3.4 The Level 3 Trigger

When an event is Level-2 accepted, the entire detector is read out, and thereby a slot in all the detector buffers is emptied for the next event. The read out event fragments are put in the proper order by the Asynchronous Transfer Mode (ATM) switch based system known as the Event Builder [37], and then arranged event fragments are channeled to the Level-3.
Level-3 [37] is a farm of conventional PCs running Linux. The farm is split in a number of 16 sub-farms of identical architecture. Each sub-farm consists of a head node (also known as converter node) and 12-16 processor nodes. There are also eight so-called output nodes in the Level-3, each is shared by two sub-farms.
Figure 3.5 shows the implementation of the Level-3 farm. Data from the front end crates is prepared by Scanner CPU's (SCPU) and fed into the ATM switch. On the other side it is the converter node that receives an ordered sequence of event fragments from the Event Builder. In the converter node these fragments are assembled in a block of data, called the *event record*, suitable for analysis by CDF software. From then on, the event record becomes the one and only piece of information about a particular event.
Each event record is fed to one of the processor nodes in the sub-farm, where event reconstruction is performed and final trigger requirements are applied. At this stage Level-3 takes advantage of the full detector information and improved resolution, not available at the lower trigger levels. Therefore tracks are reconstructed using tridimensional algorithms and both COT and SVX informations, match is performed with the muon stubs or calorimetric deposit in order to identify muons and electrons candidates, and calorimetric

energy is clustered with more detailed algorithms to generate jet candidates. Dedicated alignment tables and detector calibrations are applied at this level also. If an event satisfies Level-3 requirements, the corresponding event record gets passed to the output node which subsequently transfers it to the mass storage via the Consumer Server/Data Logger.
Parallel processing of many events by many nodes allows for much more time to look at a particular event and therefore for a much more accurate decision whether to keep it or not. Level-3 provides an additional reduction by a factor of 4 bringing the total event rate down to approximatively 75 Hz.
It would be noted that the data acquisition system is taking data for (usually large but never exceeding duration of the store) continuous periods of time called *runs*. During the run, the detector configuration (including all the on-line calibration constants *etc.*) is almost stable, it can change however from one run to another, affecting or not the data being recorded. In any case, the events that pass Level-3 are stamped with run number, so that at a later time, information about detector configuration at the time the event was taken could be retrieved from the database.
The data flow from the Level-3 is segmented into ten streams, which are denoted with letters from A to J. The events which passed all three levels of Two Track Trigger requirements are written out as "Stream H". All the streams are written to tape in real time, as the data are taken, i.e. in on-line regime.
In a second time, data are retrieved from mass storage to be elaborated. At this stage the raw data banks are unpacked and collection of physics objects suitable for analysis, such as tracks, vertices, muons, electrons, jets, are generated. This is similar to what is done at Level-3, except that it is done in a much more elaborate fashion, applying the most up-to-date calibrations and using the best measured beamlines.
Hence the data flow undergoes further categorizations and the ten data streams coming from the Level-3 output are separated in 35 data sets depending on the physics process one is interested in. In this analysis we consider the `hbhd0d` data set, which includes events from the Stream H. In practice it is more convenient to work with the compressed version of this data set called `xbhd0d`. The compression is achieved by means of dropping objects not used in most analysis from the event record. This greatly reduces the storage required (in particular allows disk storage, rather then tape storage) and speed up the analysis, because reading the data is often one of the most time consuming parts.
Occasionally, but not too often, it is found beneficial to re-process part or all the data with a newer and better version of alignment tables and detector calibrations. So one needs to state the *production version* to fully specify the data used in the analysis. We use `xbhd0d` data set produced with 5.3.1 version of *production*.

3.5 Two Track Trigger

As seen in the previous Section, data flow is splitted in several trigger paths, so at the end of the trigger chain different data samples are available for dedicated analyses. The CDF II collaboration developed several trigger paths suited for B physics analysis on fully hadronic decay modes. The so called `B_CHARM` triggers, is a series of trigger paths

	B_CHARM_LOWPT	B_CHARM	B_CHARM_HIGHPT
L 1	$p_T^1 > 2\,GeV/c$ $p_T^2 > 2\,GeV/c$ $\Delta\phi_{1-2} < 90°$	$p_T^1 > 2\,GeV/c$ $p_T^2 > 2\,GeV/c$ $p_T^1 + p_T^2 > 5.5\,GeV/c$ $\Delta\phi_{1-2} < 135°$ opposite charge	$p_T^1 > 2.6\,GeV/c$ $p_T^2 > 2.6\,GeV/c$ $p_T^1 + p_T^2 > 5.5\,GeV/c$ $\Delta\phi_{1-2} < 135°$ opposite charge
L 2	$p_T^1 > 2\,GeV/c$ $p_T^2 > 2\,GeV/c$ $0.012 < d_0^1 < 0.1\,cm$ $0.012 < d_0^2 < 0.1\,cm$ $2° < \Delta\phi_{1-2} < 90°$ $L_{xy} > 0.02\,cm$	$p_T^1 > 2\,GeV/c$ $p_T^2 > 2\,GeV/c$ $p_T^1 + p_T^2 > 5.5\,GeV/c$ $0.012 < d_0^1 < 0.1\,cm$ $0.012 < d_0^2 < 0.1\,cm$ $2° < \Delta\phi_{1-2} < 90°$ $L_{xy} > 0.02\,cm$ opposite charge	$p_T^1 > 2.6\,GeV/c$ $p_T^2 > 2.6\,GeV/c$ $p_T^1 + p_T^2 > 5.5\,GeV/c$ $0.012 < d_0^1 < 0.1\,cm$ $0.012 < d_0^2 < 0.1\,cm$ $2° < \Delta\phi_{1-2} < 90°$ $L_{xy} > 0.02\,cm$ opposite charge
L 3	$p_T^1 > 2\,GeV/c$ $p_T^2 > 2\,GeV/c$ $p_T^1 + p_T^2 > 4.0\,GeV/c$ $0.008 < d_0^1 < 0.1\,cm$ $0.008 < d_0^2 < 0.1\,cm$ $2° < \Delta\phi_{1-2} < 135°$ $L_{xy} > 0.02\,cm$ $\lvert\eta\rvert < 1.2$ & $\lvert\Delta z_0\rvert < 5\ cm$	$p_T^1 > 2\,GeV/c$ $p_T^2 > 2\,GeV/c$ $p_T^1 + p_T^2 > 5.5\,GeV/c$ $0.008 < d_0^1 < 0.1\,cm$ $0.008 < d_0^2 < 0.1\,cm$ $2° < \Delta\phi_{1-2} < 135°$ $L_{xy} > 0.02\,cm$ opposite charge $\lvert\eta\rvert < 1.2$ & $\lvert\Delta z_0\rvert < 5\ cm$	$p_T^1 > 2.6\,GeV/c$ $p_T^2 > 2.6\,GeV/c$ $p_T^1 + p_T^2 > 5.5\,GeV/c$ $0.008 < d_0^1 < 0.1\,cm$ $0.008 < d_0^2 < 0.1\,cm$ $2° < \Delta\phi_{1-2} < 90°$ $L_{xy} > 0.02\,cm$ opposite charge $\lvert\eta\rvert < 1.2$ & $\lvert\Delta z_0\rvert < 5\ cm$

Table 3.1: *Trigger requirements for the* B_CHARM *streams thorough the 3 trigger levels. The selections are performed requiring that a couple of tracks satisfies the presented cuts. The L_{xy} refers to the vertex defined as intersection of the two tracks, while $|\Delta z_0|$ is the distance in z coordinate between the two tracks.*

studied to select B (and D) mesons in multi-bodies decay modes. The basic idea in the design of these triggers was the power of impact parameter tracks in the b-quark identification. Table 3.1 shows the trigger requirements for the trigger paths used for the analysis presented in this Thesis; all these triggers are designed to collect *hadronic mesons*, selecting events were only a couple of tracks satisfy impact parameters requirements, thus the name Two Tracks Trigger (TTT).[4] This idea is easy to understand for the 2-body decay topology, but not so easy for multi-bodies decay modes. Trigger studies [48] were accomplished for multi-bodies decay modes also, showing that this kind of requirement selects multi-bodies b decays among background.
All these B triggers have a signal efficiency around 0.5% for essentially all the interesting signals collected. This can be thought somewhat reductif, but, as discussed in Chapter 1, in $p\bar{p}$ collisions, the $b\bar{b}$ cross-section is very large with respect to the B-factories production,

[4]The number of track over that a trigger requirement can be performed is strongly dependent to the time available to compute the selection. Increasing the number of tracks over which requiring the cuts, comes into an higher combinatorial and then in an higher CPU time needed to perform the decision.

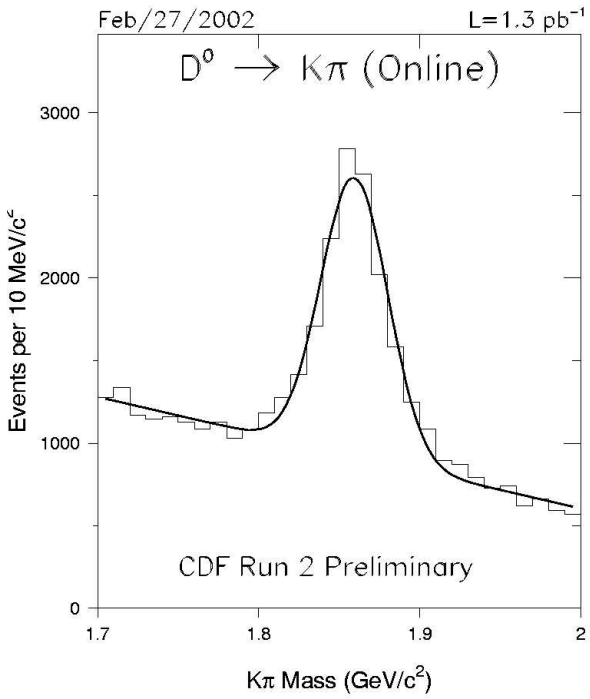

Figure 3.6: *On-line invariant mass of two SVT trigger tracks with kaon and pion masses assignment.*

and low efficiency in the trigger selection can be spent gaining high background rejection and improved signal over background ratio.
The overall CDF II trigger is designed in such a way that output rate have to be always the same, regardless the instantaneous luminosity. That means that for high luminosities ($\sim 100 \times 10^{30}\, cm^2 s^{-1}$), some triggers are not enough selective. Therefore a further reduction is necessary and it is done keeping only some events selected randomly among those that passed the trigger. In this case the trigger is said to be *prescaled*, that is a scale factor is applied to select events to be written. During the data taking, the output rate is kept constant maximizing the number of events to be written, therefore any change in the running condition will reflect in the change of the prescale factor of some triggers. These trigger paths, among them there are the Hadronic triggers also, are said to be *dynamically prescaled*. CDF II reached high luminosity only at the beginning of 2004, so the effective prescale factors used for the B trigger paths, are almost constant with time. Anyway, because the different selection requirements among the triggers, which will change the efficiency, the effective prescale is needed. Table 3.2 shows these effective prescales calculated for the trigger paths used in this analysis.

As already mentioned, the knowledge of the beam position and the detector calibration parameters are important informations in order to correct the track parameters at Level-2 and Level-3 stages and then to perform the trigger selections in a straightforward way. Therefore Trigger rates have to monitored during the data taking. The monitoring of the Two Track Trigger rate is done on-line using D^0 peak on invariant mass distribution.

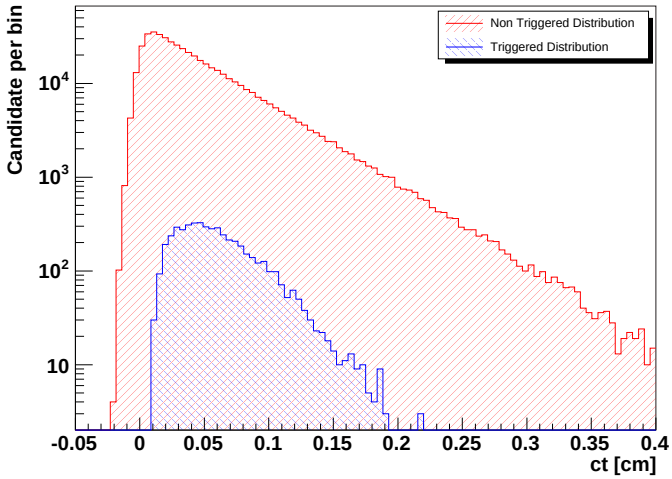

Figure 3.7: *Comparison between the B^+ proper time distribution before (red) and after (blue) the trigger selection. Track impact parameters requirements heavily modifies the ct distribution.*

The D^0 production rate is large, and therefore the peak can be used to monitor the performance of the Two Track hadronic Trigger over the time, since the number of D^0 per pb^{-1} is constant if the trigger works properly. In fact the track informations provided by SVT at Level 2 can be further integrated at Level-3 to extract some kind of *hybrid track*. These kind of tracks is created adding to the SVT tracks the third dimensional information from COT 3D tracking after a match is performed between SVT and COT only tracks. These hybrid 3D tracks provide the possibility to work out the invariant mass of a couple of track (given a mass hypothesis) and look for peaks in invariant mass distribution. This is done for $D^0 \to K\pi$ decay mode. At Level-3 Hybrid tracks are used to create D^0 candidate and after some requirements are applied [42] a peak on invariant mass distribution can be seen *on-line* as shown in Fig. 3.6.

3.5.1 The Trigger Effect

Unfortunately, acting on track impact parameter, strongly modify the expected proper time distribution, no longer following a simple exponential law. More over, the `B_CHARM` streams require two displaced tracks (see Table 3.1), meaning that different topologies will

Trigger	Prescale	$\mathcal{L}$ (pb^{-1})
`B_CHARM_LOWPT`	2.13	170 ± 10
`B_CHARM`	1.13	321 ± 19
`B_CHARM_HIGHPT`	1.11	290 ± 17

Table 3.2: *Effective prescales and integrated luminosities of the TTT trigger paths.*

be affected in different way by the same selection. Finally the trigger selection requires not only a lower limit for the track impact parameters, but also an upper limit[5], reflecting in a upper cut on decay length for a reconstructed meson.
The result of trigger selections is that the usual exponential law followed by the proper time distribution of a given meson is modified both at lower and upper values of proper time. In Figure 3.7 the proper time distribution of a $B^+ \to \bar{D}^0\pi^+$ ($\bar{D}^0 \to K\pi$) is shown after the trigger selection is applied. The exponential law distribution is also plotted for comparison. Thus, there is a trigger bias on lifetime distribution which has to be evaluated. In this analysis we show the method developed to understand this trigger bias on Chapter 5 while in Chapter 6 the results obtained using this technique are discussed.
It has been shown in reference [62] that the upper requirement on track impact parameter reduces the statistical power of the used sample, returning a bigger statistical uncertainty of the fitted variables. The problem consists in the fact that the upper impact parameter requirement operated by the trigger, translates into an upper selection on the proper time distribution. As demonstrated in reference [62], the statistical precision due to the upper lifetime cut is modified by replacing N, the total number of events, with:

$$N \to N \cdot \left(1 - \left\langle \left(\frac{\frac{\Delta t}{2\tau}}{\sinh(\frac{\Delta t}{2\tau})} \right)^2 \right\rangle \right), \tag{3.2}$$

where τ is the lifetime to be measured and Δt is the width of the time window defined by the lifetime selections. So it makes sense to define a *statistical power per event*, $\mathcal{P}$ as:

$$\mathcal{P} = 1 - \left\langle \left(\frac{\frac{\Delta t}{2\tau}}{\sinh(\frac{\Delta t}{2\tau})} \right)^2 \right\rangle. \tag{3.3}$$

As you can see the *statistical power* is a function of $\frac{\Delta t}{2\tau}$ and can have strong effect also with naive selection requirements. For example, an upper limit requirement leaving a time interval that is twice the lifetime measured ($\frac{\Delta t}{2\tau} = 2$), retains 85% of the events, but the statiscal power per event is reduced to 28%. The combined effect is equivalent of loosing 76% of the unbiased sample before the selection, rather than the naively expected 14%.
The Two Track Trigger requirement of two tracks with impact parameters laying between 120 μm an 1 mm, translates to different upper and lower lifetime selections for each event, typically yielding a Δt ranging from 1 to 3 B lifetimes and depends on the decay mode reconstructed.

[5]The upper limit on impact parameter cut is performed, at Level Trigger, to reduce the number of possible SVT roads and therefore to reduce the AM volume.

Chapter 4

Data Sample and Reconstruction

This analysis measures the lifetime of the B^+, B_d^0 and B_s^0 on the following exclusive decay modes:

- $B^+ \to \bar{D}^0\pi^+ \quad (\bar{D}^0 \to K^+\pi^-)$
- $B_d^0 \to D^-\pi^+ \quad (D^- \to K^+\pi^-\pi^-)$
- $B_d^0 \to D^-\pi^+\pi^-\pi^+ \quad (D^- \to K^+\pi^-\pi^-)$
- $B_s^0 \to D_s^-\pi^+ \quad (D_s^- \to \phi\pi^-)\,(\phi \to K^+K^-)$
- $B_s^0 \to D_s^-\pi^+\pi^-\pi^+ \quad (D_s^- \to \phi\pi^-)\,(\phi \to K^+K^-)$

The results are based on the data collected by CDF II detector within the Two Track Trigger from February 2002 to August 2004 (runs range: 138809 to 186598). Events triggered by at least one of the trigger paths among the `B_CHARM, B_CHARM_HIGHPT` and `B_CHARM_LOWPT` described in Section 3.5, are used, which correspond to an integrated luminosity of $362 \pm 21\ pb^{-1}$.

4.1 Reconstruction

CDF II has a limited particle identification capability and therefore the reconstruction is done using a track-based method: tracks are assigned pion or kaon mass hypotheses and combined together to form meson candidates. Only tracks combination falling in certain mass window are considered as coming from a possible candidate and are further subjected to additional selections.
Since in an event with N_{tracks} the number of possible candidates for a n-bodies decay is $N_{cand} = \frac{N_{tracks}!}{(N_{tracks}-n)n!}$ it is clear that for high n, N_{cand} can be very large and spurious combinations become the largest source of background. The number of combinations can be greatly reduced by applying quality selections to tracks. As a consequence, tracks selection has a very important role in reducing the combinatorial background, and tracks quality requirements must be applied before any reconstruction algorithm is applied. In

Variable	Selection
Number of COT Axial SL	≥ 2
Number of COT Stereo SL	≥ 2
Number of COT Axial hits per SL	≥ 5
Number of COT Stereo hits per SL	≥ 5
Number of Axial SVX hits	≥ 3
$\lvert\eta\rvert$	≤ 2
Pt	$> 0.30\ GeV/c$

Table 4.1: *Common track selection.*

particular for the lifetime measurement, tracks quality is essential to achieve the best vertex resolution. In the default track fit, performed at *production* level, hits are included without taking into account multiple scattering that occurs to particles traveling through the detector. The tracks are then refitted by the analysis code correcting the parameters for this effect [49]. The refit procedure is also necessary to correctly take into account the energy loss which depends on mass hypothesis; at this level the alignment table informations are specified for the track refitter. The detector material description is introduced at this level in a more accurate way. The refit procedure is performed using the Kalman [50] technique.
The common tracks quality requirement are reported in table 4.1. Most of them refer to the minimum number of hits required for a good track fit, while a selection is performed on η to select tracks within the fiducial volume of the main tracker (COT), and a minimum p_T is needed in order to reject tracks with high curvature.

The reconstruction of all decay modes proceed trough a similar way: following the decay products, the B meson is reconstructed via the intermediate charmed resonances, as sketched in Fig. 4.1.
The procedure starts which a D meson identification by vertexing two (D^0), or three ($D^{\pm}\, D_s^{\pm}$) tracks, with the only constraints to originate from a common vertex and a charge track match ($D^0 \rightarrow K^{\pm}\pi^{\mp}$, $D^{\pm} \rightarrow K^{\mp}\pi^{\pm}\pi^{\mp}$, $D_s^{\pm} \rightarrow \phi\pi^{\pm}$). To suppress the combinatorial background the invariant mass of D candidates is required to lie within the regions $[1.7; 2.0]$, $[1.87; 1.91]$ and $[1.87; 2.07]$ GeV/c^2 for D^0, $D^{\pm}$ and $D_s^{\pm}$ mesons respectively. No particle identification is applied, therefore kaon and pion mass hypotheses are used to create D candidates. In addition, for the $D_s^{\pm}$ mesons, a further constraint is used on the invariant mass distribution of the two kaons: because this is supposed to peak at the ϕ meson mass, we asked a ϕ mass window within $[1.011; 1,028]$ GeV/c^2. Then requirements on χ^2 probability of the D vertex fit are performed to remove spurious candidates.
The D mesons are therefore combined (new vertex fit) with a third track[1], using the pion mass hypothesis, to reconstruct the final B meson candidate. At this level a second vertex fit is performed between the attached track(s) and the D meson candidate. Here the mass value of charmed particles is constrained to PDG value [41]. After this procedure

[1]For the $D\pi\pi\pi$ modes three tracks were added.

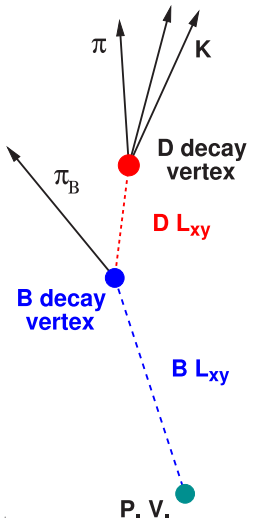

Figure 4.1: *Sketch of a* $B^0_d \to D^-\pi^+$ *decay topology*

is completed a collection of B meson candidate has been done. Anyway the background contamination is still high, and more accurate selections have to be performed to reveal the signal peak in the invariant mass distribution. This kind of selections are performed acting on quantities that characterize the B meson and depend on the reconstruction channel. The next section will describe the procedure to optimize these selections.

4.2 Selections Optimization

The selection requirements have been optimized to maximize the significance of the B meson signal while preserving a high signal efficiency. The significance of the signal is defined as $\frac{S}{\sqrt{S+B}}$ where S and B are the number of signal and background events in the signal region. The number of signal and background events can be determined directly from data. This procedure is correct only in the case of large samples. To avoid the risk of tuning on fluctuations the selection optimization uses a combination of data and Monte Carlo simulated events. A sample of data containing non signal events is used to estimate the number of background events after a selection criteria is applied. Usually the low and high B invariant mass regions in the proximity of the peak are chosen to guarantee a background sample that is kinematically similar to the signal. The Monte Carlo sample is used to estimate the number of signal events after the same selections.
Since the hadronic decays of B mesons considered in this analysis have complex structures due to reflections and partially reconstructed events, sampling events from the low mass window close to the B meson peak is not possible. Therefore the background is fitted to an exponential plus a first order polynomial in the region away from the peak and reflections (Fig. 4.2). The integral of the background distribution under the signal region measures the number of background events. The scaling factor between Monte Carlo and data for signal is determined before the selection optimization is done. The optimization process is iterative, it starts with a set of loose requirements. At each step all requirements

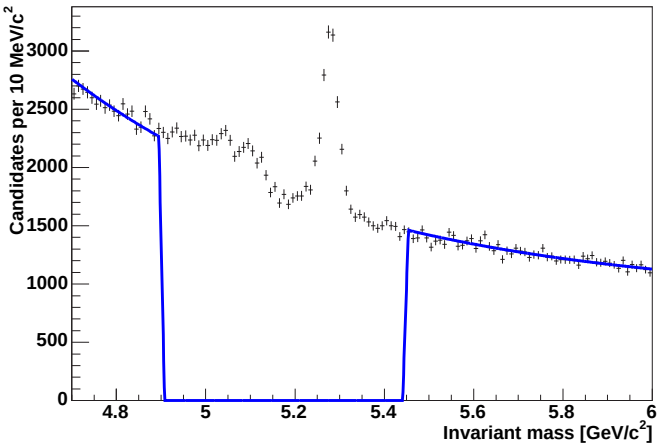

Figure 4.2: *The B_d^0 invariant mass distribution before selection optimization. The fit of the background is done using an exponential function plus a first order polynomial and excluding the signal area.*

are fixed except one that is varied. At each variation the significance and the efficiency are registered. For a given set of selections with the same significance the one with the highest efficiency is chosen. A minimum efficiency of 90% is required. The final set of requirements for the five decays is listed in Table 4.2. Here, the χ^2_{xy} variables refer to the goodness of the vertex fit, the $p_T^{\pi_B}$ is the transverse momentum of the pion(s) coming from the B vertex, and ΔR is defined as $\Delta R = \sqrt{(\Delta\eta)^2 + (\Delta\phi)^2}$. The trigger requirements, on the trigger quantities, is applied to the B candidate tracks of all the decay modes. The requirements follow the trigger path prescription, that is, when an event pass the `B_CHARM_LOWPT` selections, the same requirements are applied to the B candidate, while when an event pass the `B_CHARM_HIGHPT` trigger the B candidate tracks are subjected to these more restrictive selections. With the trigger reconfirmation on candidate tracks we are guaranteed that are the B tracks that fired the trigger, making more clear the sample composition and reliable the signal simulations. Finally it was required that the z position of the B vertex doesn't lie within the crack regions of silicon detectors.

4.3 Monte Carlo Simulation

Monte Carlo simulations are an essential tool for almost every High Energy Physics analysis. They represent a fast and tuned interface between the predicted model and the collected data, helping researchers to have a better understanding of the data.
A Monte Carlo Simulation can be summarized in a three step procedure: particle generation, particle decay and detector response simulation. The particle generation is based on Bgenerator [56], a Monte Carlo program based on NLO calculations [57]. In fact Bgenerator, dedicated to B physics, is able to generate B or D mesons only, without care of fragmentation products that naturally come from hadron collisions.

Optimized selections for the reconstructed decay modes					
Meson Decay Mode	$B^{\pm}$ $\bar{D}^0\pi^{\pm}$	B^0_d $D^-\pi^+$	B^0_s $D^-_s\,\pi^+$	B^0_d $D^-\,\pi^+\pi^-\pi^+$	B^0_s $D^-_s\,\pi^+\pi^-\pi^+$
$\chi^2_{xy}(B)$	< 15	< 15	< 15	< 15	< 13
$\chi^2_{xy}(D)$	< 15	< 15	< 14	< 15	< 10
$L^B_{xy}\,(\mu m)$	> 350	> 500	> 250	> 750	> 600
$L^{B-D}_{xy}\,(\mu m)$	$>$ -150	$>$ -300	$>$ -200	$>$ -200	$>$ -100
$p^{\pi_B}_T\,(GeV/c)$	> 1.0	> 1.2	> 1.2	> 0.4	> 1.0
$\lvert d^B_0\rvert\,(\mu m)$	< 80	< 110	< 60	< 65	< 55
$\Delta R(D-\pi_B)$	< 2.0	< 1.5			
$p^B_T\,(GeV/c)$				8.0	9.0
$M(3\pi)\,(GeV/c^2$				2.2	2.2
	Trigger reconfirmation on SVT quantities B's z vertex within [-50.0;-18.0] $\cup$ [-14.0;14.5] $\cup$ [18.5;50.0] cm				

Table 4.2: *List of optimized selections for the B mesons reconstruction. Trigger selections and Z quality of B vertex were re-applied to B candidate tracks.*

A b quark[2] is generated following the NDE input spectrum [57] and then is fragmented into a B meson according to the Peterson fragmentation function [57] with the Peterson fragmentation parameter at the default value of $\epsilon_B = 0.006$. For our analysis the generated quark was limited within the spatial region $\mid \eta \mid < 1.3$ and with a minimum momentum greater then $5\,GeV/c$. These settings reflect the fact that the b quarks can be generated within the fiducial volume of the detector and that a minimum energy is needed in order to fire the trigger.
The mesons decay relies on EvtGen program [77], a decayer tool extensively tuned by B factory experiments.
Then the geometry and the behavior of active volumes of the CDF II detector are simulated using a dedicated software based on the third version of GEANT package [78]. GEANT is a wide spread program able to simulate the response of High Energy Physics detectors at hit level.
Finally, the trigger effects are simulated by TRGSim++, a software that implements the details of the trigger logic used by CDF II. TRGSim++ appends to each simulated event trigger banks and trigger bits as for data. A particular trigger path can be selected by requiring the corresponding trigger bit.
Since the CDF II detector underwent several hardware and trigger modifications during the data taking period, the actual dataset can be rather inhomogeneous. To properly reflect the different running conditions that occurred, the Monte Carlo samples have been generated for a set of representative runs weighted by their luminosity.

[2]For our simulation only a single quark was generated.

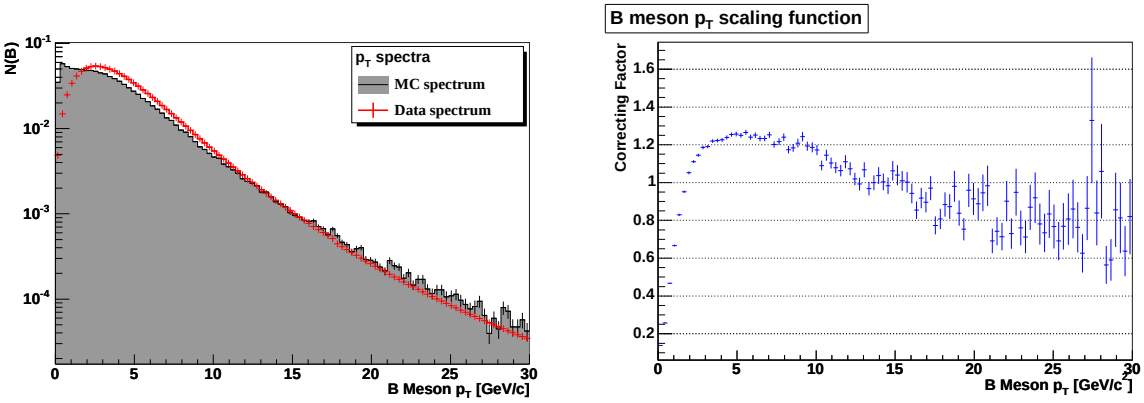

(a) (b)

Figure 4.3: *(a) Data and Monte Carlo p_T spectra used in the re-reweighing technique. Data spectrum comes from $B \to J/\psi X$ inclusive analysis. Both distributions are normalized to have unitary area.(b) Re-weighting factor as function of p_T used in this analysis.*

4.3.1 Monte Carlo Validation

The most significant way to evaluate how well the Monte Carlo reproduces data is to compare the simulated distributions with those obtained after sideband subtraction in data. However, because of the complex resonance structures in the low mass region (See Fig. 4.2) only the high-mass sideband can be used for subtraction. The background fraction in the signal region (defined to be ± 2 standard deviation around the mass peak) is estimated with a mass fit as described in Chapter 6. Figs. 4.4 and 4.5 show a comparison between Monte Carlo and data for some variables in the case of the $B_d^0 \to D^-\pi^+$ meson. The agreement is usually good, but not perfect, mainly because only the high-mass sideband was used. Indeed other analyses show that the agreement is rather good. As shown in Fig. 4.3(a), the momentum spectrum of the Monte Carlo generated B mesons shows a discrepancy compared to data. To correct for this effect, that would introduce a bias in the lifetime measurement, the Monte Carlo is re-weighted according to the B meson p_T spectrum measured by the CDF collaboration. For the B_d and the B_u mesons, p_T spectra have been measured in data using high statistics sample with improved purity, while for B_s, does not exist any statistically significant measurement. Therefore, to take into account for a different p_T spectrum we re-derived the efficiency distribution after the p_T spectrum has been re-scaled with a B-inclusive spectrum from CDF data. The p_T spectrum comes from the CDF analysis [68] where B mesons are selected via inclusive decay modes $B \to J/\psi X$, $J/\psi \to \mu^+\mu^-$. In this analysis J/ψ have been reconstructed identifying an invariant mass peak in the $\mu^+\mu^-$ distribution, therefore, prompt J/ψ and b-Hadron contributions have been separated looking for a secondary vertex which the J/ψ belongs.
The Monte Carlo transverse momentum spectrum is therefore re-weighted using the following technique. Data and Monte Carlo distributions have been normalized to have

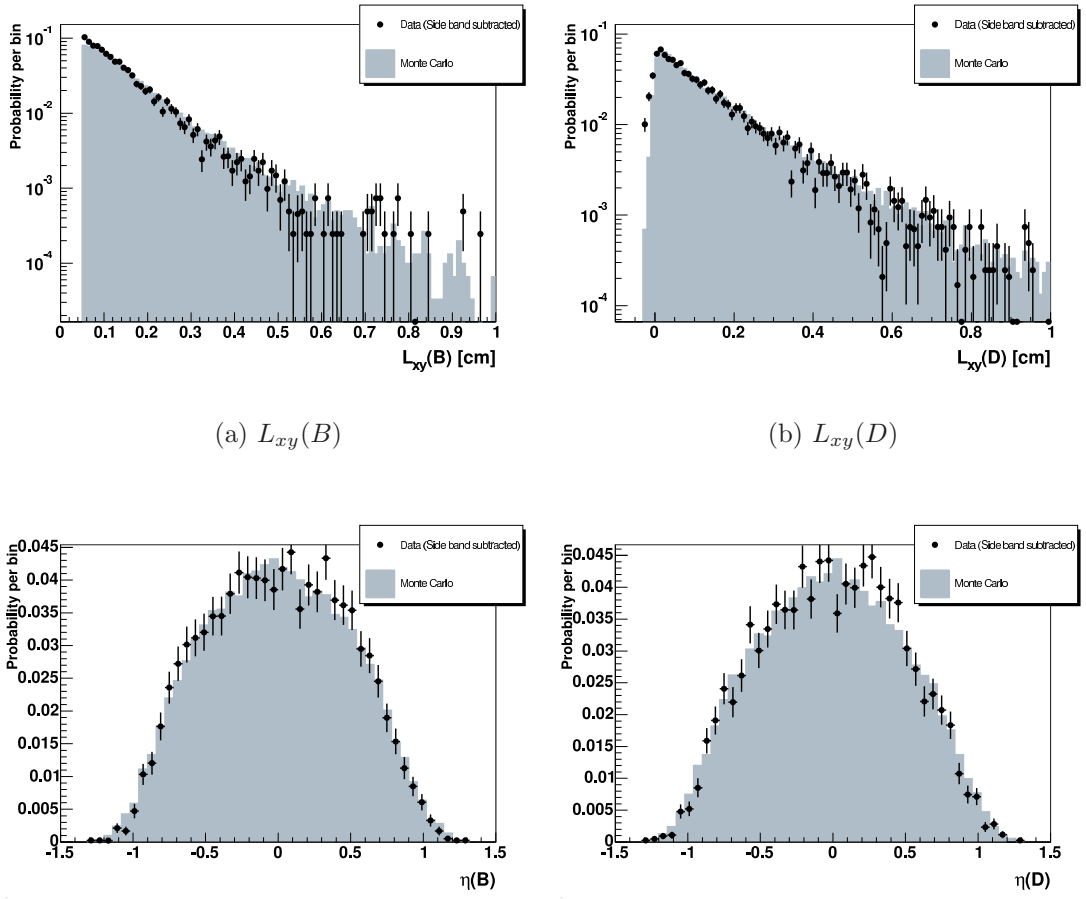

(a) $L_{xy}(B)$ (b) $L_{xy}(D)$

(c) $\eta(B)$ (d) $\eta(D)$

Figure 4.4: *Data and Monte Carlo comparison for B_d^0 meson $L_{xy}(B)$ (a), $L_{xy}(D)$ (b), $\eta(B)$ (c), $\eta(D)$ (d). All distributions are normalized to unity.*

unitary area. Therefore for each p_T bin (every 300 MeV/c) the ratio between the entries of the two distribution has been calculated as correcting factor, therefore the re-weighted p_T value is defined as:

$$p_T^{rew.} = p_T \frac{N_{Data}(p_T)}{N_{MC}(p_T)}, \tag{4.1}$$

where p_T is the value to be re-weighted, and $N_{Data}(p_T)$ $N_{MC}(p_T)$ are the entries for the momentum p_T in the red and gray histograms of Fig. 4.3(a), respectively. In Fig. 4.3(b) the behavior of scaling factor $\frac{N_{Data}(p_T)}{N_{MC}(p_T)}$ as a function of p_T is shown. The uncertainty in the scaling factors as been taken into account as systematic error in Chapter 7.

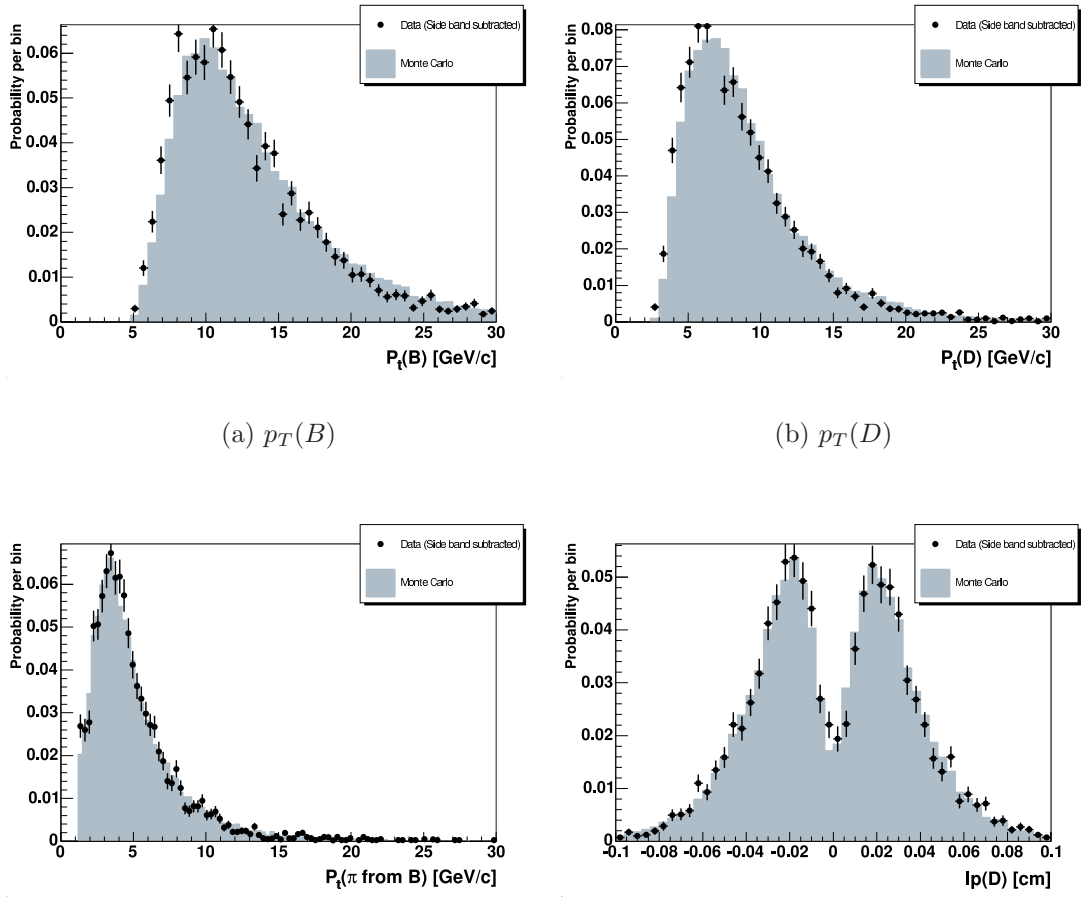

(a) $p_T(B)$ (b) $p_T(D)$

(c) $p_T^{\pi_B}$ (d) $d_0(D)$

Figure 4.5: *Data and Monte Carlo comparison for B_d^0 meson $p_T(B)$ (a), $p_T(D)$ (b), $p_T^{\pi_B}$ (c), $d_0(D)$ (d). All distributions are normalized to unity.*

Chapter 5

Methodology

The effects of trigger selections on proper decay time have to be correctly incorporated in the probability density functions used to build up the likelihood adopted to extract the lifetime.
This analysis developed a Monte Carlo based method that makes full use of the detailed simulation of the CDF II detector and trigger systems. In the case of the Two Track Trigger this is somehow an obliged step to perform, due to the presence of unavoidable correlations between the two SVT tracks and the offline tracks, and also due to the necessity to correctly describe the effect of the SVT patterns acceptance.

5.1 The Basic Idea

In absence of any kind of trigger bias and resolution effects, the decay time distribution of an unstable particle follows an exponential distribution:

$$f(ct) = \frac{1}{c\tau} e^{-\frac{ct}{\tau}}. \tag{5.1}$$

Detector resolution introduces a smearing of the time measurement in such a way that the actual decay time distribution is described by the Fourier convolution:

$$f(ct) = \frac{1}{c\tau} e^{-\frac{ct'}{\tau}} \otimes R(ct; ct') \tag{5.2}$$

where $R(ct; ct')$ is an appropriate resolution function, t is the reconstructed proper time (the measured quantity), while t' is the true proper time (not known). The Two-Track Trigger requirements on the tracks impact parameters, on the track-pair opening angle and transverse decay length modify the proper decay time distribution (see Fig. 3.7), so that its effective shape is no longer described by Eq. 5.2.

The method presented, described in detail in the following sections, consists basically in parameterizing the trigger and selection effects into a single acceptance (efficiency), thought as a function of the reconstructed (measured) lifetime only ($\epsilon_{TTT}(ct)$).

The introduction of the efficiency function modify the unbiased Probability Density Function as:

$$f(ct) = \frac{1}{c\tau} e^{-\frac{ct'}{\tau}} \otimes R(ct; ct') \cdot \epsilon_{TTT}(ct). \tag{5.3}$$

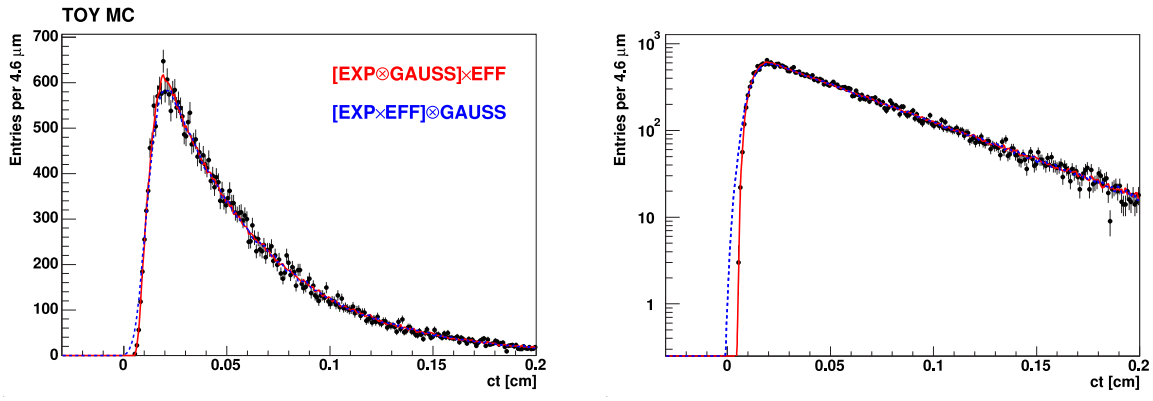

(a) (b)

Figure 5.1: *(a) Toy Monte Carlo lifetime distribution where only a L_{xy} requirement is applied. The p.d.f. projections in the case of an efficiency function based on the reconstructed ct (solid line) and on the true ct (dashed line) are over imposed. In the last case the curve does not correctly describe the distribution. (b) The same plot in logarithmic scale.*

The efficiency method can be trivially generalized to include any other inevitable bias effect, due to analysis selections used to reduce background level. Moreover, this method is well matched to be implemented in fast algorithms to optimize the computation time and precision, which are crucial for the mixing analysis (see for example [63]).
In the rest of the analysis we will refer to the efficiency curve as the overall efficiency function, where analysis and trigger effects are considered together.

In the proposed method the efficiency function is derived using Monte Carlo samples of the signal events, by comparing the measured proper time distributions obtained before and after the trigger and selection requirements. A drawback of this approach is that the method relies on the correctness of the simulation of the trigger effects, and, more important, of the resolutions models used in the simulation of the CDF detector. It will shown that the current level of detail of the CDF simulation is indeed adequate for the scope, giving at the same time an evaluation of the associated systematic uncertainties. It is worth to notice here that the efficiency function has to be defined in terms of measured quantities, and not in terms of true quantities. The use of an efficiency function depending on the *true quantities*, could be done only in the case of simple relations between the measured and *true* proper decay time values, or after a complete treatment of the correlations effects between them (i.e. performing a full unfolding procedure). Fig. 5.1 shows a simple Toy Monte Carlo lifetime distribution where only the requirement that $L_{xy} > 200$ μm is applied. The Probability Density Function projections ($p.d.f.$) in the case of an efficiency function based on the reconstructed ct and on true ct are over imposed. In the last case the $p.d.f.$ clearly fails to correctly describe the lifetime distribution. Therefore using an efficiency function based on the true ct would lead to an incorrect extraction of

the lifetime.

5.1.1 Measurement of the ct efficiency function ($\epsilon_{TTT}(ct)$)

Several methods can been implemented to describe the overall Two Track Trigger efficiency based on Monte Carlo, the basic idea we used is simply to define the efficiency function as a ratio of the signal proper time distributions before and after the trigger selections:

$$\epsilon(ct) = \frac{Histo^{TTT}(ct)}{BEFORE - TTT(ct)}. \tag{5.4}$$

The efficiency function is then defined as bin by bin ratio of two histograms provided by the simulations. The histogram at the numerator, Histo^{TTT}(ct), collects those events that pass the trigger and the analysis requirements, while the histogram at the denominator, BEFORE-TTT(ct), contains all the events after reconstruction but before any selection. However this definition does not represent correctly the efficiency because the resolutions distributions before and after the selections are different. The trigger selects a specific region of the kinematics phase space and in general requires better track reconstruction. To correct for that problem the definition has been changed as follow:

$$\epsilon(ct) = \frac{Histo^{TTT}(ct)}{\sum_i exp(ct, c\tau^{MC}) \otimes Gauss(\sigma^i_{ct})}, \tag{5.5}$$

where, the denominator is replaced by an histogram defined as the sum over the number of events passing the trigger selections of the lifetime distribution, (with the same lifetime used in the Monte Carlo simulation) convoluted with the resolution function for that Monte Carlo event. The model for the resolution function is assumed to be a Gaussian with mean equal to zero and width equal to the σ_{ct} of each Monte Carlo event. Aside, this method does not require an additional sample of non triggered events.
In this way, the efficiency distribution is not suitable as $p.d.f.$ component in an unbinned likelihood fit. Therefore the efficiency distribution has to be fitted with some functional form. The functional form for $\epsilon(ct)$ is essentially arbitrary since there is no model for the description of the trigger and analysis bias. However it is desirable to keep the number of free parameters as low as possible. Moreover, this function should have no zeros and be positively defined in order to avoid subsequent negative $p.d.f.$, therefore a sum of exponential multiplied by second order polynomial was chosen:

$$\epsilon_{TTT}(ct) = \sum_{i=0}^{i=3} N_i \cdot (x - \beta_i)^2 \cdot e^{\frac{-x}{\tau_i}} \cdot (x > \beta_i) \tag{5.6}$$

The second order polynomials describe the initial rise, whether the exponentials take care of the decreasing behavior at high ct values. The main feature of this kind of parametrization is the possibility to work out analytically the primitive of the overall signal $p.d.f.$ This is important when you need to have a faster and more accurate fitter. The problem that arises with this parametrization is its versatility: the exponential function might not suit different efficiency shapes due to different selection requirements.

A more versatile parameterization, though slower because not analytically integrable, is a polynomial ratio:

$$\epsilon_{TTT}(ct) = \frac{(a_0 \cdot ct + a \cdot ct^2 + a_1 \cdot ct^3)^2}{(a_2 + a_3 \cdot ct + a_4 \cdot ct^2 + a_5 \cdot ct^3 + a_6 \cdot ct^4)^2} \tag{5.7}$$

Here, the numerator describes the initial rise, whether the denominator takes care of the decreasing behavior at high ct values. As mentioned above, this parametrization, though more versatile, provides a signal $p.d.f.$ that is not analytically integrable, and can present poles or zeroes in the fitting region, so that we have to be careful using it. Because that, in our analysis we decided to use the parametrization in Eq.: 5.6.
Thus, a binned Likelihood fit was performed on the efficiency distributions. Figures 5.3, show the efficiency distributions of B_d^0, B^+ and B_s^0 for the five decay channels studied in this analysis, with the fit curves superimposed. These curves are the fit results obtained using the functional form in Eq. 5.6, and the selection requirements used in this analysis (described in Chapter 4).
The relative contributions from the different trigger paths are taken into account. These contribution were obtained summing the various contributions weighted with the effective luminosity associated to each curve.
In fact, different trigger selections can modify the proper time distributions in different ways. If one consider the selections performed by the `B_CHARM` trigger paths it's clear the problem arising from the lack of the opposite charge requirement on the `B_CHARM_LOWPT`. For a three bodies decay mode, such as the $B^- \to D^0\pi(D^0 \to K\pi)$, excluding the opposite charge requirement allows new trigger topologies modifying in that way the overall shape of the proper time distribution. To be more specific, one can distinguish two different topologies within the $D{+}track(s)$ decay modes: the first, when the track coming from the B (π^B) is a trigger track; the second when the trigger tracks are both D tracks. Because the charge requirement between the two trigger tracks, the relative ratio between the two contribution can change. This behavior is well explained in Figs. 5.2, where using Toy Monte Carlo, the efficiency curves are shown for different trigger topologies and decay modes, with and without the opposite charge selection is applied. As you can see, for the 3 tracks modes the relative ratio between the two contributions (when π^B fires the trigger and when not) change significantly in the presence of the opposite charge requirement, while in the 4 tracks modes the difference is negligible. The effective prescales of each trigger, and the associated integrated luminosity used in the distributions and fits in Figs. 5.3, are reported in Table 3.2.
Then the efficiency distributions from the 3 trigger paths used, were summed weighting them with the associated luminosities, and the overall distribution was fitted. All the fits show good χ^2 fit probabilities that range from 80% to 99% for the B_d^0, B^+ and B_s^0 cases, and reproduce sufficiently well the behavior of the histogram efficiency.

5.2 The fit Procedure

As mentioned above, the lifetime estimations will be extracted via an unbinned likelihood fit. In the analysis, this statistical procedure will be widely used to estimate the

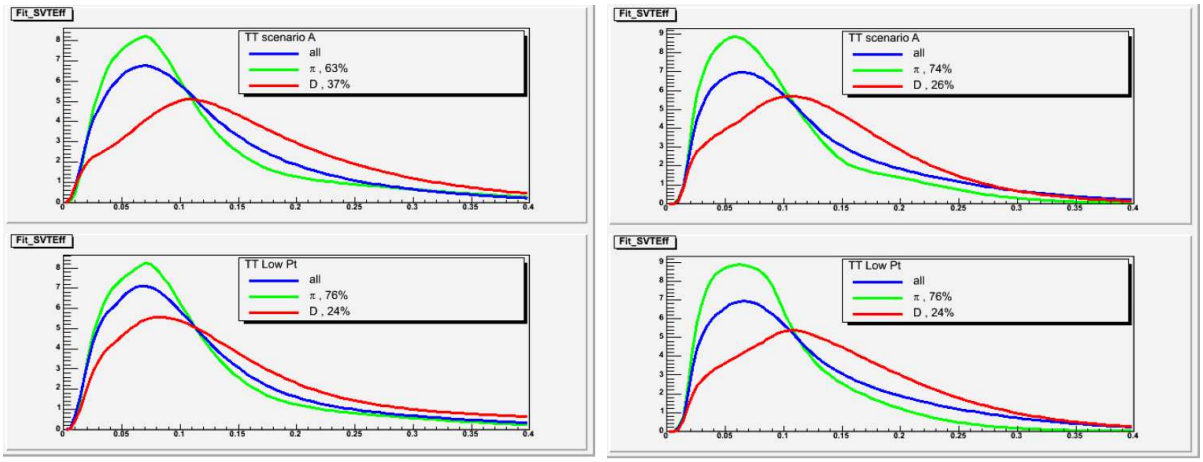

(a) 3 tracks decay mode

(b) 4 tracks decay mode

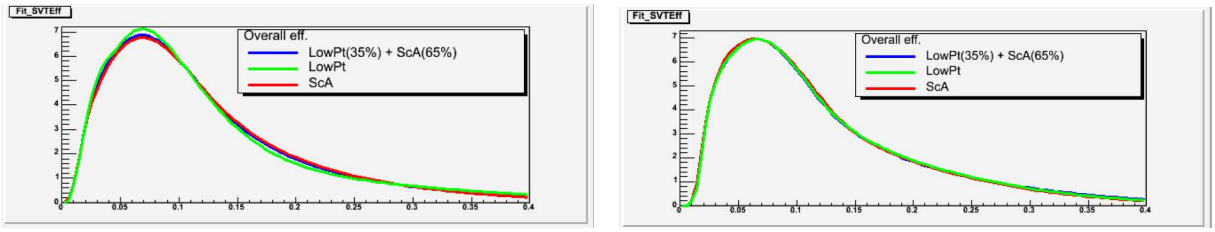

(c)

(d)

Figure 5.2: *The opposite charge requirement effect on the efficiency curves. On the left column the behavior of a 3 tracks decay mode, on the right the same plots for a 4 tracks decay mode. In Figs (a) and (b) are shown the different efficiency curves when the* π^B *fire the trigger (green) and when not (red). Also an overall efficiency curve is plotted as a sum of the weighted curves (blue). On the top of these plots the* `B_CHARM` *are shown, while on the bottom the same configuration when* `B_CHARM_LOWPT` *trigger selections are applied. Plots (c) and (d) summarize the overall efficiency curves comparing the different trigger scenarios.*

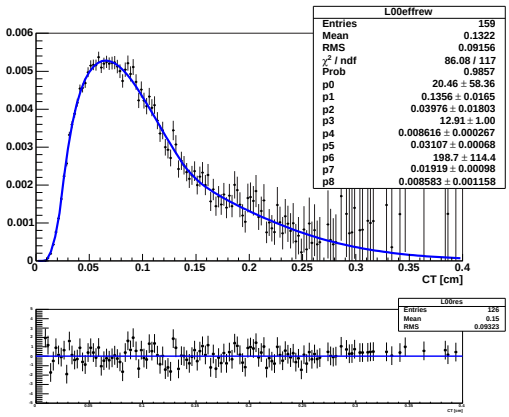

(a)

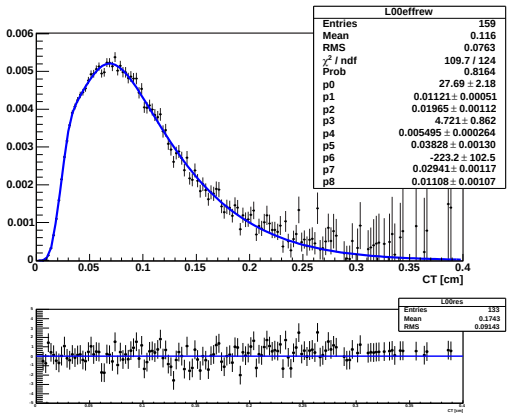

(b)

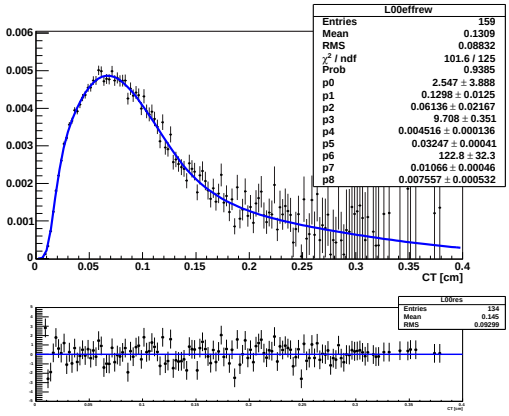

(c)

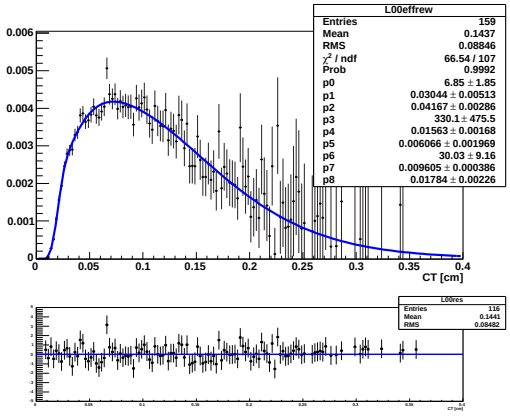

(d)

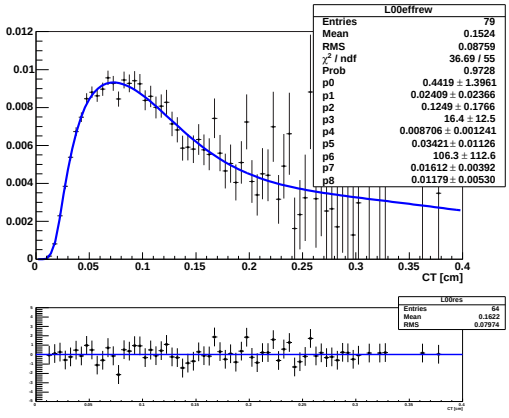

(e)

Figure 5.3: *The SVT efficiency curves (defined in Eq. 5.6) and distributions for the decay modes (a) $B^0_d \to D^-\pi^+$, (b) $B^+ \to \bar{D}^0\pi^+$, (c) $B^0_s \to D^-_s\pi^+$, (d) $B^0_d \to D^-\pi^+\pi^-\pi^+$, (e) $B^0_s \to D^-_s\pi^+\pi^-\pi^+$ from Monte Carlo. On the bottom of each plot is shown the pull distribution of residuals, defined as the difference between the data histogram and the fitting curve divided by the histogram bin error.*

fit components also, therefore few comments are needed to explain how it works. The unbinned likelihood fit technique is a statistical method to estimate a set of given parameters concerning a given distribution [81]. The better estimation is obtained for the set of parameters α, that maximizes the Likelihood Function $\mathcal{LF}$, defined as

$$\mathcal{LF}(\alpha) = \prod_{i=1}^{N} \mathcal{L}(x_i; \alpha); \tag{5.8}$$

where N is the statistical size of the fitted sample, and $\mathcal{L}(x_i; \alpha)$ is the *p.d.f.* assumed to describe the fitted distribution. In general, fit routines are created to find minima of functions, more over is often convenient to deal with sums and not with products. Therefore, usually the set of parameters α is estimated minimizing the following function called (Negative Log-Likelihood Function):

$$\mathcal{NLLF}(\alpha) = -\ln \mathcal{LF}(\alpha) = -\sum_{i=1}^{N} \mathcal{L}(x_i; \alpha). \tag{5.9}$$

This is one of the most powerful method to find minima, because is make use of the all information available from the distribution, and it is independent of the binning also. More over, because it does not rely on the binning, the normalization parameter can be excluded from the list of parameters to be minimized. Some times, one deals with distributions of *independent variables* which describe different aspects of the same phenomenon. Hence we have to minimize the parameters describing the *p.d.f.* of the different variables *simultaneously*. In this case, the global *p.d.f.* $\mathcal{L}(x, y; \alpha, \beta)$, in the case of two variables, is written as product of the single *p.d.f.*, :

$$\mathcal{L}(x, y; \alpha) = \mathcal{L}(x; \alpha) \cdot \mathcal{L}(y; \beta), \tag{5.10}$$

where x and y are the independent variables and α and β are the set of parameters describing the template distributions. In the realistic case in which the *p.d.f.* of the two variables are written as a sum of different contributions (signal, backgrounds,...) weighted by M relative contributions f_j, the global *p.d.f.* is written:

$$\begin{aligned} \mathcal{L}(x, y; \alpha, \beta) &= \sum_{j=1}^{M-1} f_j \cdot \mathcal{L}_j(x; \alpha) \cdot \mathcal{L}_j(y; \beta) \\ &+ \left(1 - \sum_{j=1}^{M-1} f_j\right) \cdot \mathcal{L}_M(x; \alpha) \cdot \mathcal{L}_M(y; \beta), \end{aligned} \tag{5.11}$$

where the last term is written just to highlight the correlation between the relative contributions, which sum must be equal to 1.
This fit procedure that make use of the *p.d.f.* described in Eq. 5.11 is often called *combined fit*. The advantage of this procedure is the possibility to determine with great precision the relative fractions f_j between the different contributions in data sample using all the information available. The determination of the parameters α, β and f_j is obtained minimizing the expression in Eq. 5.9 where $\mathcal{L}(x_i, \alpha)$ is substituted with the expression in

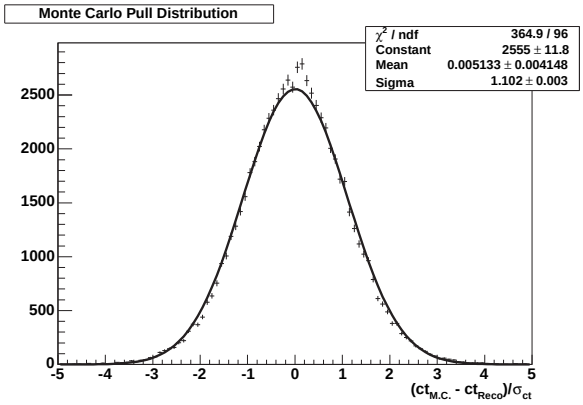

Figure 5.4: *Proper Time Pull Distribution from signal Monte Carlo ($B^{\pm} \to \bar{D}^0\pi^{\pm}$).*

Eq. 5.11.
For the distributions where the information is available only in a *binned form*, such as the efficiency distributions that come binned for construction, a likelihood fit is available in a binned form:

$$\mathcal{NLLF}(\alpha) = -\ln \mathcal{LF}(\alpha) = -\sum_{i=1}^{N_{bins}} N_i \cdot \mathcal{L}(x_i;\alpha) - N_{bins}, \tag{5.12}$$

where N_{bins} stands for the number of bins used, N_i stands for the number of entries in such a bin and $\mathcal{L}(x_i)$ is the value of the $p.d.f.$ evaluated at the bin center x_i.
Even if the binned likelihood uses less information w.r.t. the unbinned method, it is anyway more powerful then a simple χ^2 fit, that rely on the hypothesis of a Gaussian distribution of the measurements, therefore we preferred to use it when unbinned fits were not possible.
In this analysis, the minimization procedure has been preformed using a dedicated package, MINUIT [82], within the `root` software framework [83].

5.3 Test on Monte Carlo

The Method proposed in the previous section rely on a good tuning of Monte Carlo samples used to extract the efficiency curves. In Chapter 4 we provided a comparison between data and Monte Carlo which evidence the not perfect agreement among the two, because of reliability to describe the contaminations of physical background under the signal peak and then subtract them. Indeed, is important to test the availability of the Method; this Section is devoted on checks done on the Method and on the fitters using Monte Carlo samples and Toy Monte Carlo.
The obtained efficiency curves are tested for consistency on statistically independent samples of signal Monte Carlo events, that is the signal Monte Carlo samples were fitted for the lifetime using efficiency curves extracted from statistically independent Monte Carlo samples. The selection requirements used, are the same described in Chapter 4, so that

the efficiency curves are the same that we used to fit the data.
Therefore, an unbinned Maximum Likelihood fit with event by event *ct* error has been performed with a *scale factor* fixed to 1.1. The *ct* error per event information is derived from the vertices and momentum resolutions. Therefore, for each reconstructed B meson, an estimation of the uncertainty can be associated to the evaluation of its decay proper time. What we get is an estimation of the *real* error that affect the *ct* measurement, then to correct for any bias introduced in such as estimation, a fixed factor is multiplied to the *ct* error is used. In practice, the scale factor is a quantity that estimate how well the detector resolutions are measured. The scale factor has been determined, from the simulations it selves, looking at the pull distribution obtained as $\frac{ct_{reco}-ct_{HEPG}}{\sigma_{ct_{reco}}}$, where ct_{reco} is the reconstructed proper time , $\sigma_{ct_{reco}}$ is the corresponding uncertainty, and ct_{HEPG} is the *true proper time* obtained from the generator level quantities in Monte Carlo samples (see Fig. 5.4). The width of the pull distribution is taken as a scale factor.
The results of the fits are listed in Table 5.1 and the fit projections for the studied decay modes, are shown in Figs. 5.3. All the fit results agree within one standard deviation with the generated value. The samples used are populated enough to give statistical errors smaller then what we obtained on data.

Variable	$B^{\pm} \to D\pi$	$B^0_d \to D\pi$	$B^0_s \to D_s\pi$	Unit
Gen. Value	501	460	438	μm
Scale Factor	1.1	1.1	1.1	
Fitted Value	499.9 ± 2.2	462.3 ± 2.7	437.9 ± 2.5	μm
Sample Size	110K	57K	54K	# of events
$\chi^2/n.d.f.$	53/56	55/58	54/59	
$Prob(\chi^2)$	59 %	59 %	66%	
Variable	$B^{\pm} \to J/\psi K^{\pm}$	$B^0_d \to D3\pi$	$B^0_s \to D_s3\pi$	Unit
Gen. Value	501	438	460	μm
Scale Factor	1.1	1.1	1.1	
Fitted Value	502.3 ± 2.5	464.2 ± 4.3	436.5 ± 4.4	μm
Sample Size	91K	18K	13K	# of events
$\chi^2/n.d.f.$	73/57	96/91	57/49	
$Prob(\chi^2)$	7%	33 %	20%	

Table 5.1: *Results of signal Monte Carlo fits.*

5.3.1 Toy Monte Carlo

Goodness of the fit tests are used as a tool to determine the reliability of the fitter itself and its implementation.
Usually, Toy Monte Carlo techniques are performed to check if the $p.d.f.$ are correctly normalized and if sources of bias are hidden within the fit method. As mentioned above, different efficiency parameterizations lead to different normalization procedures, *e.g.* Eq. 5.6 is analytically integrable, while Eq. 5.7 requires a numerical integration.

Toy Monte Carlo tests are performed to check the full fitter behavior. First the fitter in the case of signal only is tested. The test does not depend on the decay mode but on

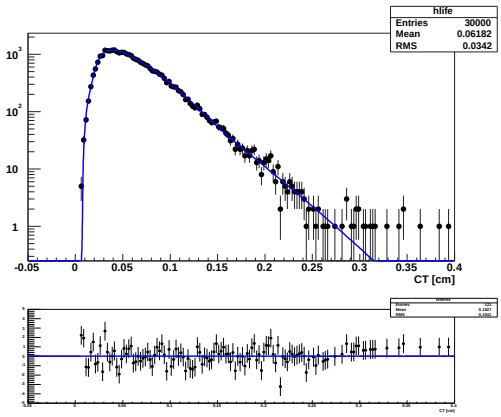

(a)

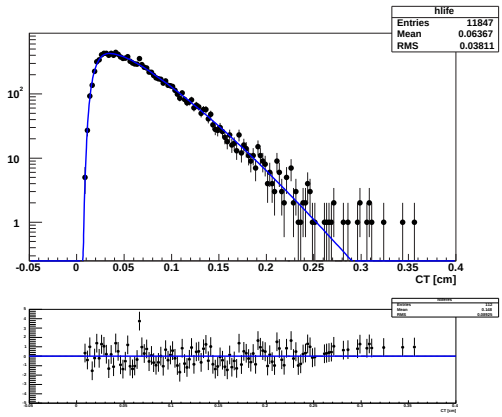

(b)

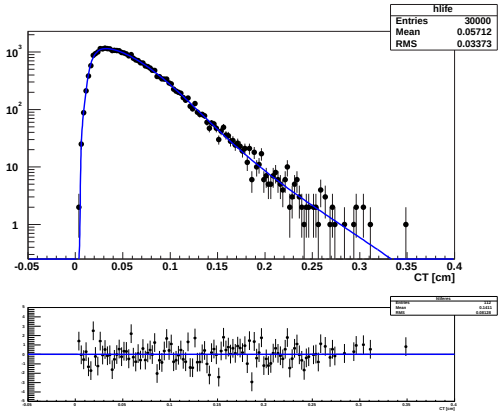

(c)

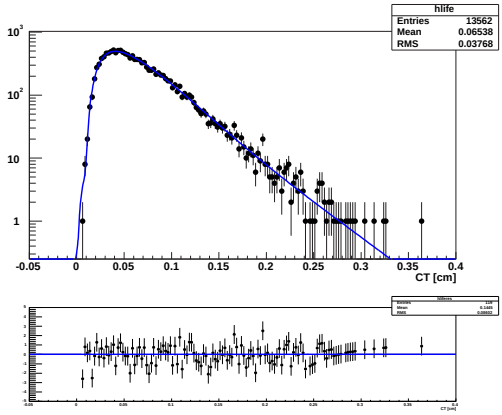

(d)

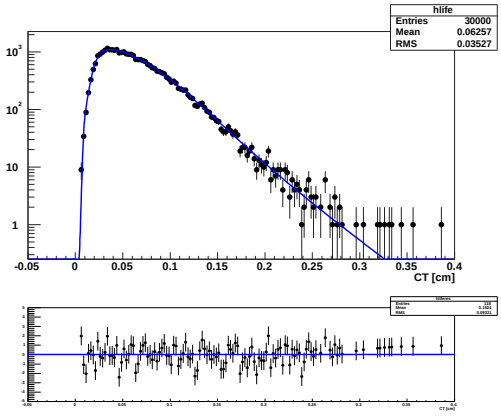

(e)

Figure 5.5: *Fit results for* $B_d^0 \to D^-\pi^+$ *(a),* $B_d^0 \to D^-\pi^+\pi^-\pi^+$ *(b),* $B_s^0 \to D_s^-\pi^+$ *(c),* $B_s^0 \to D_s^+\pi^+\pi^-\pi^+$ *(d),* $B^+ \to D^0\pi^+$ *(e). On the bottom you can see the pull distribution defined as the difference between the data histogram and the fitting curve divided by the histogram bin error. On top left on each plot is shown the Likelihood value as function of* τ *parameter.*

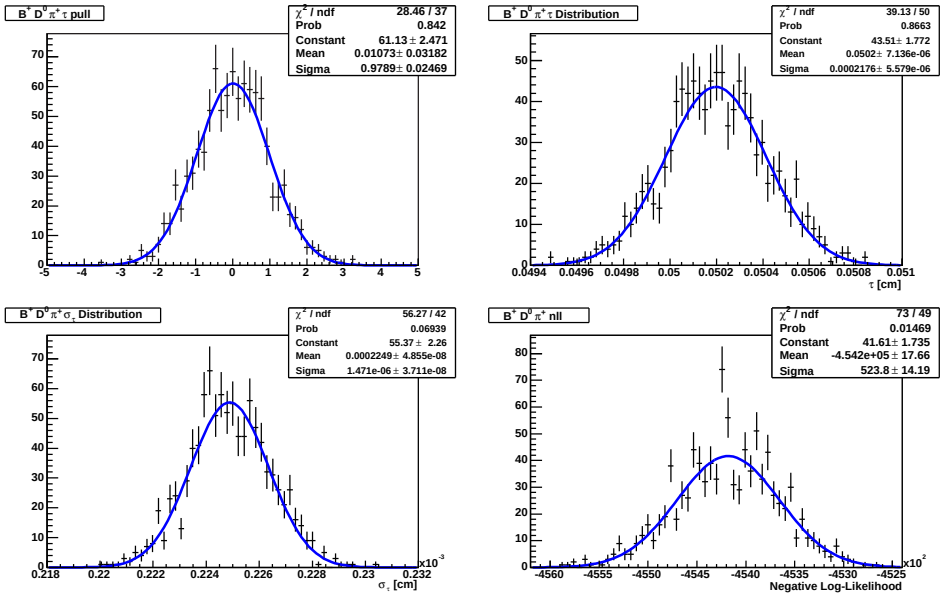

Figure 5.6: *Results for the signal only toy Monte Carlo for the $B^{\pm}$ meson. On top-left the $c\tau$ pull distribution, on top-right $c\tau$ distribution, while on the bottom τ_{err} and NLL distributions are shown.*

the *p.d.f.* implementation within the fitter, so the test was done for the $B^{\pm}$ only: a set of 1250 experiments with 51513 events each, has been generated for the $B^{\pm}$ mode. The input signal lifetime is set to $c\tau = 502\ \mu m$ and we used the $B^{\pm}$ efficiency function as described above. The results of the toy experiments are shown in Figure 5.6. No deviations appear from the plotted distributions.

In order to test the complete fitter tool we generated a set of B^0_d, $B^{\pm}$ and B^0_s samples in all the decay modes used, including background contributions. These contributions were templated using the functional forms described in Chapter 6. We generated 1000 toy experiments for each decay mode studied with the same statistical size found on data samples. The results of the toy experiments are shown in Figure 5.7 for all the B decay modes further analyzed. Table 5.2 shows the fit results on pull distributions. In all cases the pulls behave correctly without significantly deviations, being compatible with normalized Gaussian distributions with mean 0 and sigma 1. In Figure 5.7 last column, a blue line shows the Negative Log-Likelihood value as obtained from the fits on data. All of them are compatible with the distributions on toy experiments.

5.4 Check on an Unbiased Sample

A way to test our capability to fit lifetime distributions in hadronic decays selected with the SVT trigger, is to use a sample of data where no bias is present and where a fully reconstructed decay mode can be collected. Fortunately, this kind of sample exists: the $B^{\pm} \to J/\psi K^{\pm}$ decays collected with the dimuon trigger.
The $B^{\pm}$ lifetime is measured on these events and subsequently in a sub sample where

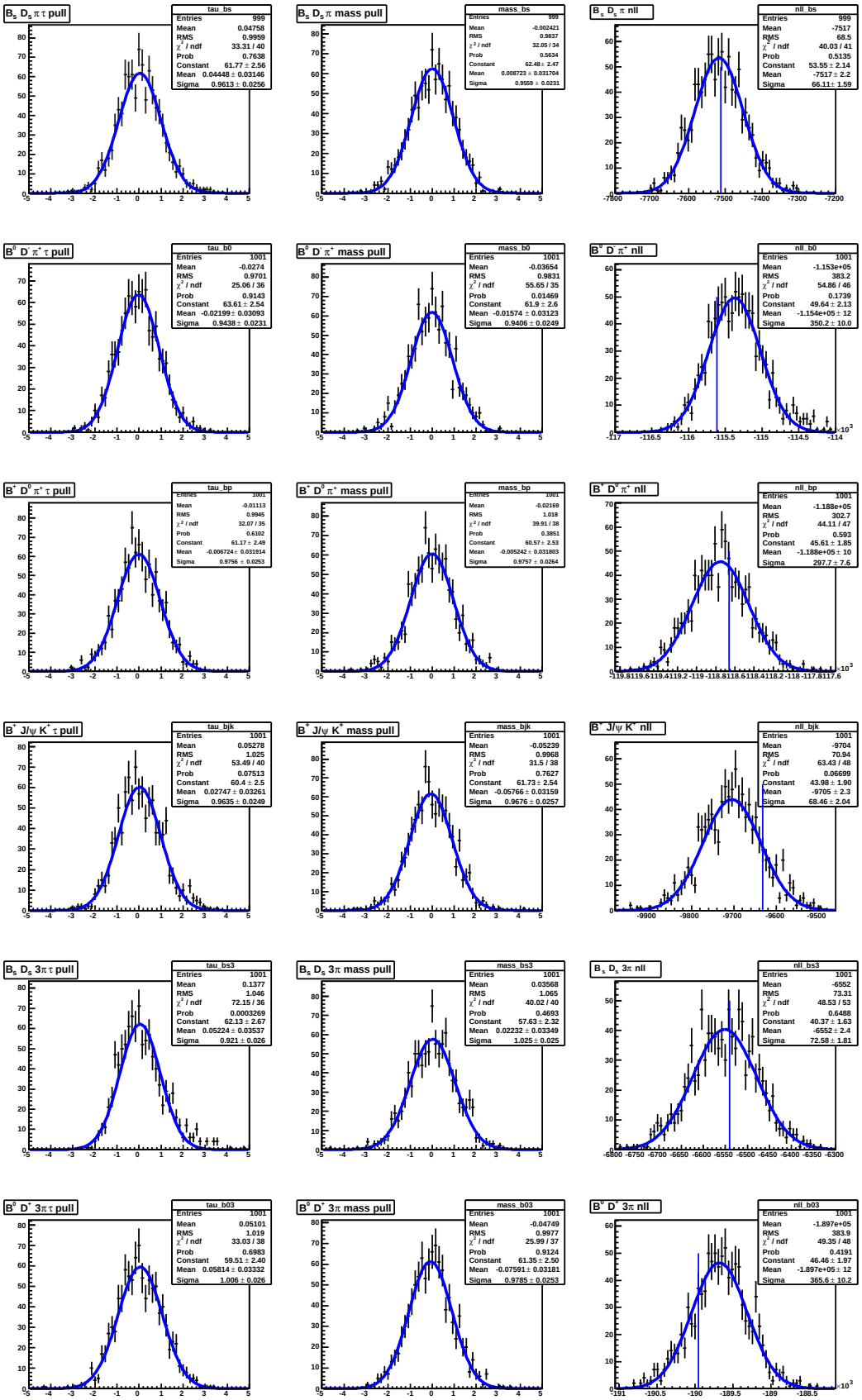

Figure 5.7: *Results from Toy Monte Carlo for all B decay modes.*

Variable		$B^{\pm} \to D^0\pi^{\pm}$	$B_d^0 \to D^-\pi^+$	$B_s^0 \to D_s^-\pi^+$	Unit
Sample Size		17147	16640	999	# of events
τ	mean	-0.007 ± 0.032	-0.022 ± 0.031	0.044 ± 0.031	
τ	σ	0.976 ± 0.025	0.944 ± 0.023	0.961 ± 0.026	
mass	mean	-0.005 ± 0.032	-0.016 ± 0.031	0.009 ± 0.032	
mass	σ	0.976 ± 0.026	0.941 ± 0.025	0.956 ± 0.023	
Variable		$B_d^0 \to D^-\pi^+\pi^-\pi^+$	$B_s^0 \to D_s^-\pi^+\pi^-\pi^+$	$B^{\pm} \to J\psi K^{\pm}$	Unit
Sample Size		32284	1235	10K	# of events
τ	mean	0.058 ± 0.033	0.052 ± 0.035	0.028 ± 0.033	
τ	σ	1.001 ± 0.026	0.921 ± 0.026	0.963 ± 0.025	
mass	mean	-0.076 ± 0.032	0.022 ± 0.033	-0.058 ± 0.032	
mass	σ	0.978 ± 0.025	1.025 ± 0.025	0.968 ± 0.026	

Table 5.2: *Fit results on pull distributions. Plots are shown in Fig. 5.7.*

Two Track Trigger selections are applied using the trigger quantities. Hence the lifetime measurements before and after the Two Track Trigger selections are compared to have a reliable estimation of the method used. The strength of this kind of estimation resides on the statistical power of sample used. Unfortunately, even if the sample before the trigger selection is populated enough to reach a resolution of the 2%, the SVT requierement is too much severe, and the statistical power goes down of a factor of 4. Therefore this comparison cannot give an ultimate answer on the method reliability, anyway it can give strong indications of possible troubles.

5.4.1 $B^{\pm} \to J/\psi K^{\pm}$ lifetime fit

The data used for this check are collected with the dimuon trigger in the `xpmm0d` dataset, requiring the presence of a couple of separated muons. This trigger is intended to collect huge sample of J/ψ mesons to dimuons decay mode. The data correspond to an integrated luminosity of about 260 pb^{-1}.
The event selections are taken from previous analyses dedicated on B lifetime measurements on this dataset [72]. The B reconstruction follows the decay topology: J/ψ mesons are first identified looking at invariant mass distribution of two muons. A third track is then added to J/ψ candidate in the Kaon mass hypothesis, and the $B^{\pm}$ meson is finally identified via resonant peak in the invariant mass spectrum of $\mu\,\mu\,K$ tracks. The B decay vertex is reconstructed as a physical point where the candidate tracks converge. The signal enhancement on the background is obtained requiring muon identification, good track reconstruction and B vertex determination. The list of requirements is reported in Table 5.3. After the described selections, a combined mass-lifetime unbinned maximum likelihood fit was performed on dimuon sample using the following $p.d.f.$:

$$\mathcal{L}(m, \sigma_m, ct, \sigma_{ct}) = f_S \mathcal{L}_S(m, \sigma_m, ct, \sigma_{ct}) + (1 - f_S)\mathcal{L}_{BG}(m, \sigma_m, ct, \sigma_{ct}) \tag{5.13}$$

Description	Cut Value
Track Quality	$p_T > 0.4\ GeV/c$
Track Quality	≥ 3 SVX II layers with an$r-\phi$ hit
Track Quality	≥ 2 axial SL with ≥ 5 hits in each
Track Quality	≥ 2 stereo SL with ≥ 5 hits in each
Muon Quality	≥ 3 axial SL with ≥ 5 hits in each
Muon Quality(CMU only)	$\chi^2_{CMU}(\mu^{\pm}) < 9.0$
Muon Quality	$p_T(\mu^{\pm}) > 1.5\ GeV/c$
J/ψ mass window	$\|m(\mu^+\mu^-) - M^{J/psi}_{PDG}\| < 80\ MeV/c^2$
B Quality	$p^B_T > 5.5\ GeV/c$
B Quality	$p^K_T > 1.6\ GeV/c$
B Quality	$Prob(\chi^2) > 10^{-3}$
Z of B vertex	[-50.0;-18.0]$\cup$ [-14.0;14.5]$\cup$ [18.5;50.0] cm

Table 5.3: *Analysis requirements applied on $B^{\pm} \to J/\psi K^{\pm}$ sample. The χ^2_{CMY} quantity is related to the match between the COT tracks and the CMU stubs, while the prob(χ^2) is related to the vertex quality fit. B candidates are excluded if the Z of secondary vertex lies in regions where the silicon bulk-heads create non instrumented areas.*

where

$$\begin{aligned}
\mathcal{L}_{SIG}(m,\sigma_m,ct,\sigma_{ct}) &= \mathcal{G}(m,\sigma_m)\mathcal{L}_{SIG}(ct,\sigma_{ct}); \qquad (5.14)\\
\mathcal{G}(m,\sigma_m) &= \frac{1}{\sqrt{2\pi}\sigma_m} e^{-\frac{(m-mass_B)^2}{2\sigma_m^2}};\\
\mathcal{L}_{SIG}(ct,\sigma_{ct}) &= \frac{1}{\tau} e^{-\frac{ct}{\tau}} \otimes \frac{1}{\sqrt{2\pi}\cdot S_{ct}\sigma_{ct}} e^{-\frac{(ct)^2}{2(S_{ct}\sigma_{ct})^2}}.\\
\mathcal{L}_{BG}(m,\sigma_m,ct,\sigma_{ct}) &= \mathcal{T}_{BG}(m)\mathcal{L}_{BG}(ct,\sigma_{ct}); \qquad (5.15)\\
\mathcal{T}_{BG}(m) &= a\cdot m + b;\\
\mathcal{L}_{BG}(ct,\sigma_{ct}) &= \sum_{i=1}^{3} \frac{fr_i}{\tau_i} e^{(-1)^i \frac{ct}{\tau_i}} \otimes \frac{1}{\sqrt{2\pi}\cdot S_{ct}\sigma_{ct}} e^{-\frac{(ct)^2}{2(S_{ct}\sigma_{ct})^2}} +\\
&+ (1-fr_1-fr_2-fr_3)\frac{1}{\sqrt{2\pi}\cdot S_{ct}\sigma_{ct}} e^{-\frac{1}{2}\frac{(ct)^2}{2(S_{ct}\sigma_{ct})^2}}.
\end{aligned}$$

The mass sector is parametrized with a Single Gaussian for the signal peak $\mathcal{G}(m,\sigma_m)$ and just a straight line for the background $\mathcal{T}_{BG}(m)$. The description of the proper time sector is instead more complicated: while a single exponential, $\mathcal{L}_{SIG}(ct,\sigma_{ct})$, is needed to describe the signal contribution, a more sophisticated functional form $\mathcal{L}_{BG}(ct,\sigma_{ct})$, is used for the background. The parametrization of the latter is done with two positive exponentials for the long lived background, a negative exponential to take into account the negative tails, and finally a single Gaussian to describe the prompt contribution. The Gaussian used for the prompt description is taken as resolution model, so that all the exponentials used are convolved with this Gaussian. A scale factor S_{ct} was used on the

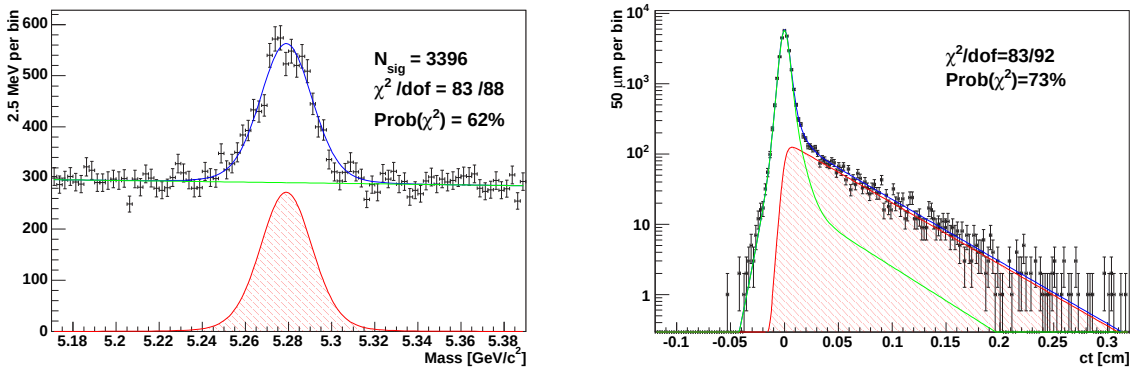

(a) (b)

Figure 5.8: *a) The Mass distribution with the fitted curves superimposed. b) Lifetime distribution with the fitted curves superimposed.*

lifetime sector, and it was floating in the fit to properly take into account the proper time detector resolution.
Background parametrization of the proper time sector $\mathcal{L}_{BG}(ct, \sigma_{ct})$, comes from side bands distributions studies, anyway all the parameters were let free in the fit. The goodness of fit is estimated as projection χ^2 probabilities:

Mass Sector $\chi^2/d.o.f. = 83/88$; $Prob(\chi^2)$ =62%,

Lifetime Sector $\chi^2/d.o.f. = 83/92$; $Prob(\chi^2)$ =73%.

The fit results are shown in Figure 5.8 and summarized in the first column of Table 5.4. In Table 5.4 the second column also reports, for comparison, the results for the same fit as obtained in [72] and the two are in agreement.

5.4.2 SVT-biased $B^{\pm} \to J\psi K^{\pm}$ lifetime fit

In order to study the effect of Two Track Trigger, we selected, from the dimuon sample, events which pass `B_CHARM` requirements using trigger level information, in this way we obtain a sub-sample of $B^{\pm}$ mesons after Two Track Trigger selections.
The Trigger requirements are very tight, so that the signal over noise ratio increases reducing the background contribution to few events under the signal peak, as shown in the Figure 5.10 (a). While the Mass distribution does not change, the proper time distribution indeed suits a deep modification. The signal proper time distribution is now described introducing the overall trigger efficiency discussed in Section 5 and a new template has been used to describe the shape of proper time background distribution. Moreover, the background contribution is reduced and the mass window has to be enlarged to $[5.0, 5.6]$ GeV/c^2 in order to have a sufficient number of background events to model the combinatorial background template.

Par.	Our Fit	Fit as in [72]	Units
M	5278.93 ± 0.26	5278.67 ± 0.26	MeV/c^2
f_S	0.1171 ± 0.0023	0.1223 ± 0.0025	
A	-0.85 ± 0.45	-0.85 ± 0.45	$(GeV/c^2)^{-1}$
S_M	1.556 ± 0.028	1.544 ± 0.028	
$c\tau$	495.1 ± 9.7	498.1 ± 9.9	μm
fr_2	0.0341 ± 0.0062	0.0373 ± 0.0071	
fr_1	0.0099 ± 0.0078	0.1057 ± 0.0087	
fr_3	0.0183 ± 0.0022	0.0135 ± 0.0025	
$c\tau_2$	55 ± 5	52 ± 5	μm
$c\tau_1$	61 ± 5	57 ± 5	μm
$c\tau_3$	450 ± 41	397 ± 59	μm
S_{ct}	1.313 ± 0.011	1.249 ± 0.012	
N_{sig}	3396 ± 67	3385.6 ±68.2	

Table 5.4: *Results of our fit on dimuon sample. The Mass Scale Factor S_M and the proper time scale factor S_{ct} are floating during the fit.*

The background distribution is heavily modified by the trigger requirements, and the following functional form has been chosen to parametrize it:

$$\begin{aligned} \mathcal{L}_{BG}^{TTT}(ct) &= Exp(ct;\tau) \otimes Gauss(\mu;\sigma) \\ &= \frac{1}{\tau} e^{-\frac{t}{\tau}} \otimes \frac{1}{\sqrt{2\pi}\sigma} e^{-\frac{(t-\mu)^2}{2\sigma^2}}. \end{aligned} \tag{5.16}$$

A binned fit was performed on ct-distribution of events from mass side-bands region ([5.0 - 5.227] GeV/c^2 + [5.331 - 5.6] GeV/c^2) to test the background shape. Figure 5.9 shows the side bands ct distribution, while Table 5.5 shows the fit results.

Therefore, to extract the lifetime, a combined mass and lifetime unbinned maximum

Par.	Value	Units
smearing mean	178 ± 18	μm
smearing width	85 ± 14	μm
$c\tau_1$	379 ± 34	μm

Table 5.5: *Fit results on side bands proper time distribution*

likelihood fit has been performed on the sub sample selected with the Two Track Trigger requirements. For the mass sector, the same parametrization used in the non SVT biased case, is used; for the ct distribution, instead, the $p.d.f$ in Eq. 5.3 for signal, and the arbitrary shape parametrization in Eq. 5.16 for the background, is used. The ct efficiency curve has been determined as described in the previous sections.

Since the trigger selection eliminates the prompt contribution, the ct scale factor was not left floating but fixed to the same value obtained in the non SVT-biased fit. It can be

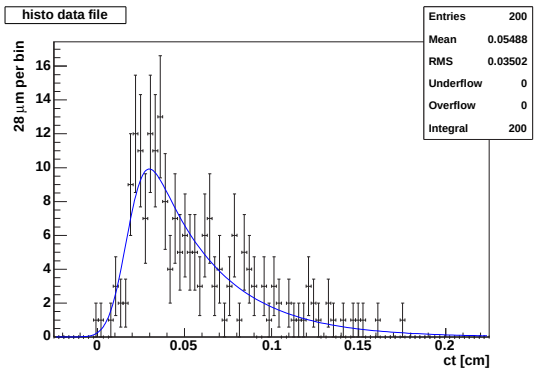

Figure 5.9: *ct side bands distribution with fit result superimposed.*

objected that the resolution distribution can change after the trigger selections, anyway because the B mesons lifetime is large with respect to the resolution achieved at CDF II a possible systematic coming from that is expected to be negligible, as in fact it will be shown in the further chapters. The parameters describing the background proper time distribution are let floating in the fit. However, the fitted values agree with those coming from the side band test, confirming the validity of the parametrization.
The final fit was performed in the mass region from 5.0 to 5.6 GeV/c^2. Results are shown in Table 5.6 and are compared with the results obtained without the SVT trigger selection. The corresponding plots are shown in figure 5.10. The results before and after the trigger selections are compatible within the errors, giving confidence on this method.[1]
Here it can be noticed the statical power reduction due to Trigger and mentioned at the end of Chapter 3. From the lifetime measurement of the not triggered sample, the statistical lifetime resolution is of 1.96% for 3396 signal events. In absence of any trigger bias, one expect that the resolution scales with the square root of the statistic sample, that is for the sample after Two Track Trigger was applied one expects a resolution of $1.96 \cdot \sqrt{3396/433} = 5.49\%$. Instead, the measured lifetime resolution is 7.76%, that is $\sqrt{2}$ times bigger than what expected, compatible with a statistical power reduction of a factor 2.

As mentioned above, the low statistic of this sample limits the importance of this validation. Nonetheless other information can be obtained from this sample. Since the background component under the signal region is very low, the ct efficiency function obtained with sideband subtracted data can be compared to simulated data. This has been done in Figure 5.11, where the two distributions are compared. The signal region is defined in the mass range [5.219 - 5.339] GeV. A χ^2 test, used to quantify the agreement between the two distributions, gives $\chi^2/\text{ndf} = 35.8/37$ and a 52% probability.

[1]To be precise the comparison between the two results cannot be done looking at the quoted errors because the two samples are strongly correlated by construction.

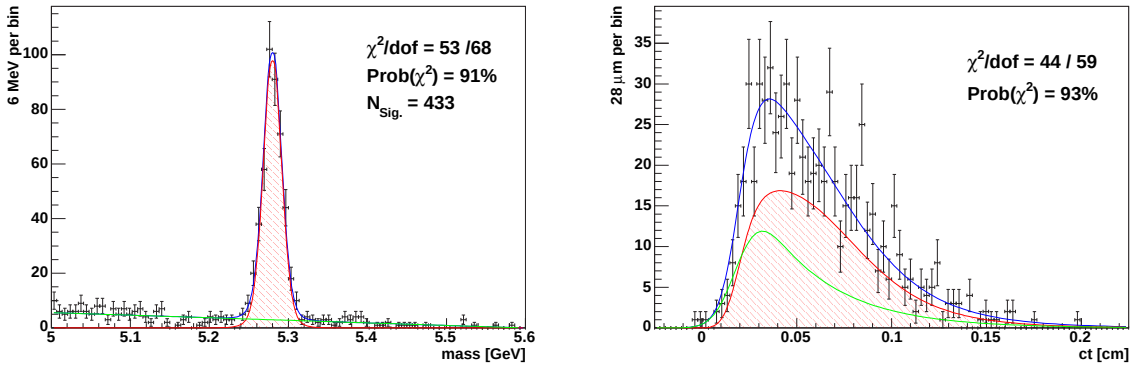

(a) (b)

Figure 5.10: *Fit results after the* B_CHARM *Trigger selection was applied. a) The Mass distribution with the fitted curves superimposed. b) Lifetime distribution with the fitted curves superimposed.*

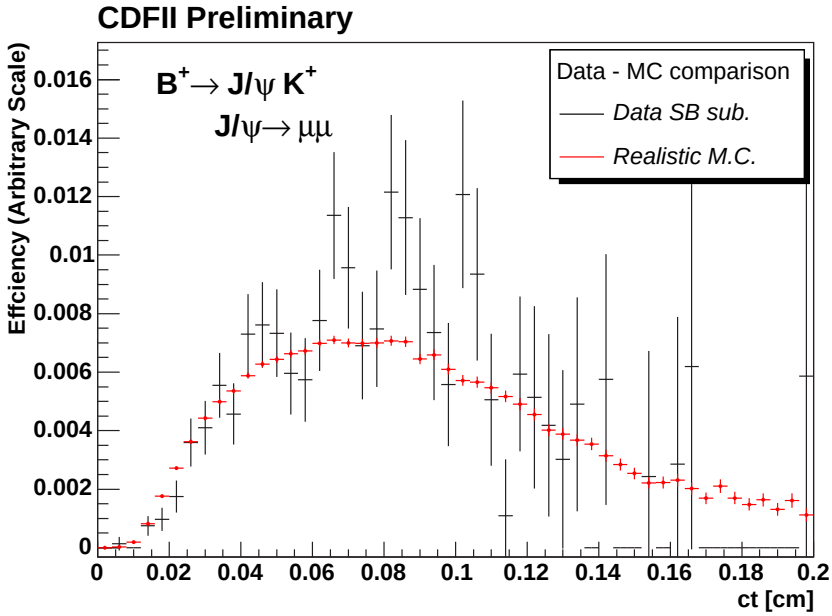

Figure 5.11: *Comparison between the efficiency function obtained from sideband subtracted Data and MC after Trigger and analysis selections. A χ^2 test gives $\chi^2/ndf = 35.8/37$ and a 52% probability.*

Par.	triggered Sample	NON triggered Sample	Units
M	5279.80 ± 0.63	5278.93 ± 0.26	MeV/c^2
f_S	0.639 ± 0.021	0.1171 ± 0.0023	
A	-5.64 ± 0.19	-0.85 ± 0.45	$(GeV/c^2)^{-1}$
S_M	1.445 ± 0.065	1.556 ± 0.028	
$c\tau$	523.4 ± 40.6	495.1 ± 9.7	μm
S_{ct}	1.313 FIXED	1.313 ± 0.011	
NON TTT background parameters			
fr_2	not present	0.0341 ± 0.0062	
fr_1	not present	0.0099 ± 0.0078	
fr_3	not present	0.0183 ± 0.0022	
$c\tau_2$	not present	55 ± 5	μm
$c\tau_1$	not present	61 ± 5	μm
$c\tau_3$	not present	450 ± 41	μm
TTT background parameters			
smearing mean	190 ± 19	not present	μm
smearing width	97 ± 15	not present	μm
$c\tau_1$	363 ± 32	not present	μm
N_{sig}	433 ± 14	3396 ± 67	

Table 5.6: *Results of the fit on triggered sample. In the second column the results from NON triggered sample are reported for comparison.*

Chapter 6

Measurement of the B^+, B_d^0 and B_s^0 lifetimes

In the previous Chapter the method based on Monte Carlo simulation to determine the bias on proper time distribution introduced by the trigger selections has been presented, and results on a sample of $B^\pm \to J/\psi K^\pm$ have been discussed also. This Chapter is devoted to results on hadronically decay modes of $B^\pm$, B_d^0 and B_s^0 mesons. For each decay mode, the fit details will be presented together with the results obtained.

The B meson lifetimes are extracted by performing an unbinned maximum log-likelihood fit with proper time error computed event by event, where mass and lifetime are fitted simultaneously.
This procedure requires to properly model the signal and background contributions in both the invariant mass and proper decay time (ct) sectors.
Hadronic signals collected within the impact parameter trigger, present a complex structure in the mass region close to the signal resonance (see Fig. 4.2). Therefore an effort have been done to understand which are the dominant contributions of the background an how these contributions can be described. As will be shown in this Chapter, CDF have widely used [69] a mass modelization of the hadronic background classifying, and individually modeling, the overall background in four different categories, namely: the combinatorial background, the partially reconstructed peaking background, the background due to non-peaking partially reconstructed decays and finally the reflections due to the Cabibbo suppressed decay. Inclusive Monte Carlo simulations are used to parameterize the mass distributions of the physical contributions while side bands are used to create adequate templates for the combinatorial background in the ct sector.
Therefore, a common fitting strategy is applied to all the channels, that can be summarized with the following steps:

① Perform likelihood fit on invariant mass distribution within a large mass window ($[4.7, 6]\ GeV/c^2$).

② Fix the mass distribution template parameters and extract the combinatorial templates from the right mass side-band.

③ Use the mass window ($[5.2, 5.7]$ GeV/c^2 for B^+ and B_d^0, $[5.32, 5.72]$ GeV/c^2 for B_s^0) to perform the combined likelihood mass-proper time fit.

With this procedure a good description of the combinatorial background template is kept, while at the same time, the contamination (in the ct distribution) from the partially reconstructed B meson decays, is reduced below 1% level of the total background in the fitting region.

6.1 Mass Templates

In hadronic decay modes, the candidates are completely reconstructed and signal events are recognized identifying a resonance peak in the invariant mass distribution. Hence, the signal is finally selected via a likelihood fit in the invariant mass distribution of the candidate tracks. As shown in Figure 6.3, the distributions for hadronically reconstructed B meson present a complex structure, especially in the low mass region close to the signal peak. The resonance peaks close to the signal one suggest that most of the background is produced from B not completely reconstructed or with wrong mass assignment to the tracks. Then, to understand the B background contribution a sample of inclusive b decays is needed. For this purpose an inclusive Monte Carlo sample with a mixture of B mesons (38.9% B_u, 38.9% B_d, 10.7% B_s ,11.6% Λ_b) has been generated. For each event a single b quark was generated and forced to hadronize into mesons and baryons according to the fractions listed above. Then the B meson was let decay following the most recent EvtGen [77] decay table, and the interaction of the decay products with the detector was simulated with the dedicated software together with the trigger logic. The details of simulation are the same presented for the signal Monte Carlo and described in Section 4.3. Finally the Monte Carlo events were reconstructed using the same prescription used for data and listed in Table 4.2. Figure 6.1 shows the mass distributions of the inclusive simulation for the five reconstructed decay modes. These plots, compared to the mass plots obtained from data (Fig. 6.3), show that the partially reconstructed B mesons generate the complex structure at the low mass region with respect to the signal peak (the red one in the 6.1 plots). In all the cases the main contribution appears coming from decay modes involving the excited state of D mesons ($D^\star$). In the golden channels ($B_d^0 \to D^-\pi^+$; $B^+ \to \bar{D}^0\pi^+$; $B_s^0 \to D_s^-\pi^+$), the $D^\star$ modes are responsible for the double peak structure on the right side of the signal peak. In fact, when an excited D meson state is involved, it decays on a more stable D state emitting a neutral pion or a γ. Because the conservation of the angular momentum, the $D^\star$ meson comes from the B meson in a polarized state. Therefore the final D meson, in the presence of a γ emission, can carry only a quantized fraction of the total momentum, resulting in the *double-horn* structure in the low mass region.

B Background Characterization

Looking at the specific decay modes, the inclusive simulation help to determine the main contributions and classifying them.
In the $B_d^0 \to D^-\pi^+$ mode the dominant contributions can be classified in the already

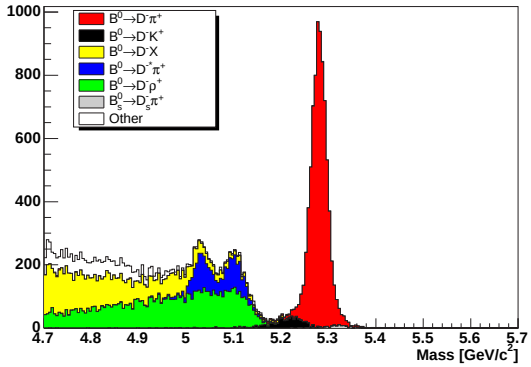

(a)

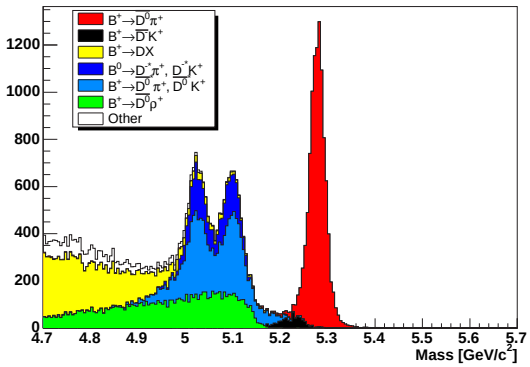

(b)

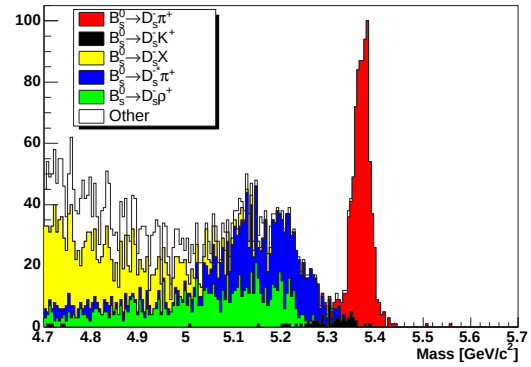

(c)

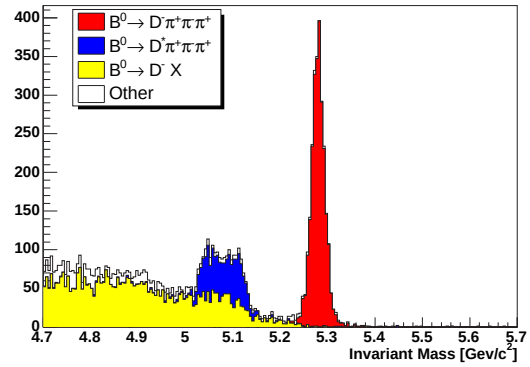

(d)

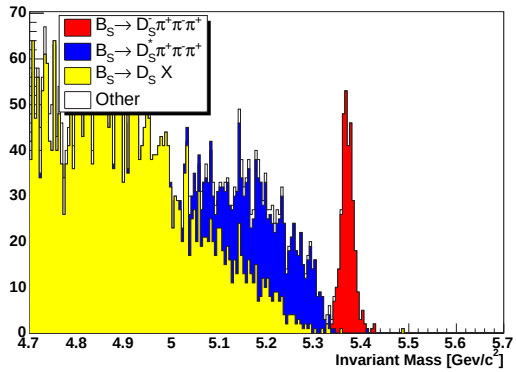

(e)

Figure 6.1: *Inclusive Monte Carlo mass distributions for the five decay mode studied in this analysis. (a) $B^0_d \to D^- \pi^+$; (b) $B^+ \to \bar{D}^0 \pi^+$; (c) $B^0_s \to D^-_s \pi^+$; (d) $B^0_d \to D^- \pi^+ \pi^- \pi^+$; (e) $B^0_s \to D^-_s \pi^+ \pi^- \pi^+$. Contributions from partially reconstructed B decays are also shown.*

quoted $D^{\star-}$ modes, where a neutral particle is lost during reconstruction, the $D^-\rho^+$ and the D^-X decay modes. $B_d^0 \to D^-\rho^+$ decay mode has a Branching ratio roughly 2 times bigger than the signal mode, therefore its contribution is supposed to be high when the D tracks fire the trigger. The $\rho^\pm$ resonance decay almost any times in a $\pi^0\pi^\pm$ modes, then the charged pion is reconstructed together with the charmed meson while the neutral pion is lost. Then the mass distribution of the $D^\mp + \pi^\pm$ appears as a smeared distribution at lower mass values with respect to the signal resonance (see Fig. 6.1 (a)). The D^-X mode (called also continuum) takes into account for all the B decays modes not involving the signal, the Cabibbo suppressed D^-K^+ and the previous $D^-\rho^+$ modes. Therefore it includes also the semileptonic modes, which do not contribute in a significant way, and all other multi bodies modes. Within these contributions there isn't any dominant decay mode, therefore they have been grouped together. Finally $B_s^0 \to D_s^-\pi^+$ contamination, even if almost negligible, is present in the high mass region under the signal peak and has been taken into account.
The $B_s^0 \to D_s^-\pi^+$ mode present the same dominant contribution observed in the B_d^0 case. $D_s^{\star-}\pi^+$ and $D_s^-\rho^+$ contributions are the main decay modes. Anyway in this case the statistic is not enough to clearly distinguish the *double-horn* structure from the excited D_s state, therefore the mass distribution of the $D_s^{\star-}\pi^+$ contamination appears like a smeared Gaussian close to the signal peak. The $D_s^-\rho^+$ contribution is similar to what has been seen in the B_d^0 case (see Fig. 6.1 (c)). Finally residual D_s^-X modes have been collected within a single group and used to create a single template.
In the $B^\pm$ mass distribution (Fig. 6.1 (b)) the dominant contribution is played by the excited D modes. Here an enhancement is provided by two different excited D modes, the charged ($D^{\star-}$) and the neutral one ($D^{\star0}$). Both of them decay in a $D^0\pi$ mode, where the pion can be neutral or charged. Therefore reconstructing the $D^0\pi^\pm$ invariant mass distribution we get contamination from the $B^\pm \to D^{\star0}\pi^\pm$ and also from the $B_d^0 \to D^{\star\pm}\pi^\mp$. Then, both the neutral and charged excited D generate the *double horn* phenomenon when a photon is lost, enhancing the resonant peaks close to the signal one. As for the other neutral modes a $D^0\rho^+$ contribution is present, but in this case it has been grouped with the D^0X continuum background to form a single mass template.
Finally the multi bodies decay modes $B_d^0 \to D^-\pi^+\pi^-\pi^+$ and $B_s^0 \to D_s^-\pi^+\pi^-\pi^+$, can be treated together. Again the dominant contribution come from exited D meson states not fully reconstructed that should provide the typical *double horn* structure when the $D_{(s)}^\star$ decays emit a γ ray. Anyway lack of statistic in the B_s^0 case, does not permit the observation of this phenomenon (see Fig. 6.1 (d) (e)).
There aren't other dominant contributions in these decay modes, therefore we preferred to put all the residual contributions together and consider them as $D_{(s)}^-X$ contribution.

B Background Mass Templates

The inclusive simulation used to understand the different background contributions from partially reconstructed B, is used also to create adequate mass templates in order to fit the data mass distributions and extract the signals.
For each decay mode the B background is splitted in different components, usually the

dominant ones, then each component has been used to extract a mass template subsequently used in the mass fit of data distribution. Binned likelihood fits were then performed to extract the parameters of the template distributions, and each invariant mass background contribution, shown in Fig. 6.2, has been parametrized as follow:

$[\mathbf{B_s^0 \to D_s^- \pi^+}]$

- ✯ $D_s^\star$: single Gaussian;
- ✯ continuum : first order polynomial;
- ✯ $D_s\rho$: Gaussian + inverse error function;

$[\mathbf{B_s^0 \to D_s^- \pi^+ \pi^- \pi^+}]$

- ✯ $D_s^\star$: inverted error function;
- ✯ continuum : expo-gauss + inverted error function + first order polynomial;

$[\mathbf{B_d^0 \to D^- \pi^+}]$

- ✯ $D^\star$: triple Gaussian;
- ✯ continuum : first order polynomial;
- ✯ $D\rho$: inverse expo-gauss;

$[\mathbf{B_d^0 \to D^- \pi^+ \pi^- \pi^+}]$

- ✯ $D^\star$: triple Gaussian;
- ✯ continuum : Gaussian + exponential + inverted error function + first order polynomial;

$[\mathbf{B^\pm \to \bar{D}^0 \pi^\pm}]$

- ✯ $D^\star$: triple Gaussian;
- ✯ continuum : exponential + first order polynomial;

The parametrization is quite arbitrary, even if theoretical considerations can be done to guess which should be the mass distribution for the dominant decay modes. Then, Binned fits were performed using the templates association shown above. Fits on single templates result in a good χ^2, confirming the validity of the suggested parametrization. Details on the analytical implementation of the templates in the mass sector of the likelihood are described in Appendix A.

6.2 Mass Fit

The first step of the fitting strategy, requires to perform a mass fit in a wide mass region, in order to estimate all the background contributions coming from partially reconstructed B mesons.
Therefore unbinned maximum likelihood fits on invariant mass distributions were performed for the five decay modes. The background contributions coming from the partially reconstructed B are parametrized with the templates proposed in the previous section, while an exponential plus a first order polynomial is used to describe the combinatorial background. The signal peak is modeled with a Gaussian, and a Gaussian with fixed parameters is included in the fits to take into account for the Cabibbo suppressed decay modes in the three golden modes: $B^\pm \to \bar{D}^0 K^\pm$, $B_d^0 \to D^- K^+$ and $B_s^0 \to D_s^- K^+$.

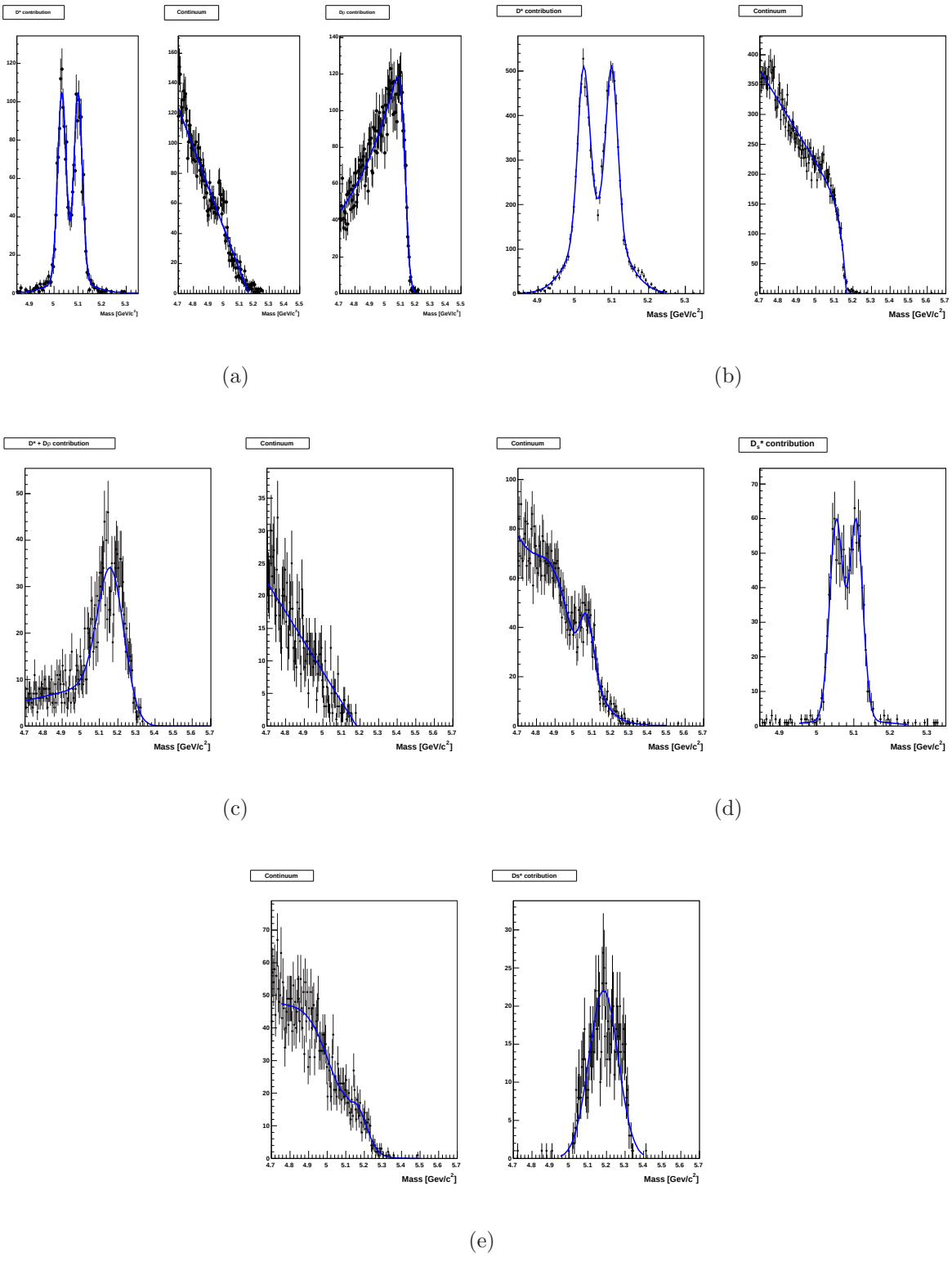

Figure 6.2: *Mass templates for the main partially reconstructed contributions. (a)* $B_d^0 \to D^-\pi^+$*; (b)* $B^+ \to \bar{D}^0\pi^+$*; (c)* $B_s^0 \to D_s^-\pi^+$*; (d)* $B_d^0 \to D^-\pi^+\pi^-\pi^+$*; (e)* $B_s^0 \to D_s^-\pi^+\pi^-\pi^+$*.*

The Cabibbo suppressed contribution is fixed using the Monte Carlo studies. The parameters of the Gaussian distribution, used to template this contribution, are fixed with respect to the signal peak, in order to avoid possible absolute scale shifts deviations on simulations. In fact, even if a inclusive Monte Carlo is able to reproduce the main contributions of partially reconstructed B, the mass fit is performed letting floating some template parameters that are related to the absolute energy scale, such as the centroids of satellite peaks or end-point of continuum background. Thus the mass templates became more reliable and the fit quality increases.
The general form of the Probability Density Function ($p.d.f.$) used to perform the mass Likelihood fit is:

$$\begin{aligned}\mathcal{L}(m) &= f_S \cdot \mathcal{L}_S(m) \\ &+ (1 - f_S) \cdot f_{comb.} \cdot \mathcal{L}_{Comb}(m) \\ &+ (1 - f_S) \cdot (1 - f_{comb.}) \cdot \sum_{i=0}^{N} f_{B_i} \cdot \mathcal{L}_{B_i}(m). \end{aligned} \tag{6.1}$$

Where the contributions for the signal and the combinatorial background can be expressed as:

$$\begin{aligned}\mathcal{L}_S(m) &= \frac{1}{1 + f_{DK}} \left(\frac{1}{\sqrt{2\pi}\sigma_B} e^{-\frac{1}{2}\frac{(m-\mu_B)^2}{2\sigma_B^2}} + f_{DK} \cdot \frac{1}{\sqrt{2\pi}\sigma_{DK}} e^{-\frac{1}{2}\frac{(m-\mu_{DK})^2}{2\sigma_{DK}^2}} \right); \\ \mathcal{L}_{Comb}(m) &= (1 - f_{flat}) \cdot \frac{s}{e^{-s \cdot m_{min}} - e^{-s \cdot m_{max}}} \cdot e^{-s \cdot (m - \frac{m_{max} - m_{min}}{2})} + f_{flat} \end{aligned} \tag{6.2}$$

Clearly the f_{DK} contribution, that stands for the Cabibbo suppressed signal, is non zero for the three D+single track decay modes only. The branching ratio of this modes is reduced by the Cabibbo term $|V_{us}|^2$ in the CKM Matrix, explaining the *suppressed* terminology. In the reconstruction procedure used, no particle identification is applied, and a pion mass is assigned to the track pointing to the secondary vertex. Therefore the invariant mass distribution of the reconstructed $B \to D_{(s)}K$ meson appears as a small peak shifted at lower values w.r.t the $B \to D_{(s)}\pi$ mode (see the black contribution in Fig. 6.1). The f_{DK} term was evaluated starting from the measured branching ratios and the different detector efficiencies for kaon and pion tracks:

$$f_{DK} = \frac{Br(B \to DK)}{Br(B \to D\pi)} \cdot \frac{\epsilon_{MC}(DK)}{\epsilon_{MC}(D\pi)} \tag{6.3}$$

where $\epsilon_{MC}(DK)$ and $\epsilon_{MC}(D\pi)$ are the Monte Carlo efficiencies for the two decay modes. The last terms in Eq.6.1, $f_{B_i} \cdot \mathcal{L}_{B_i}(m)$ refer to the $p.d.f.$ used for the partially reconstructed background contributions, described by the templates introduced in the previous section. Details on the functional form of the different templates used are given in Appendix A.
Finally an unbinned maximum likelihood fit was performed for the five decay modes listed at the beginning of Chapter 4.
Figures 6.3 show the fitted distributions on the wide mass range $[4.7, 6.0]$ GeV/c^2. Global fits and single contributions are also shown. The five fit results are listed in the Tables 6.5,

6.4, 6.6, 6.3, 6.7, at the end of this Chapter. In these tables, the values marked as FIXED refer to the fits results of template fits that have been fixed during the unbinned mass fits. Details on what the template parameters represent are given in Appendix A.

The reliability of the fitter has been demonstrated in Section 5.3.1. Here, a test on the fit quality, has been done performing a χ^2 test. The tests show good agreement within the statistical errors of the templates used. The main results of these mass fits can be summarized as follow:

$[\mathbf{B_s^0 \to D_s^- \pi^+}]$

- ☆ Reconstructed B_s^0: 472 ± 27;
- ☆ B_s^0 Mass : 5,365.6 ± 1.1 MeV/c^2;
- ☆ B_s^0 Width : 16.6 ± 1.1 MeV/c^2
- ☆ $\chi^2/n.d.f.$: 80/96 *Prob.* 88%

$[\mathbf{B_d^0 \to D^- \pi^+}]$

- ☆ Reconstructed B_d^0: 7957 ± 80;
- ☆ B_d^0 Mass : 5,278.89 ± 0.29 MeV/c^2;
- ☆ B_d^0 Width : 15.7 ± 0.25 MeV/c^2
- ☆ $\chi^2/n.d.f.$: 133/130 *Prob.* 41%

$[\mathbf{B_s^0 \to D_s^- \pi^+ \pi^- \pi^+}]$

- ☆ Reconstructed B_s^0: 133 ± 23;
- ☆ B_s^0 Mass : 5,368.7 ± 1.8 MeV/c^2;
- ☆ B_s^0 Width : 17.7 ± 4.1 MeV/c^2
- ☆ $\chi^2/n.d.f.$: 116/130 *Prob.* 80%

$[\mathbf{B_d^0 \to D^- \pi^+ \pi^- \pi^+}]$

- ☆ Reconstructed B_d^0: 4173 ± 115;
- ☆ B_d^0 Mass : 5,278.49 ± 0.42 MeV/c^2;
- ☆ B_d^0 Width : 26.55 ± 0.30 MeV/c^2
- ☆ $\chi^2/n.d.f.$: 137/130 *Prob.* 31%

$[\mathbf{B^\pm \to \bar{D}^0 \pi^\pm}]$

- ☆ Reconstructed $B^\pm$: 8380 ± 104;
- ☆ $B^\pm$ Mass : 5,278.44 ± 0.25 MeV/c^2;
- ☆ $B^\pm$ Width : 17.81 ± 0.23 MeV/c^2
- ☆ $\chi^2/n.d.f.$: 163/130 *Prob.* 2.7%

The mass value obtained from the fits are in agreement with the world average values [41] (B_s^0 mass 5369.6 ± 2.4 MeV/c^2, B_d^0 mass 5279.4 ± 0.5 MeV/c^2, $B^\pm$ mass 5279.0 ± 0.5 MeV/c^2) within the statistical errors, while the widths represent the detector resolutions for each decay mode.

6.3 Combined Mass-Lifetime fits

When the mass fit is performed all the contributions are estimated, so they can be kept under control. This is the underlying idea of the combined maximum likelihood fit on mass and proper time quantities. Thanks to the mass information, the different contributions can be separated and the relative fractions are under control during the lifetime

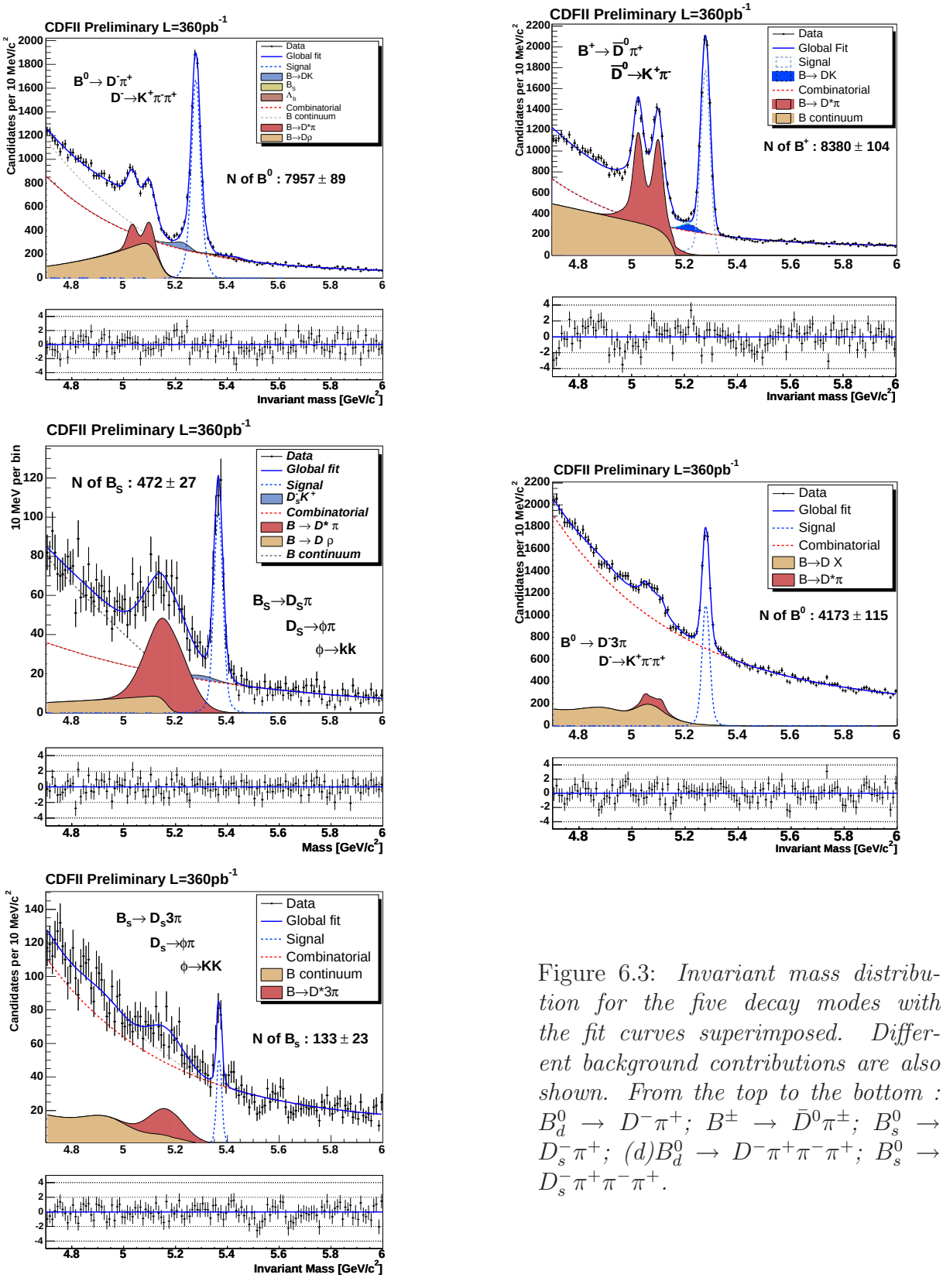

Figure 6.3: *Invariant mass distribution for the five decay modes with the fit curves superimposed. Different background contributions are also shown. From the top to the bottom :* $B_d^0 \to D^-\pi^+$; $B^\pm \to \bar{D}^0\pi^\pm$; $B_s^0 \to D_s^-\pi^+$; *(d)* $B_d^0 \to D^-\pi^+\pi^-\pi^+$; $B_s^0 \to D_s^-\pi^+\pi^-\pi^+$.

fit. More over, the use of additional information help to reduce the error estimation in the fit.
The mass sector and how to create template distributions for all the dominant contributions has been already discussed in previous sub-sections, here the proper time sector is described and the results of the combined fit are shown.
At CDF II the proper decay time of a reconstructed particle is derived from other measured quantities and then defined as:

$$ct = m_{PDG} \cdot \frac{L_{xy}}{p_T}. \tag{6.4}$$

Where m_{PDG} is the world average mass value [41] of the reconstructed particle, p_T is the measured transverse momentum, and L_{xy} is the decay length projected in the direction of the particle momentum:

$$L_{xy} = \frac{\vec{D}_{xy} \times \vec{p}_T}{|\vec{p}_T|}, \tag{6.5}$$

where $\vec{D}_{xy}$ is the transverse decay length oriented in the outgoing direction. The decay length is measured as the difference between the B meson production point (primary vertex) and the decay point (secondary vertex). The secondary vertex position, and the corresponding error matrix, are given by the vertex fit of the B meson candidate tracks, while the primary vertex is determined as the point on the beamline calculated at the B meson candidate z position and used in a average run basis. The primary vertex error matrix is extracted from the measured beam profile. The use of m_{PDG} allows for a better lifetime resolution by removing the uncertainty on the mass measurement of the candidate. Anyway this choice introduces some problems in the *scaling properties* of the background contribution far from the signal region, and therefore have to be corrected for the mass when creating templates of background proper time distributions.

6.3.1 Lifetime Templates

The main background contribution under the signal peak is the combinatorial one, and its proper time template distribution is needed for the combined fit. This has been done by constructing a template distribution directly from the ct distribution of a conveniently defined sideband in the high invariant mass region. As mentioned before, the ct quantity is defined using the m_{PDG}, and the proper time distribution is not constant in different mass region, consequently, the background template distribution taken at high mass value, may not correctly describe the ct distribution under the signal peak.
The use of average ct distributions obtained using the combinatorial background in both the high and the low mass regions, is not a viable solution due to the presence of partially reconstructed B. It requires not only the knowledge of different background fractions[1], but also a reliable estimation of the proper time distribution of the B mesons, that will be a lifetime measurement itself!
To model the combinatorial background ct distribution in the fit range, a rescaling procedure is adopted.

[1] These could be extrapolated from the invariant mass fit.

Let $f(ct_{rec})$ be the function that describes the sideband ct distribution in a given mass region, and $g(m)$ be the mass distribution of all combinatorial background. Then the template distribution $h(ct)$ that describes the ct distribution in the mass range $[m_{LO}; m_{HI}]$ is obtained by:

$$h(ct) = \int_{m_{LO}}^{m_{HI}} f(ct \cdot \frac{m}{m_{PDG}}) g(m) \mathrm{d}m \tag{6.6}$$

where f is rescaled with a mass dependent factor and re-weighted in the whole mass range with the mass distribution of the background.
The sideband region used to extract the template is between 5.4 and 5.6 GeV/c^2 for the B_u and B_d modes, [5.45 - 5.6] GeV/c^2 for the B_s modes. A statistically well populated sideband region close to the signal but not including mis-reconstructed contribution such as Λ_b or B_s in the B_d^0 decay mode, has been selected.

The background proper time distributions extracted in this way, were then fitted using binned likelihood fits with ad hoc functional forms. Essentially a sum of exponentials convolved with Gaussians have been used:

$$p.d.f.(t)^{\alpha} = \frac{f_1}{\tau_1} e^{-\frac{t}{\tau_1}} \otimes \frac{1}{\sqrt{2\pi}\sigma_1} e^{-\frac{(t-\mu_1)^2}{2\sigma_1^2}} + \frac{1-f_1}{\tau_2} e^{-\frac{t}{\tau_2}} \otimes \frac{1}{\sqrt{2\pi}\sigma_2} e^{-\frac{(t-\mu_2)^2}{2\sigma_2^2}}; \tag{6.7}$$

$$p.d.f.(t)^{\beta} = \frac{f_1}{\tau_1} e^{-\frac{t}{\tau_1}} \otimes \frac{1}{\sqrt{2\pi}\sigma} e^{-\frac{(t-\mu)^2}{2\sigma^2}} + \frac{1-f_1}{\tau_2} e^{-\frac{t}{\tau_2}} \otimes \frac{1}{\sqrt{2\pi}\sigma} e^{-\frac{(t-\mu)^2}{2\sigma^2}}. \tag{6.8}$$

In practice, the first expression can be reduced to the second one when only one Gaussian is used to smear the exponentials. The $p.d.f.(t)^{\alpha}$ describes quite well the distribution for the B_u and B_d mesons, while the $p.d.f.(t)^{\beta}$ is a good parametrization for the B_s decay modes. Table 6.1 summarizes the fit results, while Figure 6.4 shows the projections of the fit results on the sidebands.

Param.	$B^{\pm}$	$B_d^0 \to D\pi$	$B_d^0 \to D3\pi$	$B_s^0 \to D_s\pi$	$B_s^0 \to D_s3\pi$
$p.d.f.$	α	α	α	β	β
f_1	0.85 ± 0.05	0.47 ± 0.16	0.59 ± 0.06	055 ± 0.16	0.87 ± 0.20
τ_1 (μm)	125 ± 16	134 ± 24	185 ± 7	102 ± 53	486 ± 44
τ_2 (μm)	389 ± 39	311 ± 32	440 ± 19	360 ± 31	110 ± 29
μ_1 (μm)	238 ± 10	303 ± 30	421 ± 7	155 ± 11	322 ± 17
μ_2 (μm)	118 ± 11	155 ± 16	235 ± 7		
σ_1 (μm)	64 ± 6	73 ± 20	40 ± 5	47 ± 7	92 ± 12
σ_2 (μm)	32 ± 7	50 ± 8	69 ± 6		
$\chi^2/n.d.f.$	72/77	20.7/23	117/124	32/25	20.7/23

Table 6.1: *Fit results of the combinatorial background on re-weighted sidebands.*

6.3.2 Combined Fits

In the previous sub-section the determination of the proper time template distributions for the combinatorial background has been discussed. In Chapter 5 the functional form

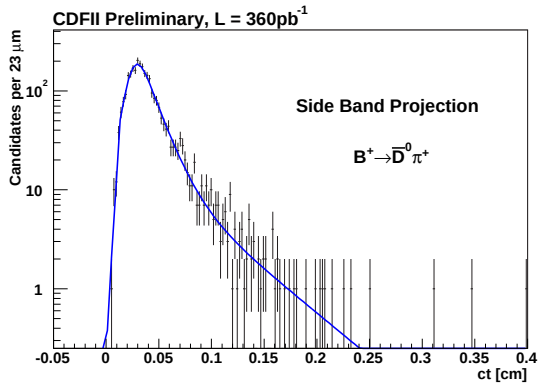

(a)

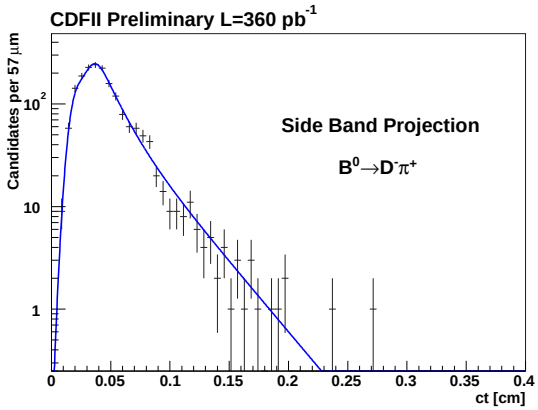

(b)

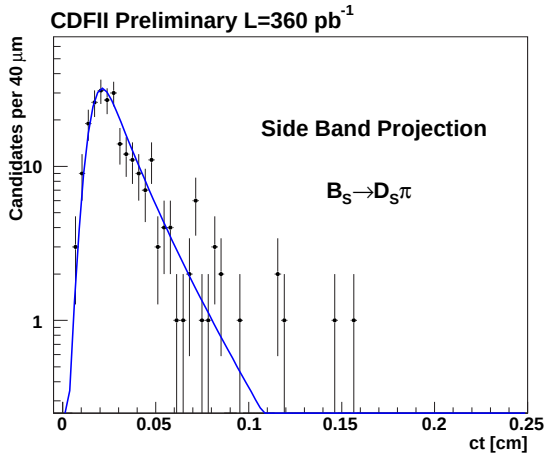

(c)

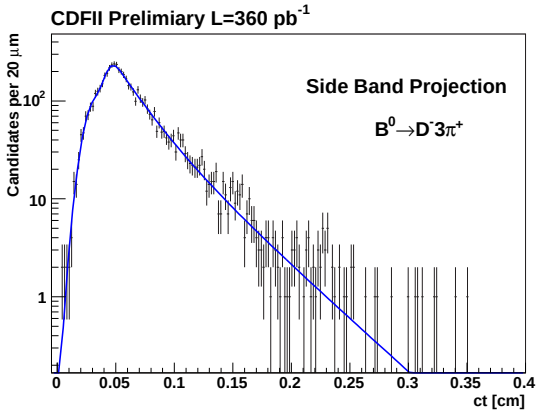

(d)

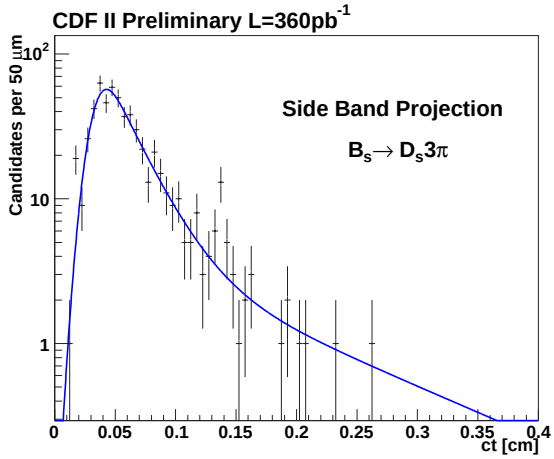

(e)

Figure 6.4: *Fit projections of the lifetime distributions on the side-band. Proper time distribution of the combinatorial background is shown for the five decay modes studied. (a) $B^+ \to \bar{D}^0\pi^+$; (b) $B_d^0 \to D^-\pi^+$; (c) $B_s^0 \to D_s^-\pi^+$; (d) $B_d^0 \to D^-\pi^+\pi^-\pi^+$; (e) $B_s^0 \to D_s^-\pi^+\pi^-\pi^+$.*

to model the signal contribution has been extracted. Here all the pieces are assembled together to create the complete likelihood.
As mentioned above the lifetime distributions of partially reconstructed B cannot be modeled. Therefore an asymmetric mass region around the signal peak is used for the combined fit, in order to reduce this kind of background contamination during the combined fit. The mass region chosen for the combined fit, ranges from 5.2 to 5.7 GeV/c^2 for B_u and B_d mesons, and from 5.32 to 5.72 GeV/c^2 for B_s decay modes.
Using these regions, the B background contamination is reduced at the 1% level of the total background and then is considered negligible.
A combined fit technique is applied to use all the information available and have a more precise parameters estimation, i.e. with a lower statistical error, thus, helping the discrimination of the different source of contributions. The final $p.d.f.$ is:

$$\begin{aligned}\mathcal{L}(m, ct, \sigma_{ct}) &= f_S \cdot \mathcal{L}_S(ct, \sigma_{ct}) \cdot \mathcal{L}_S(m) \\ &+ (1 - f_S) \cdot f_{comb.} \cdot \mathcal{L}_{Comb}(ct) \cdot \mathcal{L}_{Comb}(m) \\ &+ (1 - f_S) \cdot (1 - f_{comb.}) \cdot \mathcal{L}_{Comb}(ct) \cdot \sum_{i=0}^{N} f_{B_i} \cdot \mathcal{L}_{B_i}(m). \end{aligned} \tag{6.9}$$

In Eq. 6.9 the mass component is the same already presented in Eq. 6.1, while for the proper time sector the $\mathcal{L}_S(ct, \sigma_{ct})$ is the signal component, described by the Eq. 5.3, and the $\mathcal{L}_{Comb}(ct)$ is the functional form $p.d.f.(ct)^{\alpha,\beta}$ presented in Eq.: 6.7 and 6.8. The same parametrization is used for both the proper time combinatorial background and partially reconstructed B. Again this hypothesis holds whenever the partially B contribution is negligible w.r.t the other background sources. The mass window selected for the combined fits, guarantees that this contribution (the $\sum_{i=0}^{N} f_{B_i}$ term in the Eq. 6.9), is of the 1% level of the total background. Additionally in Chapter 7, tests are performed to check this assumption, and all of them show that this is a negligible source of systematics.
Finally we can note that the dependence on the proper time resolution is restricted to the signal term only. The use of fixed template turns in to the fact that only the signal term shows an explicit dependence on the proper time resolution. Usually, unbinned fits that make use of the resolution information need to introduce a *scale factor* to take into account for non Gaussian behavior and over/under estimation of the resolution itself. The *scale factor* is a floating parameter during the fits, and the fit determines its value. This is not the case for this analysis, where the proper time distribution, for both signals and background, does not show any prompt Gaussian peak, because the trigger and analysis selections have cut down the short-lived contribution.
Therefore, the scale factor cannot be estimated using this data sample. Because that, we decide to fix the scale factor to 1.3, evaluated from lifetime measurements using $B^{\pm} \to J/\psi K^{\pm}$ and $B_d \to J/\psi K^{0*}$ in previous analyses [72] where the trigger selections are looser. One can object that the error estimation and the error distribution change according to the selections used and then decay modes selected with different criteria should need different scale factors. Anyway, Monte Carlo Studies shown that the scale factor does not change within statistical errors after the trigger requirement are applied, more over as it will be shown in Chapter 7 the analysis is not much sensitive to the *scale factor* value, so that changing its value of the 10% produces negligible bias in the lifetimes

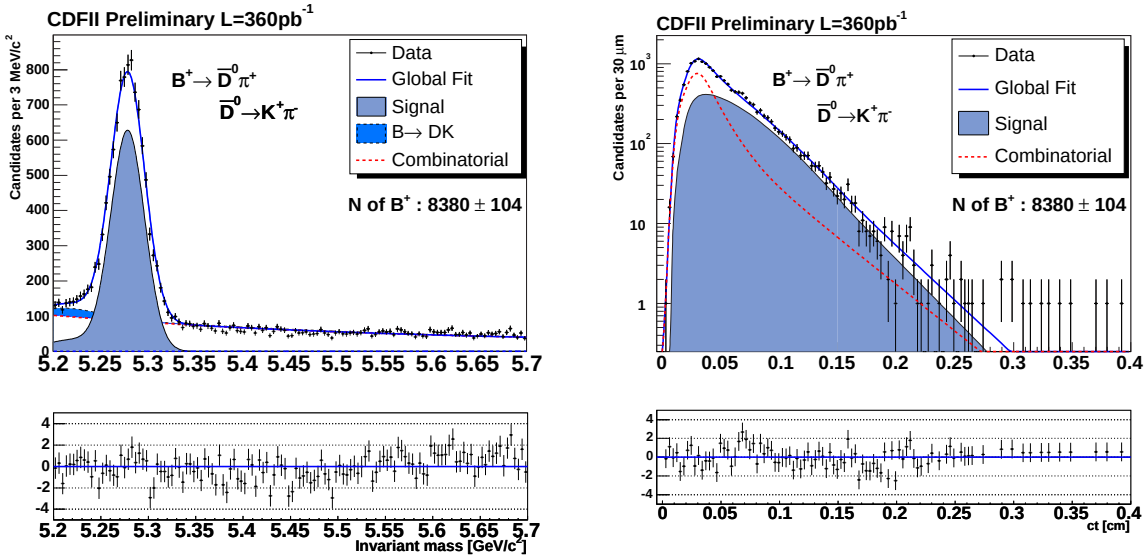

(a) (b)

Figure 6.5: *Fit projections for $B^+ \to \bar{D}^0\pi^+$ decay mode with the fit results superimposed. (a) Mass distribution, (b) proper time distribution.*

fit results. In the following, each decay mode will be analyzed separately.

$B^+ \to \bar{D}^0\pi^+$

In the combined mass-lifetime fit the parameters left floating were the B^+ mass, the mass resolution of the signal Gaussian and the B^+ lifetime.
The remaining parameters are fixed either to the values obtained from the wide mass range fit (see Table 6.5) or to the values coming from the combinatorial proper time template distributions. As mentioned above, we fix the scale factor on the proper decay time error to 1.3. Hence, an unbinned maximum likelihood fit with ct error event by event was performed on data. The results of the fit are reported below, and the projections of the likelihood on the invariant mass and proper decay time distributions are shown in Fig. 6.5.

- Number of Signal events in the window $= 8380 \pm 104$
- $B^\pm$ mass $= 5278.64 \pm 0.24\, MeV/c^2$
- $B^\pm$ width $= 17.96 \pm 0.21\, MeV/c^2$
- $B^\pm$ lifetime $= 498 \pm 8\, \mu m$

The Cabibbo suppressed contribution is not included in the number of $B^\pm$.
The obtained result for the lifetime is in good agreement with the current world average

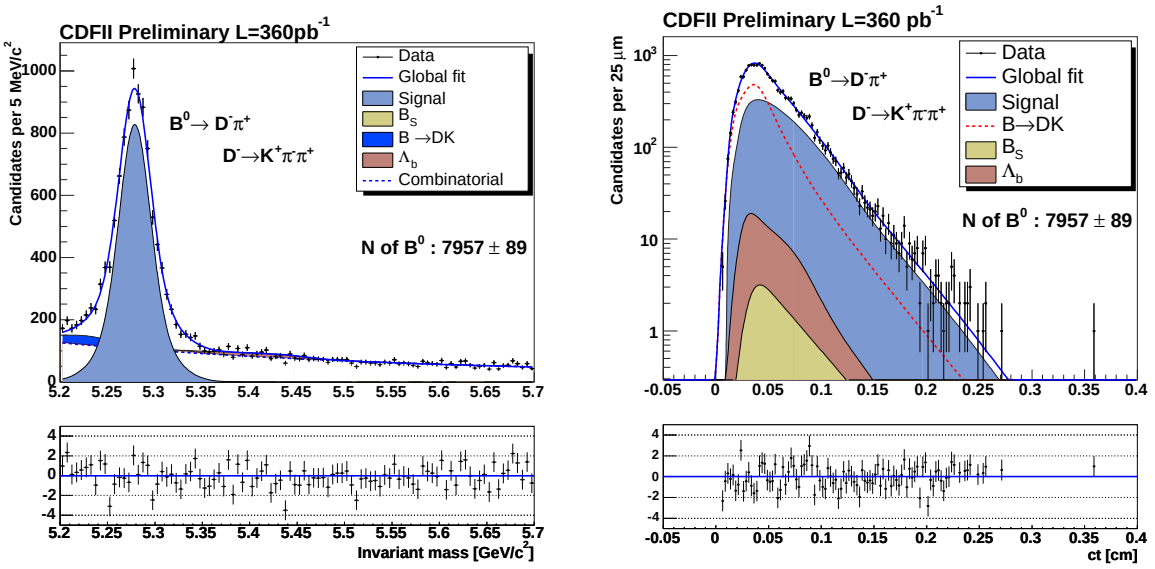

(a) (b)

Figure 6.6: *Fit projections for $B_d^0 \to D^-\pi^+$ decay mode with the fit results superimposed. (a) Mass distribution, (b) proper time distribution.*

of $501 \pm 5\,\mu m$ [41].
The quality of the fit can be quantified with a χ^2 test between an histogram of the data and the overall $p.d.f.$ normalized to number of total entries in the histogram:

mass : $\chi^2/\text{ndf} = 164/130$; Prob = 3 %

lifetime : $\chi^2/\text{ndf} = 79/62$; Prob = 8 %

$B_d^0 \to D^-\pi^+$

The same fitting technique is used for the $B_d^0 \to D^-\pi^+$ decay mode also, with the B_d^0 mass, the B_d^0 mass resolution and the B_d^0 lifetime floating in the combined mass-lifetime fit.
The other parameters are fixed either to the values returned by the wide mass range fit, reported in Table 6.4, or to values derived from the combinatorial proper time template distributions. Again, we fix the scale factor on the proper decay time error to 1.3.
The unbinned maximum likelihood fit with ct error event by event results are:.

- number of signal events = 7956 ± 80
- B_d^0 mass = $5279.6 \pm 0.5\,MeV/c^2$
- B_d^0 width = $15.9 \pm 0.4\,MeV/c^2$
- B_d^0 lifetime = $457 \pm 8\,\mu m$

The projections of the likelihood on the invariant mass and proper decay time are shown in Fig. 6.6. The lifetime obtained is in good agreement with the current world average of $460.5 \pm 4.2\,\mu m$ [41].
The quality of the fit can be quantified with a χ^2 test between an histogram of the data sample and the overall $p.d.f.$ normalized to number of total entries in the histogram:

mass : $\chi^2/\text{ndf} = 190/160$; Prob = 5 %

lifetime : $\chi^2/\text{ndf} = 38/28$; Prob = 10 %

In Fig. 6.6 contributions coming from the $B_s^0 \to D_s^- \pi^+$ and $\Lambda_b \to \Lambda_c^- \pi^+ (\Lambda_c \to pK\pi)$ contaminations are shown. These contributions were in fact added to the global $p.d.f.$ in the combined fit. Mass and proper time distributions for those contaminations were fixed from simulations, and the relative ratios of these contributions w.r.t. the signal were fixed using measurements from other experiments [41]. In practice, the the overall $p.d.f.$ used for the fit presents two additional terms w.r.t. the one in Eq. 6.9; the $p.d.f.$ used can be written as:

$$\begin{aligned}
\mathcal{L}^{B_d^0 \to D^- \pi^+}(m, ct, \sigma_{ct}) &= f_S \cdot \mathcal{L}_S(ct, \sigma_{ct}) \cdot \mathcal{L}_S(m) \\
&+ (1 - f_S) \cdot f_{comb.} \cdot \mathcal{L}_{Comb}(ct) \cdot \mathcal{L}_{Comb}(m) \\
&+ (1 - f_S) \cdot (1 - f_{comb.}) \cdot \mathcal{L}_{Comb}(ct) \cdot \sum_{i=0}^{N-2} f_{B_i} \cdot \mathcal{L}_{B_i}(m) \\
&+ (1 - f_s) \cdot (1 - f_{comb.}) \cdot f_{B_{\Lambda_b}} \cdot \mathcal{L}_{\Lambda_b}(ct) \cdot \mathcal{L}_{\Lambda_b}(m) \\
&+ (1 - f_s) \cdot (1 - f_{comb.}) \cdot f_{B_{B_s}} \cdot \mathcal{L}_{B_s}(ct) \cdot \mathcal{L}_{B_s}(m).
\end{aligned} \tag{6.10}$$

Details on the templates used for these contributions are presented in Appendix A.

$B_d^0 \to D^- \pi^+ \pi^- \pi^+$

In the combined mass-lifetime fit the B_d^0 mass, the B_d^0 mass resolution, the B_d^0 lifetime and all the background template parameters in ct sector are let floating. Here the combinatorial ct templates are free in order to better take into account this dominant contribution. The re-scaling procedure used to estimate the proper time combinatorial background does not solve completely the bias due to taking the proper time template distribution from the high mass region only. Then, when the combinatorial statistics become dominant a better description of the combinatorial ct distribution can obtained determining the template parameters directly on data. Therefore the ct template parameters of the combinatorial background are let floating during the combined fit. Anyway they did not change from the initial ones within the statistical errors. More over when the fitter is performed with the ct-parameters fixed, it returns in a lifetime deviation compatible with the systematic error evaluated in the next Chapter, and a worse fit quality.
The other parameters are fixed either to the values obtained from the wide mass range fit. We fix the scale factor on the proper decay time error, returned event by event by the vertex fit, to 1.3. The results of the fit are reported below and the projections of the likelihood on the invariant mass and proper decay time are shown in Fig. 6.7:

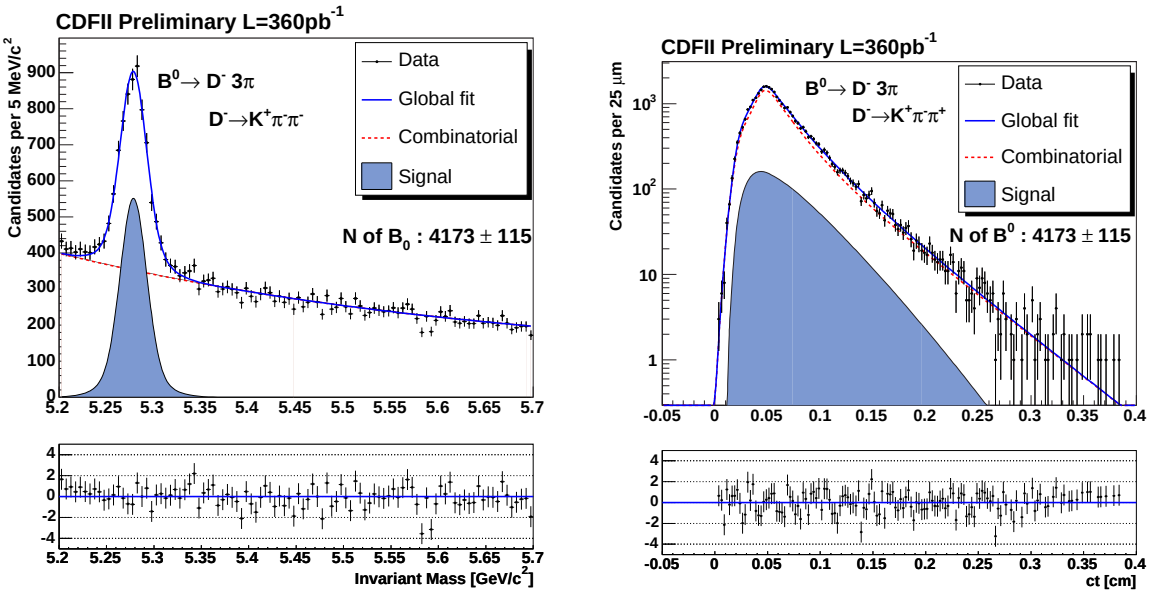

(a) (b)

Figure 6.7: *Fit projections for $B_d^0 \to D^-\pi^+\pi^-\pi^+$ decay mode with the fit results superimposed. (a) Mass distribution, (b) proper time distribution.*

Param.	Value	Units
fraction	0.66 (0.59) ± 0.04	
τ_1	202 (185) ± 9	μm
τ_2	455 (440) ± 14	μm
$mean_1$	412 (421) ± 6	μm
$mean_2$	232 (235) ± 9	μm
$width_1$	63 (40) ± 4	μm
$width_2$	69 (69) ± 4	μm

Table 6.2: *Values for the ct-side parametrization as obtained from the overall lifetime fit and as obtained from an independent binned fit on the sideband region $[5.4 - 5.6]$ GeV/c^2 after the re weight (in parenthesis).*

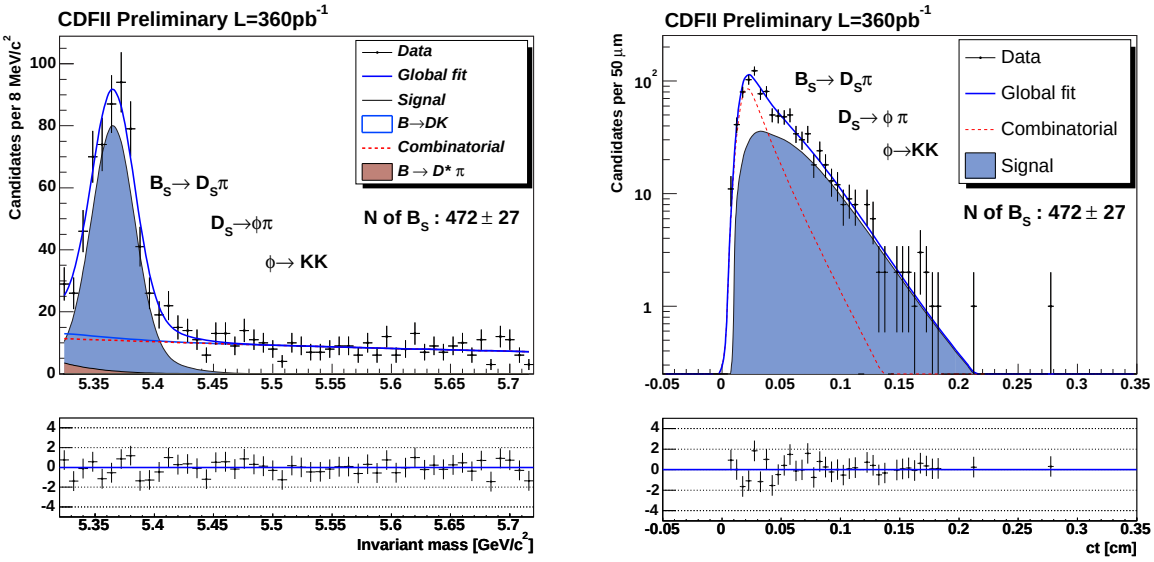

(a) (b)

Figure 6.8: *Fit projections for $B_s^0 \to D_s^- \pi^+$ decay mode with the fit results superimposed. (a) Mass distribution, (b) proper time distribution.*

- number of signal events $= 4173 \pm 115$
- B_d^0 mass $= 5278.4 \pm 0.4\, MeV/c^2$
- B_d^0 width $= 26.8 \pm 0.7\, MeV/c^2$
- B_d^0 lifetime $= 442 \pm 13\, \mu m$
- The combinatorial background parameters are reported in Table 6.2.

The measured B_d^0 lifetime is in agreement with the current world average of $460.5 \pm 4.2\, \mu m$ [41] and with the previous evaluation on the $B_d^0 \to D^- \pi^+$ decay mode.
The quality of the fit can be quantified with a χ^2 test between an histogram of the data sample and the overall *p.d.f.* normalized to number of total entries in the histogram:

mass : $\chi^2/\text{ndf} = 97/100$; Prob $= 56$ %

lifetime : $\chi^2/\text{ndf} = 86/87$; Prob $= 52$ %

As already mentioned, the combinatorial background parameters did not change within the statistical errors after the combined fit as shown in Table 6.2.

$B_s^0 \to D_s^- \pi^+$

B_s mass, B_s mass resolution, the B_s lifetime and the combinatorial lifetimes in the *ct* background (τ_1 and τ_2 in Eq. 6.8) are the floating parameters in the combined mass-lifetime fit.

As done in the previous fits, the scale factor on the proper decay time error is fixed to value 1.3, and all the remaining parameters are fixed to the values returned by the mass fit or to values derived from *ct* combinatorial templates. In this case, some combinatorial background parameters in the *ct* sector are free, because the lack of statistic in the side band sample used extract them. As shown in Fig. 6.4, the sample used to extract the proper time combinatorial background is little populated, so that the parameters determination cannot be precise. Therefore the lifetime parameters of the proper time combinatorial template distributions (τ_1 and τ_2) are free in the overall fit to estimate them in a more reliable way.
The results of the fit are reported below and the projections of the likelihood on the invariant mass and proper decay time are shown in Fig. 6.8:

- number of signal events = 465 ± 27
- B_s^0 mass = $5365.2 \pm 1.1\, MeV/c^2$
- B_s^0 width = $17.83 \pm 1.1\, MeV/c^2$
- B_s^0 lifetime = $479 \pm 32\, \mu m$
- $\tau_1 = 113(102)\ \pm 31\, \mu m$
- $\tau_2 = 214(360)\ \pm 16\, \mu m$

The quality of the fit can be quantified with a χ^2 test between an histogram of the data sample and the overall $p.d.f.$ normalized to number of total entries in the histogram:

mass : $\chi^2/\text{ndf} = 15/25$; Prob = 94 %

lifetime : $\chi^2/\text{ndf} = 16/18$; Prob = 58 %

The fit returns a B_s^0 lifetime value in agreement with the current world average of $438 \pm 17\, \mu m$ reported in the Particle Data Book [41].
The values in parenthesis for the τ_1 and τ_2 parameters, refer to fitted value on combinatorial background sample already presented in Table 6.1. While the τ_1 did not change within the errors, it seems that τ_2 was underestimated in the ct template. This feature comes from the lack of statistic used to create the template and it is the reason why they are let free during the combined fit.

$B_s^0 \to D_s^- \pi^+ \pi^- \pi^+$

Also for this multi bodies decay mode of the B_s^0 meson, the fit procedure used is the same. All the combinatorial background parameters, in both mass and proper time sector, are fixed during the fit. The mass background parameters are fixed to values from the mass fit, while the *ct* parameters are fixed to values derived from the side band template described at the beginning of this Section. Signal fraction is also fixed from the mass fit, and the floating parameters are then the B_s^0 mass, the B_s^0 mass resolution and the B_s^0 lifetime. Proper time resolution is fixed to 1.3 value as done in the other fits. Here,

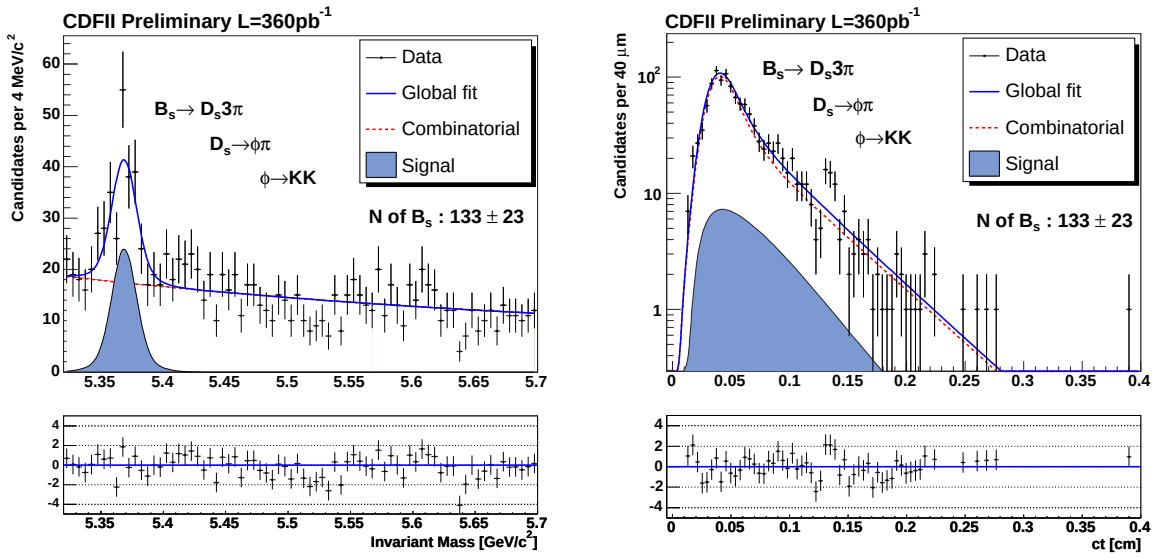

(a) (b)

Figure 6.9: *Fit projections for $B_s^0 \to D_s^- \pi^+ \pi^- \pi^+$ decay mode with the fit results superimposed. (a) Mass distribution, (b) proper time distribution.*

the statistics available in the *ct* combinatorial background sample is enough to generate a reliable template, so that the background parameters were fixed. Hence, a combined unbinned maximum likelihood fit was performed on this sample. The results of the fit are reported below and the projections of the likelihood on the invariant mass and proper decay time are shown in Fig. 6.9.

- number of signal events = 133
- B_s^0 mass $= 5,368.6 \pm 1.8\, MeV/c^2$
- B_s^0 width $= 18.8 \pm 3.4\, MeV/c^2$
- B_s^0 lifetime $= 480 \pm 71\, \mu m$

The quality of the fit is quantified with a χ^2 test between an histogram of the data sample and the overall *p.d.f.* normalized to number of total entries in the histogram:

mass : $\chi^2/\text{ndf} = 76/69$; Prob = 26 %

lifetime : $\chi^2/\text{ndf} = 39/33$; Prob = 21 %

The measured B_s^0 lifetime is in good agreement with the current world average of $438 \pm 17\, \mu m$ [41] and with the evaluation done in the $B_s^0 \to D_s^- \pi^+$ sample.

6.4 Combined Lifetimes Results

In this analysis, B_s^0, B_d^0 and $B^{\pm}$ have been completely reconstructed in 5 hadronic decay modes, and then the lifetime distributions have been fitted. For both B_s^0 and B_d^0, two independent lifetime measurements are available in $D\pi$ and $D\pi\pi\pi$ modes. The lifetime estimation is independent from the decay mode used to extract it, and they can be combined together to give a better result.
A weighted average is used to calculate the central value and the statistical error, therefore the measurements are weighted with their statistical uncertainty:

$$\bar{\tau} = \frac{\tau_{D\pi} \cdot \sigma_{\tau_{D\pi}} + \tau_{D3\pi} \cdot \sigma_{\tau_{D3\pi}}}{\sigma_{\tau_{D\pi}} + \sigma_{\tau_{D3\pi}}}, \qquad \sigma_{\bar{\tau}} = \left(\frac{1}{\sigma_{\tau^2_{D\pi}}} + \frac{1}{\sigma^2_{\tau_{D3\pi}}} \right)^{-\frac{1}{2}}. \tag{6.11}$$

Finally, quoting the weighted values for the neutral mesons, the final results are:

$$\begin{aligned} c\tau(B_d^0) &= 453 \pm 7\,(stat)\ \mu m, \\ c\tau(B_s^0) &= 479 \pm 29\,(stat)\ \mu m, \\ c\tau(B^{\pm}) &= 498 \pm 8\,(stat)\ \mu m. \end{aligned}$$

or

$$\begin{aligned} \tau(B_d^0) &= 1.510 \pm 0.022\,(stat)\ ps, \\ \tau(B_s^0) &= 1.599 \pm 0.096\,(stat)\ ps, \\ \tau(B^{\pm}) &= 1.661 \pm 0.028\,(stat)\ ps. \end{aligned}$$

The quoted errors are statistical only, and they are related to the samples size available. In the next Chapter we will discuss the dominant sources of systematic uncertainties that can affect our measurements. An estimation of all of them will be given and the final result will be quoted.

Parameter	Value	Units
Horn Frac. (f_1)	0.566 FIXED	
Horn center (μ_1)	5,080 FIXED	MeV/c^2
Horn offset (μ_2)	32.14 FIXED	MeV/c^2
Horn Main σ (σ_1)	37.85 FIXED	MeV/c^2
Horn sec. σ (σ_1)	10.19 FIXED	MeV/c^2
D^* rel. fraction ($f_{D^\star}$)	0.109 $\pm$0.035	
Endpoint (γ)	5,127 FIXED	MeV/c^2
Mean ($\mu_{rest.}$)	5,034 FIXED	MeV/c^2
Width ($\sigma_{rest.}$)	4,420 FIXED	MeV/c^2
τ ($\tau_{rest.}$)	0.059 FIXED	$MeV^{-1}c^2$
Mean Rev E-G (μ_{rho})	5,034 FIXED	MeV/c^2
a par. Rev E-G ($a_{rest.}$)	4,557 FIXED	GeV/c^2
b par. Rev E-G ($b_{rest.}$)	56,99 FIXED	GeV/c^2
Rel ratio E-G ($f_{rest.}$)	0.00004 FIXED	
comb. slope (s)	2,050 $\pm$ 0.096	MeV/c^2
comb. flat (f_{flat})	0.265 $\pm$ 0.026	
comb. ratio ($f_{comb.}$)	0.923 $\pm$ 0.013	
signal fraction (f_S)	0.037 $\pm$ 0.001	
B_d^0 mean	5,278.49 $\pm$ 0.42	MeV/c^2
B_d^0 width	26.55 $\pm$ 0.83	MeV/c^2

Table 6.3: *Results for Mass Fit wide mass window for $B_d^0 \to D^-\pi^+\pi^-\pi^+$. Details on the quoted variables are given in Appendix A.*

Parameter	Value	Units
Horn Frac. (f_1)	0.978 FIXED	
Horn center (μ_1)	5,066 FIXED	MeV/c^2
Horn offset (μ_2)	33.55 FIXED	MeV/c^2
Horn Main σ (σ_1)	113.8 FIXED	MeV/c^2
Horn sec. σ (σ_2)	17.61 FIXED	MeV/c^2
D^* fraction ($f_{D^\star}$)	0.030 ± 0.003	
gamma (γ)	5,150 FIXED	MeV/c^2
ρ scaling coeff. ($f_\rho/f_{D^\star}$)	4.63 ± 0.79	
mean ρ (μ_ρ)	5,130 FIXED	MeV/c^2
a par. ρ (a)	2.956 FIXED	GeV/c^2
b par. ρ (b)	25.65 FIXED	GeV/c^2
cont. coeff. ($f_{cont.}/f_{D^\star}$)	3.75 ± 0.59	
comb. flat (f_{flat})	0.571 ± 0.017	
comb. slope (s)	2.66 ± 0.14	$MeV^{-1}c^2$
comb. ratio ($f_{comb.}$)	0.571 ± 0.018	
signal fraction (f_S)	0.146 ± 0.004	
Λ_b rel. ratio ($f_{B_{\Lambda_b}}$)	0.045 FIXED	
B_s^0 rel. ratio ($f_{B_{B_s}}$)	0.008 FIXED	
B_d^0 mean	5,278.89 ± 0.29	MeV/c^2
B_d^0 width	15.17 ± 0.25	MeV/c^2

Table 6.4: *Results for Mass Fit wide mass window for $B_d^0 \to D^-\pi^+$. Details on the quoted variables are given in Appendix A.*

Parameter	Value	Units
Horn Frac. (f_1)	0.502 ± 0.023	
Horn center (μ_1)	5,062.55 ± 0.51	MeV/c^2
Horn offset (μ_2)	38.31 FIXED	MeV/c^2
Horn Main σ (σ_1)	64.11 FIXED	MeV/c^2
Horn sec. σ (σ_2)	15.94 FIXED	MeV/c^2
Mis reco rel. ratio ($f_{D^\star}$)	0.625 ± 0.016	
slope continuum ($s_{cont.}$)	4.201 FIXED	$MeV^{-1}c^2$
tau continuum (τ_m)	35.74 FIXED	$MeV^{-1}c^2$
endpoint continuum (α)	5.165 FIXED	MeV/c^2
comb. ratio ($f_{comb.}$)	0.559 ± 0.012	
comb. slope (s)	2.75 ± 0.12	$MeV^{-1}c^2$
comb. flat (f_{flat})	0.296 ± 0.017	
signal fraction (f_S)	0.132 ± 0.002	
$B^\pm$ mean	5,278.44 ± 0.25	MeV/c^2
$B^\pm$ width	17.81 ± 0.23	MeV/c^2

Table 6.5: *Mass fit results in the wide mass window for $B^\pm \to D^0\pi^\pm$. Details on the quoted variables are given in Appendix A.*

Parameter	Value	Units
D_ρ τ (a^{-1})	0.841 FIXED	$GeV^{-1}c^2$
Refl. σ ($\sigma_\star$)	75.6,00 FIXED	MeV/c^2
D_ρ a (a)	1.189 FIXED	$GeV^{-1}c^2$
D_ρ b (b)	32.19 FIXED	$GeV^{-1}c^2$
Refl. *mean* (μ_1)	5,165.4 ± 4.9	MeV/c^2
Rel. ratio (f_ρ)	0.151 FIXED	
point continuum (γ)	5.17 FIXED	GeV/c^2
comb. ratio ($f_{comb.}$)	0.52 ± 0.05	
comb. slope (s)	1.32 ± 0.13	$MeV^{-1}c^2$
comb. flat(f_{flat})	0.07 ± 0.01	
signal fraction (f_S)	0.101 ± 0.006	
B_s^0 mean	5,365.6 ± 1.1	MeV/c^2
B_s^0 width	16.6 ± 1.1	MeV/c^2

Table 6.6: *Mass Fit results in the wide mass window for $B_s^0 \to D_s^-\pi^+$. Details on the quoted variables are given in Appendix A.*

Parameter	Value	Units
Mean $D^\star$ (μ_1)	4,781 FIXED	MeV/c^2
a par. $D^\star$ (a)	86.38 FIXED	GeV/c^2
b par. $D^\star$ (b)	10.5 FIXED	GeV/c^2
D^* rel. fraction ($f_{D^\star}$)	0.298 $\pm$0.085	
Endpoint (γ)	5,190 FIXED	MeV/c^2
Mean E-G ($\mu_{rest.}$)	5,163 FIXED	MeV/c^2
Width E-G ($\sigma_{rest.}$)	63.7 FIXED	MeV/c^2
τ E-G ($\tau_{rest.}$)	3.68 FIXED	$MeV^{-1}c^2$
Mean Rev E-G (μ_ρ)	4,604 FIXED	MeV/c^2
a par. Rev E-G ($a_{rest.}$)	54,585 FIXED	GeV/c^2
b par. Rev E-G ($b_{rest.}$)	8,862 FIXED	GeV/c^2
Rel ratio E-G ($f_{rest.}$)	0.000018 FIXED	
comb. slope (s)	2,148 $\pm$ 218	MeV/c^2
comb. flat (f_{flat})	0.318 $\pm$ 0.076	
comb. ratio ($f_{comb.}$)	0.865 $\pm$ 0.038	
signal fraction (f_S)	0.019 $\pm$ 0.004	
B_s^0 mean	5,368.7 $\pm$ 1.8	MeV/c^2
B_s^0 width	17.7 $\pm$ 4.1	MeV/c^2

Table 6.7: *Mass Fit results in the wide mass window for $B_s^0 \to D_s^-\pi^+\pi^-\pi^+$. Details on the quoted variables are given in Appendix A.*

Chapter 7

Systematic Errors Determination

In this Chapter the determination of the systematic uncertainties related to the measurements presented are discussed.
Lifetime measurement of fully reconstructed decay modes are usually affected by systematic uncertainties coming from detector resolutions and misalignment, signal extraction, fitting model, etc. In ct biased fully reconstructed samples, a further source of systematic uncertainty have to be obviously taken into account. In our specific case this source is related on how well we are able to estimate the form of the ct efficiency function and correct for the effect.
As already done in other analyses [79], it will be shown that in such as environment CDF II is able to take under control all these systematic sources under the 3% level.
All the dominant sources of systematic error will be here presented and discussed. Because our determination of the efficiency function strongly relies on the ability of the Monte Carlo simulation to reproduce resolution effects on the trigger and offline quantities, the simulation behavior is actually the main subject of this Section.
Whenever the systematic evaluation is found to be independent from the decay mode, it has been evaluated for a single channel only.

7.1 *ct* Background Description

In the proper time sector, two contributions have been identified and used in the fits: the signal and the combinatorial background, Then the background characterization is necessary in order to have a reliable evaluation of the signal properties. Several assumptions such as the negligible contribution of the physical background, and the reliability of the template *ct*-distributions for the combinatorial one have been done. In this Section these assumptions are studied and validated.

7.1.1 Partially Reconstructed B

In the lifetime fit procedure, the hypothesis of negligible contribution from the partially reconstructed B in the mass fit region has been used. In fact, from the mass fit in the wide range $[\ 4.7 - 6.0\ GeV/c^2]$ it has been possible to evaluate this contribution in the regions $[\ 5.2 - 5.7\ GeV/c^2]$ and $[\ 5.32 - 5.72\ GeV/c^2]$, which was found to be less then

few % with respect to the overall background. To check the hypothesis and estimate the uncertainty associated with that the following procedure was applied.
During the combined mass-lifetime fit, the residual background contribution from B in the mass sector is linked to the combinatorial one in the ct sector. The B lifetime value is re-evaluated changing the association of the B background with the combinatorial background in the lifetime sector and fitting the proper time distribution of the partially reconstructed B as if they were the signal. Therefore, the $p.d.f.$ used in the fit was changed from the one in Eq. 6.9 to the following one:

$$\begin{aligned}\mathcal{L}(m, ct, \sigma_{ct}) &= f_S \cdot \mathcal{L}_S(ct, \sigma_{ct}) \cdot \mathcal{L}_S(m) \\ &+ (1 - f_S) \cdot f_{comb.} \cdot \mathcal{L}_{Comb}(ct) \cdot \mathcal{L}_{Comb}(m) \\ &+ (1 - f_S) \cdot (1 - f_{comb.}) \cdot \mathcal{L}_S(ct, \sigma_{ct}) \cdot \sum_{i=0}^{N} f_{B_i} \cdot \mathcal{L}_{B_i}(m), \end{aligned} \tag{7.1}$$

where in the third line the $\mathcal{L}_S(ct)$ term substituted the combinatorial term $\mathcal{L}_{Comb.}(ct, \sigma_{ct})$. Table 7.1 shows the fit results obtained whit this configuration for all the five decay modes studied. The comparison with the lifetime results obtained on the standard fit configuration shows negligible deviation for most of them. In the case of $B_s^0 \to D_s^- \pi^+$ and $B^\pm$, the deviations are instead not negligible. More over, for both the decay modes the last column in Table 7.1 shows that the background contribution in the fit region is greater then the percent level. Further studies, reported in Appendix B, show that a so large deviation is indeed a conservative estimation of this uncertainty: in fact this method to estimate the systematic error depends on the background description, therefore any uncertainty in the background modeling or parametrization interferes with our estimation.
For the B_s^0, the systematic error introduced by this effect is roughly 3 times smaller then the statistic one, and then does not affect in significant way the overall uncertainty. Clearly when the sample size will increase with the new data collected by CDF, the statistical error will became comparable with the systematic one. Anyway in Appendix B is shown that a different physics background modelization can provide a more reliable estimation of this uncertainty, that can be reduced at 1 μm level.

Standard Fit		Wrong background assignment	
Decay Mode.	$c\tau$ Standard Value (μm)	Deviation (μm)	Physics Back. %
$B_d^0 \to D^- \pi^+$	456.6 ± 7.6	0.1	0.1
$B_d^0 \to D^- 3\pi^+$	442.0 ±12.6	0.004	0.02
$B^+ \to \bar{D}^0 \pi^+$	498 ± 8	1.5	1.5
$B_s^0 \to D_s^- \pi^+$	479.4 ± 31.8	10	3.3
$B_s^0 \to D_s^- 3\pi^+$	479.7 ± 70.6	-	0.3

Table 7.1: *Fit results with wrong physical background association.*

7.1.2 Combinatorial Background

The combinatorial background template distribution in the *ct* sector has been extracted using the re-weighting technique described in Section 6.3.1. Even with this re-wighting technique, the background proper time distribution in the high mass region can be different from that under the signal peak. More over, in order to have a reliable background parametrization we took as sideband the mass region $[5.4 - 5.6]$ GeV/c^2, but the mass window used in the combined mass-lifetime fit includes this region. This is not statistically correct, so it is important to understand what is the bias introduced with this procedure.
To check for that, the same fit is performed with the lifetime parameters τ_1, τ_2 of the background parameterization let free. The choice of these parameters has been done because these are strongly correlated to the B lifetime. Table 7.2 shows the fit results on the $B_d^0 \to D^-\pi^+$ sample with the τ parameters free. The results on the standard fit are also shown. The returned values of the *free fit* agrees within the statistical errors with those of the standard fit reported in the same table, meaning that the background ct distribution is well parameterized.
The resulting B_d^0 lifetime variation is of 1 μm. Other background parameters such as

Standard Fit		Free *tau*	
Par.	Value	Value	Units
$c\tau$	456.6 ± 7.6	455.5 ± 7.8	μm
tau_1	134.8 FIXED	131.3 ± 6.0	μm
tau_2	310.4 FIXED	317.3 ± 7.9	μm

Table 7.2: *Fit results w/ and w/o fixing the background parameters.*

the mean and the width in the $p.d.f^{\alpha,\beta}(t)$ template are also released, and all variations lie within 1 μm, so this value is used as evaluation of the systematic error associated with the combinatorial background parametrization.
As said in Chapter 6, for the $B_s^0 \to D_s^-\pi^+$ and the $B_d^0 \to D^-\pi^-\pi^+$ decay modes, the combinatorial background ct-parameters are floating for statistical reasons. Therefore the systematic error evaluated in this sub-section does not apply to these modes.

7.1.3 Background fraction

The lifetime measurement is sensitive to the combinatorial background fraction. Even though this fraction has been fixed from a fit on a wide mass range, some bias can arise from the fact that the signal is under or overestimated. Therefore a lifetime fit is performed leaving the background fraction floating.
In the $B_d^0 \to D^-\pi^+$ decay mode, the fit gives a lifetime value of 454.6 μm. Comparing this number with the standard fit result, a systematic error of 2 μm is associated.

7.2 Impact Parameter Correlation

A fundamental role in the analysis is played by the capability of the Monte Carlo simulation to reproduce the impact parameter resolution at the trigger level, because the trigger efficiency curve is determined from that. Therefore any deviation from an adequate simulation will result in a bias in the final lifetime estimation.
The basic idea used to probe this effect is to study the correlation between the impact parameter estimation as performed by the trigger and the offline algorithms. This has been done in two way: the first method estimate the impact parameter correlation directly on data, while the second one determined how well the simulation reproduce this correlation.

In order to understand the total bias that the impact parameter correlation between trigger and offline quantities can introduce, we performed the lifetime measurements with different selection configurations. For each B candidate reconstructed the trigger selections on the impact parameter tracks is added, acting on the d_0 as reconstructed using offline algorithms. Then, for every couple of tracks of the reconstructed B, the impact parameter selections are performed on the d_0 as measured by SVT (the *online* impact parameter, d_0^{SVT}) and on d_0 as determined by the analysis algorithms (the *offline* impact parameter, d_0^{SVX}).
Given an impact parameter selection, all the previous requirements do not change except for the track I.P. in both the trigger and offline quantities. Therefore, for each selection the efficiency curve and *ct*-templates parameters were re-calculated according to the new selection criteria. Table 7.3 shows the variation from the default B lifetime value for different configurations using the $B_d^0 \to D^-\pi^+$ decay mode. Analogous results have been found for the $B^\pm$ mode.
The numbers in brackets in Table 7.3 refer to the lower value of the track impact parameter allowed. These variations are somehow an overestimation of the systematic error

B_d^0 results		
Cut Set	*Variation*	Units
ONL. + OFF.	-0.5	μm
ONL.(150) + OFF.	+1.8	μm
ONL.(180) + OFF.	+2.0	μm
ONL. + OFF.(150)	-1.1	μm
ONL. + OFF.(180)	0.0	μm

Table 7.3: *Results of different online (ONL.) and offline (OFF.) configurations for the I.P. cuts. Number in brackets refers to lower d_0 track cut (in μm).*

due to the impact parameter correlation, since in reality what matters for the trigger efficiency curve is not the absolute width of the d_0^{SVT} or d_0^{SVX} distributions, but the width of the difference between d_0^{SVT} and d_0^{SVX} as reproduced in simulated data compared to real data. In fact, the method used to take into account for the trigger bias, is sensitive to the correlations between the offline and the SVT impact parameter, and we have to be sure that these correlations are well reproduced in the simulation. Therefore a second method

Monte Carlo	
width1	26.2 ± 0.2 μm
width2	60.5 ± 1.3 μm
frac	81 ± 1 %
Data	
width1	28.81 ± 0.05 μm
width2	92.4 ± 0.4 μm
frac	79 ± 1 %

Table 7.4: *Fit results on the d_0^{SVT} - d_0^{SVX} distributions from data and Monte Carlo. frac is the fraction of the first narrow Gaussian*

to probe how well the simulation reproduce the offline-SVT impact parameter correlation is used.
This method compares the d_0 correlation distributions on data and MC samples using tracks from the primary vertex.
Fig. 7.1 shows the comparison between these distributions as obtained from inclusive J/ψ in data and from Monte Carlo.
The d_0^{SVT} - d_0^{SVX} distribution is fitted on data and Monte Carlo with a double Gaussian. Results are listed on Table 7.4.
Even if a double Gaussian is not the best functional form describing these distributions, it's clear that in both the distributions there are a narrow component and a wide one. Monte Carlo and data give the same estimation for the relative fraction of these two contributions, but the Gaussian widths are different.
Looking at these distributions, a way to estimate a systematic error on this effect is the following. Smear the offline impact parameter distribution on the simulation using a value obtained by the comparison between the results in Table 7.4, then extract the efficiency curve in Eq. 5.5 performing the trigger selections on the smeared d_0. Therefore perform the lifetime fit using this new efficiency and compare the result with the one obtained in the previous Chapter.
Subtracting in quadrature the widths of the narrow Gaussians gives a smearing value of $\sqrt{28.8^2 - 26.2^2} = 12$ μm, while subtracting in quadrature the widths of the wide Gaussians gives a smearing value of $\sqrt{92.4^2 - 60.5^2} = 69.6$ μm. These two values are combined in quadrature taking into account the relative fractions between wide and narrow Gaussians (20% and 80% respectively) to obtain a final smearing value of 33 μm.
This value is used to re-derive the proper time acceptance functions in the case of the `BCHARM` trigger selections and repeat the lifetime fit. The lifetime values before and after the smearing procedure are 455.6±9.1 and 454.6±9.1 μm respectively for the $B_d^0 \to D^-\pi^+$ decay mode.
The difference between the two values has been assumed as the evaluation of the systematic error associated with the impact parameter correlation effect.
A small variation is somehow expected even if the difference between the resolution is not negligible. In fact, since the L_{xy} requirement depletes the ct region sculpted by the lower cut on the track impact parameter performed by the trigger, then the turn-on on

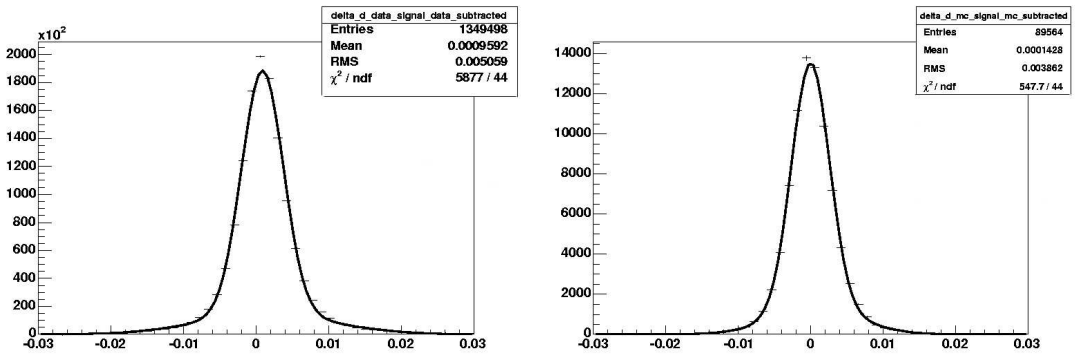

(a) (b)

Figure 7.1: The d_0^{SVT} - d_0^{SVX} distributions from data and Monte Carlo.

the proper time distribution is mostly determined by this selection.

7.3 B meson p_T and τ_{MC} dependence

As mentioned in Chapter 4 Monte Carlo samples have been generated with the default B meson p_T spectrum that is known to not reproduce completely data. Therefore a re-weighting procedure was applied to the Monte Carlo samples in order to minimize such a difference. However, residual discrepancies due to uncertainties in the assigned weights can still introduce some kind of bias in the lifetime measurement. In fact the weight factors come from a ratio between finite distribution and then they are subjected to uncertainties due to the available statistic.
To evaluate the bias due to these weights uncertainties, the Monte Carlo samples are re-weighted assigning weights incremented (decremented) by the error on the weight value. Then the corresponding efficiency curves are extracted and the lifetime fit is done.
Table 7.5 shows the fit results for a sigma variation on the assigned weight; half of this variation was assumed as the systematic uncertainty associated.

B_d^0 results		
Variation	$c\tau$	Units
$+\sigma$	458.4	μm
$-\sigma$	454.6	μm

Table 7.5: *Lifetime fit results for variations on the B meson p_T re-weight procedure. The default value is 456.6μm*

Another important issue is to understand how much the Monte Carlo input lifetime

value affects the final measurement. To understand that, different Monte Carlo samples with different input lifetimes should be generated and fitted for the lifetime using always the same efficiency curve, extracted from a sample generated with the central value. To avoid a so large Monte Carlo generation a different procedure is adopted. The *ct* distribution is rescaled by one sigma deviation ($\pm$ 4.2μm) according to the PDG [41] using the relation:

$$N(t)_{resc.} = N(t)\frac{\tau}{\tau_{resc.}} \cdot e^{\frac{t}{\tau} - \frac{t}{\tau_{resc.}}}, \tag{7.2}$$

where $\tau_{resc.}$ is the lifetime value of the *rescaled* sample. One can think that this procedure does not take into account for the trigger effect. In practice this is not true: the trigger selection acts on the proper time value trough the impact parameter requirement, and not on the average lifetime. For a given event with a fixed spatial topology, it will pass or not the trigger selection independently if it has been generated by a long or short lifetime value.
Therefore the efficiency function defined in Eq. 5.6 was re-evaluated re-fitting the efficiency distribution with the new rescaled numerator but also changing the τ_{MC} value at the denominator function. With the new efficiency curve we re-performed the complete fit on data.
Table 7.6 shows the results: as expected the variation is negligible.
Because the method is based on Monte Carlo simulation, is indeed important to proof that the method is not dependent on input lifetime parameter (τ_{MC}). Figure 7.2 shows the fit result on B_s^0 Signal Monte Carlo samples generated[1] with different lifetimes and fitted with the same efficiency curve extrapolated at 438 μm. The points can be fitted with a straight line with a slope compatible with the unity within the statistical errors, giving us confidence that the method is independent of input lifetime.

B_d^0 results		
Variation	cτ	Units
$+\sigma$	456.6	μm
$-\sigma$	456.5	μm

B_s^0 results		
Variation	cτ	Units
$+\sigma$	479.2	μm
$-\sigma$	478.8	μm

Table 7.6: *Lifetime fit results for 1 σ variation in the Monte Carlo cτ input. The default value are 456.6μm for B_d^0 and 479.4 μm for B_s^0.*

7.4 Parameterization model dependence

As already stated, the lifetime fit method relies on the correct extraction of the efficiency curve. This include also a correct parameterization of the efficiency distribution in Eq. 5.5. In the analysis the parameterization proposed in Eq. 5.6, that has the advantage of being analytically integrable, is used. Those parameters are fixed using Monte Carlo data by performing a binned likelihood fit and therefore have associated errors. The uncertainty

[1] In this case we do not rescaled the same sample.

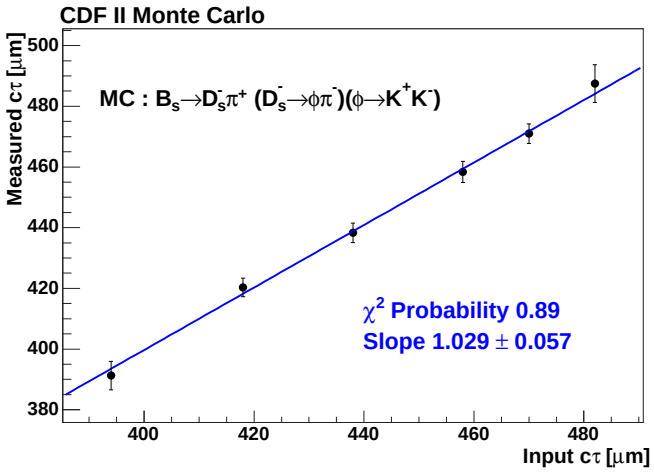

Figure 7.2: *The Plot shows the measured $c\tau$ as a function of input lifetime used to work out the efficiency function. The measured value of $c\tau$ is independent of input lifetime.*

on the efficiency parameters translates in a lifetime systematic error that have to be evaluated. The ideal way to evaluate the bias introduced by the parameterization, would be varying the parameters within their errors to obtain new curves and compare the new lifetime results obtained with them. Unfortunately these parameters are strongly correlated and this procedure would easily lead to an overestimation of the effect. Instead we decided to completely change the functional form to describe the efficiency curve using Eq. 5.7 .
The involved integrals implied by these very generic parametrization are solved numerically.
Therefore data are fitted for the lifetime using this new parametrization of the efficiency distribution. The lifetime value obtained with the new efficiency curve for the $B_d^0 \to D^-\pi^+$ is 458.1 ± 7.6 resulting in a lifetime shift of 1.5 μm which is taken as systematic error due to the parametrization model.

7.5 $\Delta\Gamma_s$ dependence

The width difference between the two CP eigenstates in the B_s^0 mesons is predicted by lattice QCD calculation (in the Standard Model frame) to be sizable: $\Delta\Gamma_s/\Gamma_s \sim 0.12 \pm 0.06$. The $B_s^0 \to D_s^-\pi^+$ decay mode contains an equal mixture of the two CP eigenstates. Hence, a measurement of the lifetime gives an estimation of the average value $< \tau >$. If $\Delta\Gamma_s/\Gamma_s$ is large, the two B_s^0 CP eigenstates will have significant different lifetimes, therefore the trigger selection can sculpt in different way the proper time distribution of the CP eigenstates and change the mixture between the two states in the reconstructed sample, resulting in a overall shift in the determination of the average lifetime $< \tau_{B_s} >$. The systematics coming from the uncertainty on $\Delta\Gamma_s/\Gamma_s$ is taken into account in this Section.

Two signal Monte Carlo samples with $c\tau + 10\%$ and $c\tau - 10\%$ (i.e. $c\tau = 482$ μm and $c\tau = 394$ μm) are generated and then combined together to extract the efficiency distribution. The combined sample after trigger and analysis requirements is a mixture in the percentage of 51.8% and 48.2% of the initial samples. The trigger and analysis selections, indeed, slightly change the 50-50% initial mixture favouring the long lived component, as expected.
From this mixed Monte Carlo sample a new efficiency curve is extracted and used to fit for the lifetime a Signal Monte Carlo sample. The obtained result is 437.3 μm compared to 438.3 μm quoted in Table 5.1. The difference had been used as an estimation of systematic effect due to this dependence.

7.6 Scaling factor dependence

In the analyses all the fits use a fixed value for the proper time scale factor. The value used in the analysis come from evaluation performed in other samples selected with a different trigger, so is it straightforward to check any bias due to the use of an improper scale factor. Therefore the scale factor is varied in the lifetime fits of $\pm 5\%$ of the standard value [72], which is the uncertainty affecting the determination of this parameter from the CDF analysis. In all cases variations less then 0.1 μm are found in the lifetime fit result, so that this dependence has been considered negligible. This fact is not surprising: with the silicon detector CDF reaches proper time resolution around 50 μm, so that measurements of the B lifetime, that are of the order of 500 μm, cannot be heavily affected by mis-resolution, and clearly a wrong resolution estimation is expected to introduce negligible effects in our lifetime measurements.

7.7 SVX Alignment

B vertices positions result from a tridimensional fit on the tracks in the final state. The silicon hits assigned to the tracks provide the most accurate measurement of the spatial coordinates, and therefore play an important role in the vertices reconstruction. Hit position is known to about 10 μm relative to the individual wafer which registers the hit. Then, the knowledge of the position of the wafer can be summarized in the following items:

- $\surd$ Position of the wafer in the ladder,
- $\surd$ Position of the ladder within the SVX barrel,
- $\surd$ Position of the barrel w.r.t. the other barrels,
- $\surd$ Position of the SVX in the global (COT) reference frame.

All these informations are stored in the alignment database and are continuously updated during data taking. Detailed studies [79] have been done to understand the effect of poor knowledge of wafer position (also called mis-alignment); here an overview of the method used and the resulting uncertainty associated is presented.

The mis-alignment uncertainty is not uniquely related to a specified analysis, in fact it is only related to the detector configuration during data taking and to the tracking algorithm used. Therefore, the results obtained, also in different trigger samples, can be used as an estimation for all analyses deeply involved in the lifetime measurements.
The studies related to the mis-alignment, were focused on two effects: the ladder bowing and an evaluation of the general alignment quality.
When two ends of a ladder are pinned to the SVX II frame, it has been observed that the ladder in most cases bends outward, so that two central wafers are at radius larger than nominal. Only in very few cases the ladders bow inward. The radial shift (of central wafers) is on average about 70 μm, but for some ladders the shift has been found to be 200 μm. The bowing effect is believed to be taken out on the most part by the alignment procedure, but we tested a somewhat marginal case of the bowing effect on the lifetime measurement in the following way:

① A wrong version of the alignment was created. In that version all SVX ladders are "bowed" inward (outward) by 50 μm.

② Starting form the previous alignment another alignment version was created where all 4 wafers in each ladder are move in (out) by 50 μm.

③ The lifetime analysis was repeated with each of such modified alignments.

The results on data and MC show that the lifetime variations are purely statistical and bow effect does not have a significant impact on the lifetime.
To check the overall quality of the alignment tables we proceed as follow: the lifetime extracted using the most recent and up-to-date alignments table is compared to the lifetime extracted using older versions of the alignment. The results of these studies show that most of the difference between the lifetimes extracted are absorbed in the error scale factor on proper time, which is, in certain sense, the scale for the proper decay length resolution.
Considering both the "bow" effect as well as the differences among different versions of alignment an global error of ± 2.4 μm was assigned as systematic uncertainty due to the alignment imperfections.

7.8 Systematic Uncertainties: Results

In this Section the results of all the systematic uncertainties are summarized. In Table 7.7 a summary of all systematic sources evaluated is given for the three mesons studied. The last line quotes the sum in quadrature of all contributions. This as been done because the contributions are supposed to be uncorrelated.
For the neutral mesons we performed two statistically independent measurements in different decay modes, each of them is affected by the same systematic error. While some of them are uncorrelated between the two decay modes, others are instead completely correlated and have to be counted once when we extract the global uncertainty. This is the case of the Alignment and I.P. correlation systematic errors for both the neutral mesons, and of the $\Delta\Gamma_s$ systematic uncertainty for the B_s^0 only. Therefore we used the formula in

Effect	Systematic Error (μm)				
Meson	B_d^0		B_s^0		B^+
Decay Mode	$D^-\pi^+$	$D^-\pi^+\pi^-\pi^+$	$D_s^-\pi^+$	$D_s^-\pi^+\pi^-\pi^+$	$\bar{D}^0\pi^+$
MC input $c\tau$	negligible	negligible	negligible	negligible	negligible
p_T re weight	1.9	1.9	1.9	1.9	1.9
Scale Factor	negligible	negligible	negligible	negligible	negligible
Bkg ct description	1.1	-	-	1.1	1.1
Part. Reco. B	negligible	negligible	10	negligible	1.5
Bkg fraction	2.0	2.0	2.0	2.0	2.0
I.P. correlation	1.0	1.0	1.0	1.0	1.0
Eff. param.	1.5	1.5	1.5	1.5	1.5
$\Delta\Gamma_s$	-	-	1.0	1.0	-
Alignm. + others	2.4	2.4	2.4	2.4	2.4
Total	4.2	4.1	11.0	4.3	4.5

Table 7.7: *Different contribution for the systematic uncertainties for B_d^0 , $B^\pm$ and B_s^0.*

Eq. 6.11 to extract the systematic errors for the B_d^0 and the B_s^0 mesons considering that only the $D+$ single track modes are affected by the Alignment, I.P. correlation and $\Delta\Gamma_s$ systematic uncertainties.
Hence, the final lifetime determination for the three mesons is:

$$\begin{aligned} c\tau(B_d^0) &= 453 \pm 7\,(stat) \pm 3\,(syst)\ \mu m, \\ c\tau(B_s^0) &= 479 \pm 29\,(stat) \pm 11\,(syst)\ \mu m, \\ c\tau(B^\pm) &= 498 \pm 8\,(stat) \pm 4\,(syst)\ \mu m. \end{aligned}$$

or

$$\begin{aligned} \tau(B_d^0) &= 1.510 \pm 0.022\,(stat) \pm 0.011\,(syst)\ ps, \\ \tau(B_s^0) &= 1.599 \pm 0.096\,(stat) \pm 0.036\,(syst)\ ps, \\ \tau(B^\pm) &= 1.661 \pm 0.028\,(stat) \pm\ 0.015(syst)\ ps. \end{aligned}$$

It is worth to notice that the B_s^0 lifetime evaluation is best single measurement available and the first measurement using fully reconstructed exclusive decay modes.

7.9 Conclusions and Perspectives

In this analysis B_u, B_d and B_s mesons were reconstructed in hadronic exclusive decay modes and lifetime values were extracted using combined mass-lifetime unbinned maximum likelihood fits. The high statistics of the samples used and the method developed gave the possibility to quote high precision results affected by low systematics uncertainty (see Figures 7.3 and 7.4).

This analysis has been performed using roughly 360 pb^{-1} of data collected at CDF II

Lifetime ratio	HQE Prediction	This Analysis
$\frac{\tau(B^+)}{\tau(B^0_d)}$	1.06 ± 0.02	1.100 ± 0.026
$\frac{\tau(B_s)}{\tau(B^0_d)}$	1.00 ± 0.01	1.059 ± 0.070

Table 7.8: *HQE prediction for the B mesons ratio. The results of this analysis are also reported in the last column.*

with the dedicated Two Track Trigger. Nowadays CDF II has collected 1 fb^{-1} of data, more over in the beginnings of 2005, the Recycler Ring started to work increasing in a significant way the instantaneous luminosity. In addition the Two Track Trigger allows to reconstructed several hadronic decay modes using, for example, different decay modes of the associated charmed meson, further reducing the statistical uncertainty. Therefore, in the next years huge samples of hadronic decaying B mesons will be available to improve the quoted results. In fact, the quoted lifetimes are still affected by a statistical error that is 2 times bigger than the systematic uncertainty, then lifetime determinations for the B^0_d and the $B^\pm$ mesons can be brought under the % level just using the new collected data. Again, in the lifetimes measurements performed, some systematics errors cancel out when quoting the ratio:

$$\frac{\tau(B^\pm)}{\tau(B^0_d)} = 1.100 \pm 0.024\ (stat.) \pm 0.009\ (syst.)$$
$$\frac{\tau(B^0_s)}{\tau(B^0_d)} = 1.059 \pm 0.066\ (stat.) \pm 0.023\ (syst.)$$

Thus, as shown in Table 7.8, the measurement obtained in this analysis for $B^\pm/B^0_d$ lifetime ratio is at the same precision level of the theoretical predictions.
The B^0_s lifetime measurement is affected by greater uncertainties in both statistical and systematic sectors, but is, anyway, one of the best single measurement available. Also for this meson the increasing statistic that will be collected at CDF II and the new B^0_s decay modes reconstructed, will reduce in a significant way the statistical uncertainties associated. The systematic error, that is at the respectable value of ∼2%, can be brought under the per cent level as for the others reconstructed B. In Appendix B, the main source of systematic error for the B^0_s is discussed, and a method to reduce it of a facotr 10 is proposed and validated.
Therefore, thanks to the new lifetime measurements that the CDF II will do with the increased statistic, it will be possible to probe the HQE predictions at deeper levels and look for *New Physics* hints.

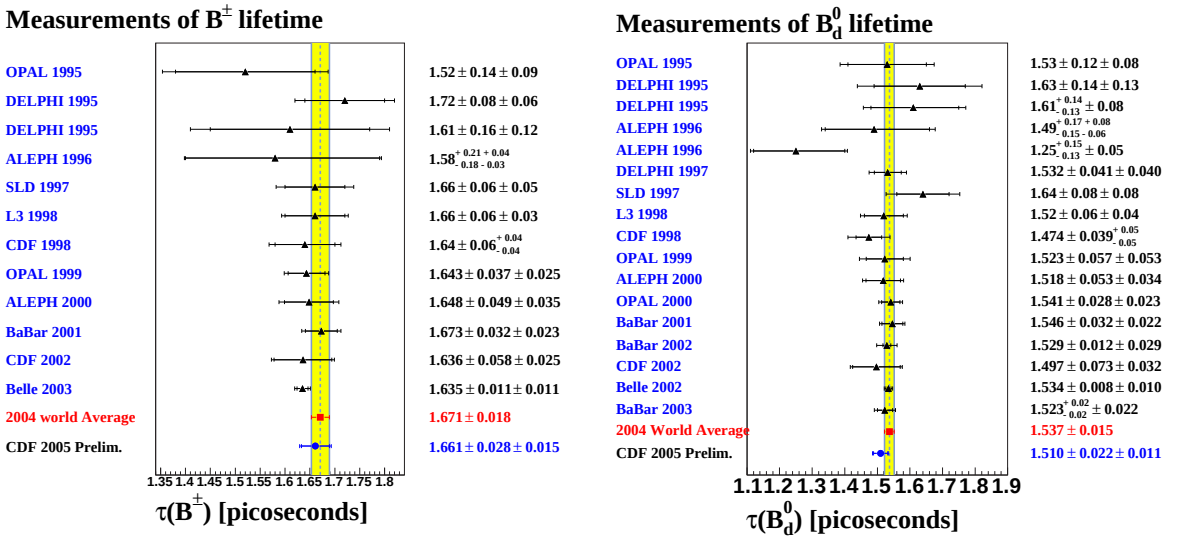

(a) (b)

Figure 7.3: *Summary of existing lifetime measurements for B_d^0 (a) and $B^{\pm}$ (b). In the last row, the values obtained in this analysis are reported.*

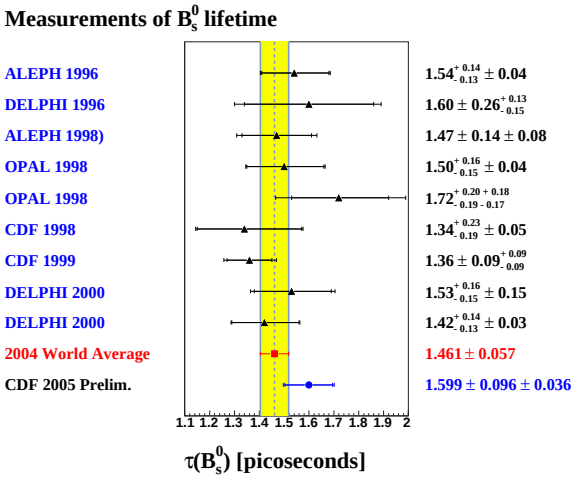

Figure 7.4: *Summary of existing lifetime measurements for B_s^0. In the last row, the value obtained in this analysis is reported.*

Appendix A

Likelihood Fit Details

A.1 Mass templates *p.d.f.*

In Chapter 6 the general *p.d.f.* used to perform the unbinned mass likelihood fit was presented. Anyway different decay modes needed different background models for the low mass structure, and the individual functional forms were not presented. Here, we will present the analytical definition of the templates used.
For each decay mode an exhaustive determination of the functional form will be presented.

A.1.1 $B^+ \to \bar{D}^0\pi^+$ Mass templates

As mentioned in Chapter 6, the background contribution coming from partially reconstructed B can be summarized in two main contributions: The $D^\star$ and the continuum. The former takes into account for the decay modes where a $D^\star$, coming from a B, decays into a D^0 meson. The second one is intended to represent all other contributions.
The following decay modes contribute to the $D^\star$ background:

- $B^+ \to \bar{D}^{0\star}\pi^+(K^+)$
- $B^0_d \to D^{\star-}\pi^+(K^+)$

Here, $\bar{D}^{0\star}$ is the $\bar{D}^\star(2007)^0$ excited state, decaying in the modes $D^0\pi^0$ and $D^0\gamma$ that are reconstructed loosing the neutral pion or the photon. The polarized $D^\star$, decaying into the $D^0\gamma$ mode, generates a double peak structure, because the photon helicity, while the $D^0\pi^0$ decay mode is responsible for a wide peak under the horns, creating the structure visible in Fig. 6.1 and 6.3 (a),(b),(d).
Is then clear that a triple Gaussian can describe all the stuff. More over, not all parameters are free, but correlation can be easily found between the three Gaussians. Finally the

following functional form has been used for the $D^\star$ contribution:

$$\begin{aligned} p.d.f.^{D^\star}(m) &= \frac{1-f_1}{\sqrt{2\pi}\sigma_1} e^{-\frac{(m-\mu_1)^2}{2\sigma_1^2}} \\ &+ \frac{0.5\cdot f_1}{\sqrt{2\pi}\sigma_2} e^{-\frac{(m-(\mu_1-\mu_2))^2}{2\sigma_2^2}} \\ &+ \frac{0.5\cdot f_1}{\sqrt{2\pi}\sigma_2} e^{-\frac{(m-(\mu_1+\mu_2))^2}{2\sigma_2^2}} . \end{aligned} \tag{A.1}$$

Here the f_1 is the relative contribution between $D^0\pi^0$ and $D^0\gamma$ modes of the $D^\star$ meson, μ_1 is the mean of the central Gaussian, μ_2 is the offset of the secondary peaks from the meaning one, and finally σ_1 and σ_2 are the widths of the Gaussians.
The continuum contribution is intended to describe all other partially reconstructed Bs without any dominant contribution. All the B mesons having a D^0 and at least one track in the final state (excluding the $D^{0\star}$ modes) are included. The functional form is therefore suggested by the MC distribution. The experimental functional form that better describes this contribution has been found to be:

$$p.d.f.(m)^{B^\pm_{cont}} = \left(1.0 - \left(m - \frac{\mu_{up}-\mu_{down}}{2}\right)\cdot s_{cont.}\right)\cdot\left(1.0 - e^{(m-\alpha)\cdot\tau_m}\right). \tag{A.2}$$

Here μ_{up}, μ_{down} are the upper and lower limit of the mass window fit, α is the endpoint value, i.e. where the function touch the zero value, and $s_{cont.}$ and τ_m are the slope and the lifetime variables, respectively.

A.1.2 $B^0_d \to D^-\pi^+$ Mass templates

The B^0_d survey is similar with respect to the B^+ one. Here more then one dominant contribution is separated, therefore the parametrization used reflect this schema. We can summarize all the contributions in : $D^\star$, $D^-\rho^+$ and continuum. Also contaminations are present in the signal region coming from $B^0_s \to D^-_s\pi^+$ and $\Lambda_b \to \Lambda^+_c\pi^-(\Lambda^-_c \to \bar{p}K^+\pi^-)$ decay modes.
The $D^\star$ contribution comes from B^0_d decaying into $D^{\star-}\pi^+$. In that case, the excited D state is the $D^\star(2010)^-$ contributing with the decay modes $D^-\pi^0$ and $D^-\gamma$. Also for this contribution, hold the motivations explained for the B^+, so that the same parametrization in Eq. A.1 was used for B^0_d.
The $D^-\rho^+$ is a dominant contribution not separated in the B^+ case. Here while the charmed meson is correctly reconstructed, the charged ρ meson is only partially reconstructed. The dominant decay mode ($\sim 100\%$) for the $\rho^\pm$, in one charged and one neutral pion, generates a main wide peak that has a big negative queue due to the kinematics. Here only the charged pion is detected, and the energy carried by the neutral one generates the shoulder behavior. So we found that an inverted exponential convolved with a Gaussian well represents the sample:

$$p.d.f.(m)^{D\rho} = e^{a\cdot(m-\mu_\rho)}\cdot Erfc(b\cdot(m-\mu_\rho)). \tag{A.3}$$

Where a, b, μ_ρ are just three parameters related to the mean, the width and the lifetime of the inverted exponential convolved with a Gaussian, and the $Erfc$ is the so called *complementary Error Function* defined as:

$$\begin{aligned} Erfc(x) &= (1 - Erf(x)) \\ Erf(x) &= \int_0^x \frac{1}{\sqrt{2\pi}\sigma} e^{-\frac{(t-\mu)^2}{2\sigma^2}} dt, \qquad (\mu = 0, \sigma = 1). \end{aligned} \tag{A.4}$$

Finally the continuum contribution, considering all other contributions, was parametrized with a straight line:

$$p.d.f.(m)^{B^0_{cont}} = 2.0 \cdot \frac{(\gamma - m)}{\eta^2}. \qquad (\gamma, \eta \geq 0) \tag{A.5}$$

The Λ_b and B_s contributions have been templated fitting dedicated Monte Carlo simulations after the reconstruction procedure used for the B^0_d golden mode. Both the contributions were templated using a Bifurcated Gaussian, defined as:

$$\mathcal{L}_{Bif} = e^{-\frac{(m-\mu_{bif.})^2}{2\sigma_L^2}} \cdot (m > \mu_{bif.}) + e^{-\frac{(m-\mu_{bif.})^2}{2\sigma_R^2}} \cdot (m \leq \mu_{bif.}) \tag{A.6}$$

A.1.3 $B^0_d \to D^-\pi^+\pi^-\pi^+$ Mass templates

In this multi-bodies decay mode, we considered just one contribution as dominant with respect to the others. In fact, even if one could expect that the other modes contribute in a significant way, nonetheless is not convenient to create a lot of templates, mainly because the high level of the combinatorial background makes the fit not very sensitive to the physics background parametrization. Therefore, in practice, we decide to hold the usual parametrization for the $D^\star$ mode (Eq.A.1) and create an *ad hoc* template for the other contributions. The *p.d.f.* used to template this background is the sum of three functions, a positive exponential convoluted with a Gaussian, a negative exponential convoluted with a Gaussian, and a straight line:

$$\begin{aligned} p.d.f.(m)^{B^0_d rest.} &= (1 - 2 \cdot f_{rest.}) \cdot \frac{1}{2} e^{\frac{\sigma^2_{rest.} - 2(m-\mu_{rest.})\tau_{rest.}}{2\tau^2_{rest.}}} \cdot Erfc\left(\frac{\sigma^2_{rest.} - (m - \mu_{rest.})\tau_{rest.}}{\sqrt{2}\sigma_{rest.}\tau_{rest.}}\right) \\ &+ f_{rest.} \cdot 2.0 \cdot \frac{(\gamma - m)}{\eta^2} \\ &+ f_{rest.} \cdot e^{a_{rest.} \cdot (m - \mu_\rho)} \cdot Erfc(b_{rest.} \cdot (m - \mu_\rho)) \end{aligned} \tag{A.7}$$

The three contributions have been normalized to unity within the fit range.

A.1.4 $B^0_s \to D^-_s\pi^+$ Mass templates

The physics background for B^0_s is expected to be similar to the B^0_d one. Anyway, the lack of statistic in the strange meson bring us to choose a less detailed parametrization. As for B^0_d, in the $D+$ single track mode the background contribution can be divided into three sources: $D^\star$, $D^-\rho$ and continuum. In this case, the $D^\star$ contribution is not enough

populated to distinguish the typical double peak. Because that, we choose to merge this contribution with the $D\rho$ and fitting all the stuff with a Gaussian plus a negative exponential convoluted with a Gaussian:

$$p.d.f.(m)^{B_s^0 D^\star} = (1 - f_\rho)\frac{1}{\sqrt{2\pi}\sigma_\star} e^{-\frac{(m-\mu_1)^2}{2\sigma_\star^2}} + f_\rho \cdot e^{a\cdot(m-\mu_1)} \cdot Erfc(b \cdot (m - \mu_1)). \quad \text{(A.8)}$$

The continuum distribution does not need a complicated parametrization. A straight line, as in Eq.: A.5, followed the purpose.

A.1.5 $B_s^0 \to D_s^- \pi^+ \pi^- \pi^+$ Mass templates

As for the golden B_s^0 mode the parametrization used for this $D+$ three tracks mode comes from the same B_d^0 decay mode. Thus, also for this channel the physics background was parametrized distinguishing the $D^\star$ contribution, templated with an inverse error function, as in Eq.: A.3, and the *continuum* contribution, templated with the same functional form used for the $B_d^0 \to D^- \pi^+ \pi^- \pi^+$ mode and presented in Eq. A.7.

Appendix B

Further Studies on Systematic optimization

B.1 B_s^0 Physics Background Description

As noted in Chapter 7, a first evaluation of the systematic error due to the partially reconstructed B in the fitting region, returns, for the B_s^0,], a large value that is not in agreement with the evaluation of the same effect in the other decay modes. At that time, it was noticed that for this particular measurement, the systematic deviation is indeed smaller than the statistic error, and has been assumed as a *conservative* estimation.
Clearly, when the statistics will increase, this systematic could became a problem, because it is the main contribution and seems to be related to the method itself. Therefore, an effort is needed to understand if the evaluation proposed in Chapter 7 can be improved.
This Appendix is devoted to find a better estimation of the systematic error due to the partially reconstructed contamination in the fitting mass region.

B.1.1 Mass Parametrization

Table 7.1 shows, for each decay mode reconstructed, the systematic error associated and the estimation of the contamination from the partially reconstructed B with respect to the overall background in the fitting mass region. In the same table, a contribution around 3% for the $B_s^0 \to D_s^- \pi^+$ decay mode is quoted. This huge contribution seems to be too high if one compares this number with the ones obtained for the B_d^0. In fact, looking at the Mass distribution in Fig. 6.8 (a), it can be seen that the $D^\star$ template continues also after the centroid of the signal peak, that is an unphysical behavior, meaning that the template used to describe such a contribution is not straigthforward and have to be corrected.
The first plot in Fig. 6.2 (c) shows the *controversial* template. Here a single Gaussian is used to template the $D_s^\star$ modes, together with an inverse exponential convolved with a Gaussian to take into account for the $D_s\rho$ contribution. The use of a single Gaussian was justified by the lack of statistic, which is so poor on data to highlight the expected *double-horns* structure already observed in the B_d^0 and $B^\pm$ decay modes. From a theoretical point

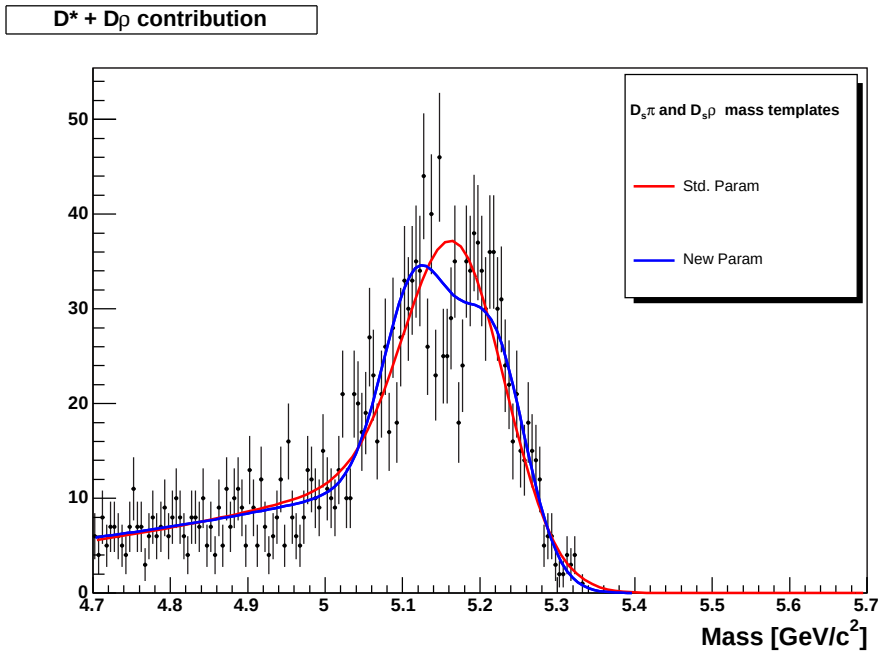

Figure B.1: *Invariant mass distribution for the $D_s^{\star -}\pi^+$ $D_s^-\rho^+$ contribution in the B_s^0 golden mode. The blue curve represents the new parametrization while the red one represents the standard one.*

of view, the double-horns structure is supposed to appear in the B_s^0 mode also; indeed the Monte Carlo simulations used for the templates, seem to present this behavior. Therefore, a new template for the $D_s^\star$ contaminations is created using the triple Gaussian model as described by the Eq. A.1. In Practice, the $p.d.f.$ used for the new parametrization comes from the one presented in Eq. A.8 where the first term is substituted with the term in Eq. A.1, that is :

$$\begin{aligned} p.d.f.(m)^{B_s^0 D^\star} &= (1-f_\rho)\cdot\left(\frac{1-f_1}{\sqrt{2\pi}\sigma_1}e^{-\frac{(m-\mu_1)^2}{2\sigma_1^2}} + \frac{0.5\cdot f_1}{\sqrt{2\pi}\sigma_2}e^{-\frac{(m-(\mu_1-\mu_2))^2}{2\sigma_2^2}}\right. \\ &+ \left.\frac{0.5\cdot f_1}{\sqrt{2\pi}\sigma_2}e^{-\frac{(m-(\mu_1+\mu_2))^2}{2\sigma_2^2}}\right) + f_\rho\cdot e^{a\cdot(m-\mu_1)}\cdot Erfc(b\cdot(m-\mu_1)). \end{aligned} \tag{B.1}$$

A Binned likelihood fit performed on the inclusive Monte Carlo sample, returns a $\chi^2/n.d.f$ =137/117 and a χ^2 probability of 10%. As done for the previous parametrization the $D_s^\star$ and $D_s\rho$ contributions were fitted simultaneously.
Fig. B.1 shows the projections of the fitted curve on the inclusive Monte Carlo sample: both the new and the standard parametrization curves are shown.

The new parametrization presents a better behavior in the high mass region, avoiding to continue in the unphysical region as done by the other parametrization. in practice the double-horns structure allows for a better description of the fall down shape near the end-up region.

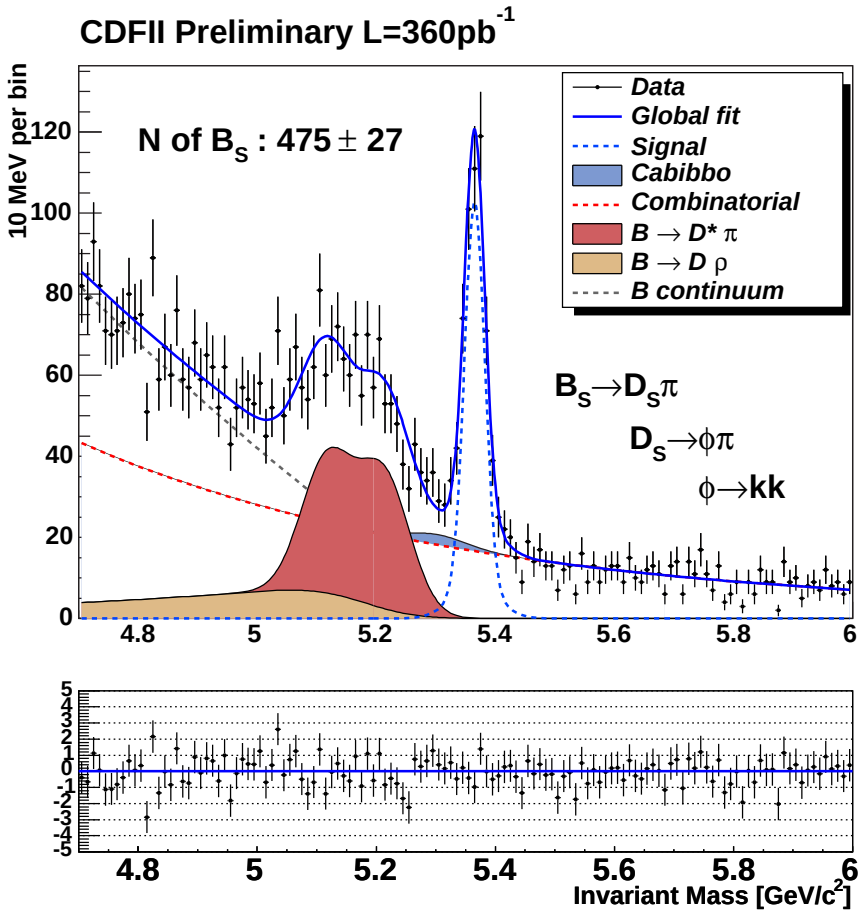

Figure B.2: *Invariant mass distribution for the $B_s^0 \to D_s^- \pi^+$ with the fit curves superimposed. Different background contributions are also shown. New template for the $D_s^\star$ contribution has been used.*

Hence, with this new template the unbinned maximum likelihood fit has been performed on data, in the wide mass region. Figure B.2 shows the mass distribution with the new fit curves superimposed; different background contributions are also shown. In Table B.1 the fit results are reported together with the estimation obtained form the fit performed with the standard template and already reported in Table 6.6. The comparison between the two fit, does not present any deviation in the signal parameters: signal fraction, mean and width of the main Gaussian are essentially the same in both fits. The new parametrization slightly modify the relative contribution between the $D_s^\star$ and $D_s\rho$ contamination (parameter f_ρ), changing the shape of the last one template, and the slope of combinatorial distribution. The most important thing is that, re-scaling the parameters to the lifetime fitting region the contamination from the partially reconstructed of is found to be around 0.5%, more than 6 times smaller than the fraction predicted by the standard template.

B.1.2 Combined Fit

Finally, using the mass window [5.32 - 5.72] GeV/c^2, the combined mass and lifetime unbinned maximum likelihood fit with per event error is performed. For the combinatorial background in the proper time sector the same template generated in Chapter 6 is used, and the Scale Factor was fixed to the 1.3 value; the efficiency curve used is the one derived for the standard fit. Again, the two lifetime parameters of the combinatorial background were left to be free during the fit. In Fig. B.3 the mass and proper time distributions are shown with the fitted curves superimposed, while in Table B.2 the fit results are returned together with the same results obtained with the standard fit.

Parameter	New Fit	Std. Fit	Units
Horn Frac. (f_1)	0.971 FIXED	———	
Horn center (μ_1)	5,165.5 FIXED	———	MeV/c^2
Horn offset (μ_2)	48.76 FIXED	———	MeV/c^2
Horn Main σ (σ_1)	44.16 FIXED	———	MeV/c^2
Horn sec. σ (σ_2)	43.15 FIXED	———	MeV/c^2
Mis reco rel. ratio ($f_{D^\star}$)	0.36 ± 0.02	0.37 ± 0.03	
D_ρ a (a)	1.818 FIXED	1.189 FIXED	$GeV^{-1}c^2$
D_ρ b (b)	10.18 FIXED	32.19 FIXED	$GeV^{-1}c^2$
Refl. σ ($\sigma_\star$)	———	75.6 FIXED	MeV/c^2
Refl. *mean* (μ_1)	5,165.5 FIXED	5,165.4 ± 4.9	MeV/c^2
Rel. ratio (f_ρ)	0.13 FIXED	0.15 FIXED	
point continuum (γ)	5.17 FIXED	5.17 FIXED	GeV/c^2
comb. ratio ($f_{comb.}$)	0.52 ± 0.05	0.52 ± 0.05	
comb. slope (s)	1.52 ± 0.11	1.32 ± 0.13	$MeV^{-1}c^2$
comb. flat(f_{flat})	0.07 ± 0.01	0.07 ± 0.01	
signal fraction (f_S)	0.102 ± 0.006	0.101 ± 0.006	
B_s^0 mean	5,365.2 ±1.1	5,365.6 ± 1.1	MeV/c^2
B_s^0 width	16.7 ± 1.1	16.6 ± 1.1	MeV/c^2

Table B.1: *Mass Fit results in the wide mass window for $B_s^0 \to D_s^- \pi^+$ with the new $D_s^\star$ template. The results from the standard fit are also reported for comparison.*

In this Table it can be seen that while the mass parameters does not move changing the fitter configuration, the B_s^0 lifetime goes down of 4 μm and the combinatorial lifetimes slightly increase. This kind of behavior was indeed expected: now that the partially reconstructed B contamination is reduced below the 0.5%, some events are redistributed between the signal and the combinatorial background. The shift on the B_s^0 lifetime is compatible with the 10 μm estimated as the systematic error due to these guilty events. To check the consistency of the result a new estimation of the Partially Reconstructed B systematic uncertainty is performed using the same method already exposed in Chapter 7. Now the shift of 1 μm is measured, confirming the validity of our approach.

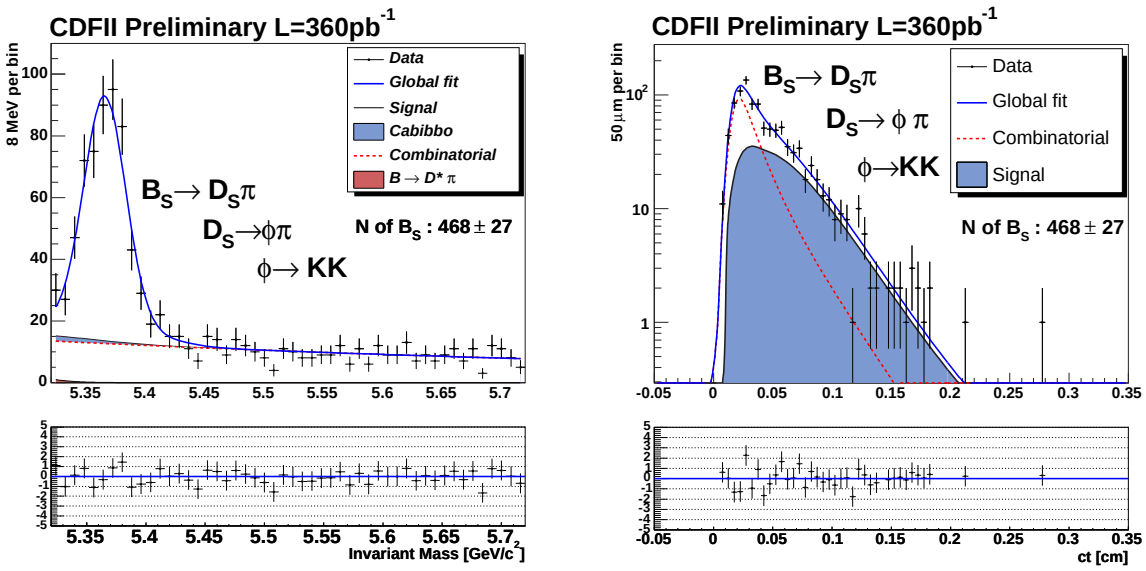

Figure B.3: *Fit projections for $B_s^0 \to D_s^- \pi^+$ decay mode with the fit results superimposed. (a) Mass distribution, (b) proper time distribution.*

B.1.3 Conclusions

A detailed analysis on the mass parametrization shown that the main source of systematic error in the $B_s^0 \to D_s^- \pi^+$ decay mode, is due to an incorrect mass template shape for the partially reconstructed B. Using a more reliable parametrization turned in a better description of the contamination in the mass fitting region, allowing to reduce the systematic uncertainty due to this effect by a factor of 10. The use of the new parametrization move the central value of our B_s^0 lifetime to 4 μm. Indeed this shift is compatible with the new description and the previous associated systematic error. Reducing this systematic uncertainty allows to extend this method to high statistic samples also, when they will be available at CDF II in the next years.
Using the new procedure, quoting the new systematic due to the partially reconstructed B, and averaging this result with the D+three tracks modes, our final estimation for the

Parameter	New Fit	Std. Fit	unit
B_s mass	5,365.2 ± 1.1	5365.2 ± 1.1	MeV/c^2
B_s width	18.06 ± 1.1	17.83 ± 1.1	MeV/c^2
B_s lifetime	475 ± 31	479 ± 32	μm
τ_1	121 ± 18	113 ± 31	μm
τ_2	251 ± 23	214 ± 16	μm

Table B.2: *Lifetime fit results for the new template. The results from the fit described in Chapter 7 are reported also.*

average B_s^0 lifetime will be:

$$c\tau(B_s^0) \;=\; 478 \pm 27\,(stat) \pm 3\,(syst)\ \mu m,$$

or, equivalently

$$\tau(B_s^0) \;=\; 1.596 \pm 0.091\,(stat) \pm 0.009\,(syst)\ ps,$$

Acknowledgments

I would like to thank Prof. Giovanni Busetto and Prof. Dario Bisello for the opportunity of doing my Ph.D. studies in such an experiment as CDF II.
I need to thank all the members of the CDF group at Padova University. First of all Donatella, she was *always* a point of reference during my experience in the b physics; sharing the same office for three years made my Ph.D. experience a *funny* job. Then I would to thank Tommaso, Julien and Luca, their friendship has been important to make my work easy. I have not to forget Francesco (*a.k.a. Delli*), his thunder-storming presence was a beautiful help to understand the secrets of the *Computing World*.
A special thank to Giorgio. We were *brothers* throughout this experience and I hope that our friendship doesn't stop to grow after we will be kept by the *Real World*.
I would like also to thank Stefano Giagu for his support during the *run toward the blesses*. He was as a second advisor in my Fermilab winter.
I am very grateful to Kim Giolo and Mauro Donegà, with whom I shared the challenge of the lifetime business. I always remember the dinners *"chez Kim"* before to face the hard work nights...
I need to thank the *train friends* also. I would not be able to face the daily delays without you guys!
I would like to thank my family for its support during these years, they believe on me in the difficult moments and understood the choices I did.
Finally a big kiss to my girlfriend Alessia; thanks to have been so strong when I was far away, thanks to have been so patient when my mind was blind because the job. Your balance helped me to understand what is important in life.

List of Figures

List of Tables

Bibliography

[1] F. Mandll and G. Shaw , Quantun Field Theory, REVISED EDITION,*John Wiley & Sons*, (1999).

[2] L.Wolfenstein, *Phys. Rev. Lett.* **51** (1983) 1945.

[3] I. Bigi, The QCD perspective on lifetimes of heavy-flavour hadrons, *UND-HEP-95-BIG02* (1995).

[4] N. Uraltsev, Heavy Quark Expansion in beauty and its decays, *UND-HEP-98-BIG1* (1998).

[5] K. Wilson, Non-Lagrangian models of current algebra, *Phys. Rev.* **179** 1499-1512 (1969).

[6] J.D. Richman., Heavy Quark Physics and CP Violation. *Elsevier Science B.V.*, (1998)

[7] J.-M. Gerard and W.-S. Hou, *Phys. Rev.* D **43**, 2909 (1991).

[8] The Heavy Flavor Averaging Group (HFAG), Averages of b-hadron Properties as of Winter 2005, *hep-ex/0505100*

[9] The Heavy Flavor Averaging Group (HFAG), Averages of b-hadron Properties as of Summer 2005,
`http://www.slac.stanford.edu/xorg/hfag/triangle/summer2005/index.html`

[10] B. Aubert *et all.*, (`BaBar` Collaboration), *Phys. Rev. Lett.* **92**, 181801 (2004)

[11] J. Adballah *et all.*, (`DELPHI` Collaboration), *Eur. Phys. J.* C **28**, 115 (2003)

[12] J. Adballah *et all.*, (`DELPHI` Collaboration), *Eur. Phys. J.* C **33**, 307 (2004)

[13] F. Gabbiani, A. I. Onishchenko and A.A. Petrov, *Phys. Rev.* **D 70** 094031 (2004)

[14] H.-G. Moser and Roussarie, *Nucl. Instrum. Methods A* **384**,491 (1997)

[15] Fermilab Beams Division,
`http://www-ad.fnal.gov/runII/index.html` .

[16] Fermilab Beams Division, Fermilab Linac Upgrade. Conceptual Design, *FERMILAB-LU-Conceptual Design*,
`http://www-lib.fnal.gov/archive/linac/fermilab-lu-conceptualdesign.shtml`.

[17] Fermilab Beams Division, The antiproton source rookie book, http://www-bdnew.fnal.gov/pbar/documents/PBAR_Rookie_Book.pdf.

[18] Fermilab Beams Division, The Recycler ring, http://www-recycler.fnal.gov/recycler_main.html.

[19] F. Abe *et al.*(The CDF II Collaboration), "The CDF II Technical Design Report", *FERMILAB-PUB-96-390-E*, Oct 1996.

[20] S. M. Sze, Physics of Semiconductor Devices, SECOND EDITION, *John Wiley & Sons*

[21] The CDF II Collaboration, Proposal for Enhancement of the CDF II Detector: An Inner Silicon Layer and A Time of Flight Detector, *Fermilab-Proposal-909*, Oct. 1998.
Update to Proposal P-909: Physics performance of CDF II with an Inner Silicon Layer and a Time of Flight detector, http://www-cdf.fnal.gov/upgrades/btb-update_jan99.ps,(1999).

[22] J. Marriner, Secondary vertex fit with mass and pointing constrains (CTVMFT), **CDF** Note 1996, (1993).

[23] W.-M. Yao, and K. Bloom, "Outside-In" silicon Tracking at CDF, **CDF** Note 5562, (2002).

[24] P.Azzi, G. Busetto, A. Ribon, Histogram tracking in the COT, **CDF** Note 5562, (2001).

[25] H. Frisch *et. all.*, Conceptual design of a deadtimeless trigger for the CDF trigger upgrade, **CDF** Note 2038, (1994).

[26] The CDF II Collaboration, CDF Run II trigger table and datasets plan, **CDF** Note 4718, (2001).

[27] E. Thomson *et. al.*, Online track processor for the CDF Upgrade, *IEEE Transactions on Nuclear Science*, Vol. 49, No. 3,(2002)

[28] A. Bardi, S. Belforte, *et all.*, "SVT: An Online Silicon Vertec Tracker for the CDF upgrade", *Nucl. Instr. Meth.*, Vol. A **409**,658-661, 1998

[29] W. Ashmanskas, A. Bardi, *et all.*, " The CFD Silicon Vertex Tracker: online precision tracking of the CDF Silico Vertex Detector", *Il Nuovo Cimento*, Vol. 112 A, no. 11,1239-1243, 1999.

[30] W. Ashmanskas, A. Bardi, *et all.*, "Silicon Vertex TRacker: A fast precise tracking trigger for CDF", *Nucl. Instr. Meth.*, Vol A **447**,218-222, 2000.

[31] J. A. Walls, " The SVX II Silicon Vertex Detector at CDF", *Nulc. Phys. B*, Vol 78,311-314, 1999.

[32] S. Belforte, M. Dell'Orso, *et all.*, "The SVT Hit Buffer", *IEEE Trans. Nucl. Sci.*, Vol. 43,1810-1813, 1996.

[33] S.R. Amendolia, S. Galeotti, *et all.*, "The AMchip: a full-custom CMOS VLSI Associative Memory for Pattern Recognition", *IEEE Trans. Nucl. Sci.*, Vol. 39,795-797, 1992.

[34] H.C. Andrew, Introduction to mathematical techniques in experimental data evaluation, *Wiley-Interscience*, 1972.

[35] H. Wind, Principal component analysis and its application to track finding, in " Formulae and methods in experimentl data evaluation", vol. III, R. Bock, *Europen Physical Society*, 1984.

[36] S. Donati et. all., $B^0 \to \pi^+\pi^-$ Trigger Studies with Run Ia Data, **CDF** Note 3167, (1995)

[37] K. Anikeev *et. all.*, Event Builder and Level-3 for aces,**CDF** Note 5793,(2001).

[38] S.Klimeno *et. all.*, The CDF Run II luminosity monitor,**CDF** Note 4330, (1998).

[39] S. Klimeno *et. all.*, CLC production and mechanical assembly, **CDF** Note 5119, (1999).

[40] D. Acosta *et. all.*, A first look at the CLC luminosity measurements, **CDF** Note 6052, (2002).

[41] Review of Particle Physics , *The European Physical journal C*, Società Italiana di Fisica & Springer-Verlag, 2004.

[42] A.Belloni, R.Carosi, S.Donati, I.Fiori, G.Punzi, First look at Two-Track trigger data, **CDF** Note 5758 Version 1.1, Dec. 2001.

[43] A.Cerri, R. Miqquel, Studying the SVT Efficiency and Resolution with J/ψ Data, **CDF** Note 5838 Version 1.0, (2002).

[44] C.Albajar *et al.*, **UA1** Collab., *Phys. Lett.* **B186**, 247 (1987).

[45] H.Albrecht *et al.*, **ARGUS** Collab., *Phys. Lett.* **B192**, 245 (1987).

[46] B.Andersson, G.Gustafson and C.Peterson, A Semiclassical Model for Quark Jet Fragmentation, *Zeitschrift f. Physik*, **C1**, 105-116 (1979).

[47] S.Aoki, talk at 19th Int. Symp. on Lepton and Photon Interactions, Stanford, 1999, *hep-ph/9912288*; P.Ball *et al.*, "*B decay* at the LHC", *hep-ph/0003238*.

[48] Manfred Paulini and Barry Wicklund for the **CDF** *B Physics Group*, Summary of Proposals for B Physics Triggers in Run II, **CDF** Note 5438 Version 1.0, Dec. 2000.

[49] Elena Gerchtein, Mario Campanelli, Calibration of the momentum scale for Kalman refitter using j/ψ events. **CDF** Note 6905 (2004)

[50] M Feindt, S.Menzemer,K.Reinnert,P.Schemitz,A.Skiba, KalKalmanFitter - A Fast and Versatile Kalman TRack-Fitter for CDF II, **CDF** Note 5388,(2000)

[51] LEP Working Group for B oscillations
`http://lepbosc.web.cern.ch/LEPBOSC/`

[52] Expectations and Aspirations in Run II (Joe Kroll).
`http://www-cdf.fnal.gov/physics/alltran.html`

[53] *see WEB-page*
`http://www-sk.icrr.u-tokyo.ac.jp/doc/sk/`.

[54] S. Herb et*al.*, *Phys. Rev. Lett.* **39** (1977) 252.

[55] Sheldon Stone, B DECAYS, *World Scientific*, 1991.

[56] K. Anikeev, C. Paus, P. Murat, Description of Bgenerator II, **CDF** Note 5092, Aug. 1999.

[57] P.Nason,S.Dawson, and R.K. Allis. The total cross-section fro the production of heavy quarks in hadronic collisions. *Nucl. Phys.,* B303:607,1988.

[58] See review of Particle Data Group, *CKM quark-mixing matrix*, F.J. Gilman, K. Kleinknecht and B. Renk.

[59] S. Aoki Lattice calculations and hadron physics. *Int. J. Mod. Phys.*, **A** 15S1:657-683 (2000).

[60] M. Battaglia et al., The CKM matrix and the Unitarity Triangle, *hep-ph/0304132* (2003)

[61] C. Kim and A. Martin, On the determination of V_{ub} and V_{cb} from semileptonic B decays, *Phys. Lett.* **B225** 186-190 (1989).

[62] Jonas Rademaker, Reduction of Statistical Power Per Evet Due to Uper Lifetime Cuts in Lifetime Measurements, **CDF** Note 7359 (2004)

[63] B_s Mixing group, Updated Study of Bs Oscillations in $B_s^0 \to D_s(3)\pi$, **CDF** Note 7861 (2005)

[64] S. Donati, G. Punzi, Two Track trigger with full SVT simulation, **CDF** Note 3780 Version 4.1, Jan. 1998.

[65] M.Beneke, G. Buchalla and I. Dunietz, Width difference in the $B_s - \bar{B}_s$ system, *Physical Review* **D54** 4419 (1996).

[66] Farrukh Azfar *et. al.* A Monte Carlo-Independent Mehtod for Lifetime Fits in Data Biased by Hadronic Trigger, **CDF** Note 6756.(2003)

[67] D. Acosta et al., The CDF Collaboration, *FERMILAB-PUB-04/148-E.*

[68] The CDF Collaboration, Measurement of J/ψ Meson and b-Hadron Production Cross Sections in $p\bar{p}$ collisions at $\sqrt{s} = 1950\ GeV$, *hep-ex/0412071*

[69] The CDF II Collaboration, Measurement of the Ratios of Branching Fractions $B(B_s \rightarrow D_s^- \pi^+)/B(B^0 \rightarrow D^- \pi^+) and B(B^+ \rightarrow \bar{D}^0 \pi^+)/B(B^0 - > D^- \pi^+)$, *hep-ex/0508014*

[70] W. Ashmanskas *et al.*, Performance of the CDF Online Silicon Vertex Tracker, **CDF** Note 5854 publeshed also on *Transactions on Nuclear Science.* (2002)

[71] S. Giagu, S. Da Ronco *et. al.*, The CharmMods/DFinder Reconstruction Package, Reference Manual,**CDF** Note 6158. (2004)

[72] K. Anikeev, Measurement of the Lifetimes of B Meson Mass Eigenstates, M.I.T. Ph.D. Thesis and **CDF** Note 7269,(2004)
K.Anikeev ,**CDF** Note 6551,(2004).

[73] K. Anikeev et al., B physics at Tevatron: Run II and beyond (2001)

[74] G. Gargiu, V. Tiwari, M.Paulini,J.Russ,B. Wicklund, Muon B Flavor Tagging - A likelihood Approach, **CDF** Note 7043, (2004)

[75] V. Tiwari,G.Gomez-Ceballos,I.Kravchenko, N.Leonardo,S.Menzemer,Ch.Paus, A.Rakitin, I.K.Furic,J.Piedra,A.Ruiz,I.Vila,G.J.Barker, M.Feindt, U.Kerzel,C.Lecci, Improved Jet Charge Tagger for summer conferences 2004, **CDF** Note 7131, (2004)

[76] P.Catastini, Same Side Kaon Tagging Studies, **CDF** Note 7496, (2004)

[77] W. Bell, J.Pablo Fernandez, User Guide for EvtGen at CDF, **CDF** Note 5618,(2003)

[78] R.Brun, R. Hgelberg,MHansroul, and J.C. Lasalle. Geant: Simulation program for particle physics experiments: user guide and reference manual, *CERN DD-78-2-REV.*

[79] K. Anikeev, New Measurement of lifetimes of B mesons in the exclusively reconstructed decays $B^+ \rightarrow J/\psi K^+$ $B^0 \rightarrow J/\psi K^{\star 0}$ $B_s \rightarrow J/\psi\phi$, **CDF** Note 6551,(2004)

[80] M. Campanelli, E. Gerchtein, Calibration of the momentum scale for Kalman refitter using J/ψ events, **CDF** Note 6905, (2004)

[81] G. Cowan, Statistical Data Analysis, *Oxford Science Publications*, (1998)

[82] F. James and Computing and Networks Division, The **MINUIT** Reference Manual v94.1
`http://wwwasdoc.web.cern.ch/wwwasdoc/WWW/minuit/minmain/minmain.html`

[83] René Brun, **ROOT** an Object-Oriented Data Analysis Framework. v3.05/07 and v4.00/08
`http://root.cern.ch/`